VACUUM ULTRAVIOLET SPECTROSCOPIC STUDY OF PLASMA IMPURITIES IN THE TOKAPOLE II POLOIDAL DIVERTOR EXPERIMENT

by

RICHARD JOSEPH GROEBNER

A thesis submitted in partial fulfillment of the requirements for the degree of

DOCTOR OF PHILOSOPHY
(Physics)

at the

UNIVERSITY OF WISCONSIN - MADISON

1979

TITLE: VACUUM ULTRAVIOLET SPECTROSCOPIC STUDY OF PLASMA IMPURITIES IN THE TOKAPOLE II POLOIDAL DIVERTOR EXPERIMENT

AUTHOR: Richard Joseph Groebner

NO. COO-2387-111

PLASMA PHYSICS
UNIVERSITY OF WISCONSIN
1150 University Avenue
Madison, Wisconsin 53706

VACUUM ULTRAVIOLET SPECTROSCOPIC STUDY OF PLASMA

IMPURITIES IN THE TOKAPOLE II POLOIDAL DIVERTOR EXPERIMENT

Richard Joseph Groebner

Under the supervision of Professor J. C. Sprott

Impurities in tokamak plasmas increase the plasma resistivity, radiate energy out of the plasma, and are implicated in the disruptive instability. Results of a study of plasma impurities in Tokapole II, a tokamak with a four-node poloidal divertor, are reported.

The main diagnostics were two vacuum ultraviolet spectrometers, which were used to identify impurities, observe impurity behavior, and measure the line radiated power. Impurity concentrations and the effects of impurities on gross plasma characteristics were determined with an impurity doping technique. The electron temperature was estimated by a time dependent coronal model describing the time history of the oxygen ions, and the ion temperature was obtained from Doppler broadening measurements. Energy loss processes were studied with a power balance analysis.

For typical discharges (B_T = 3.5 kG, $\bar{n}_e \approx 8 \times 10^{12}$ cm^{-3}, $T_e \approx 100$ eV, $T_i \approx 17$ eV), the impurities and their concentrations were oxygen (3-5%), carbon (~ 0.5%), nitrogen (associated with air leaks), and copper (undetermined concentration). The maximum radiated power of 35 to 70 kW was not more than 15 to 30% of the ohmic input power.

During the steady state phase of the discharge, the electron and ion confinement times were about 200 to 250 μsec and 300 to 500 μsec, respectively. The discharge current was not affected by impurity dopant densities of up to 5×10^{11} cm^{-3}; at higher dopant densities, the current decreased roughly linearly with the dopant level.

The plasma can be conveniently treated as two parts: a central current channel separated from a scrape-off layer by a separatrix. Impurity radiation does not dominate the energy loss processes. The energy confinement time of the central channel is comparable to that predicted by two tokamak scaling laws; this observation suggests that the primary energy loss process is anomalous electron heat conduction. Impurity radiation does not limit the electron temperature. Instabilities, probably internal disruptions, evidently limit the central current density and T_e.

The internal rings are major impurity sources. Generation of metallic impurities can only be explained by invoking the presence of sheath potentials, which are necessary for unipolar arcs and which enhance the sputtering yield of multiply-charged impurity ions.

The role of impurities in Tokapole discharges is similar to that in recent tokamaks. Very likely, further reduction of the impurity levels will permit operation in new regimes of energy confinement time, electron density, and β (ratio of plasma pressure to magnetic field pressure).

J. C. Sprott

Professor J. C. Sprott

ACKNOWLEDGEMENTS

Many people have been helpful in my research and in the preparation of this thesis.

I express my deep appreciation to Sandy White for her wonderful patience, understanding, and encouragement of me in my work.

For his interest in my research and for his constructive criticism and suggestions, I thank Professor J. C. Sprott.

I am gratefully indebted to Professor R. N. Dexter for making available much of the diagnostic equipment used in my research and for working closely with me in the taking and analyzing of the data presented in this thesis.

The work of T. Lovell, R. Vallem, and their technical crew in the construction, maintenance, and repair of experimental equipment was invaluable. I thank B. Lipschultz for assembling the microwave discharge lamp.

D. Shephard, M. Phillips, and D. Witherspoon have provided data which I have used in my thesis, and I express my appreciation to them. I have had very helpful discussions and interactions with Professor S. C. Prager, B. Lipschultz, D. Shephard, K. Miller, D. Witherspoon, T. Osborne, A. Biddle, and D. Holly.

I thank B. Bullock for doing a fine job in typing this manuscript.

This research was supported by the United States Department of Energy.

TABLE OF CONTENTS

		Page
ABSTRACT		ii
ACKNOWLEDGEMENTS		iv
TABLE OF CONTENTS		v
1.	INTRODUCTION	1
	A. Background and History	1
	B. Statement of the Problem	3
	C. Motivation	4
	D. Preview of the Thesis	5
2.	TOKAPOLE II - THE MACHINE	10
	A. Design Characteristics	10
	B. The Vacuum Vessel	14
	C. Poloidal Field	19
	D. Toroidal Field	21
	E. Vacuum System	22
3.	DIAGNOSTICS	27
	A. Near Ultraviolet-Visible Monochromator	27
	B. Vacuum Ultraviolet Survey Instrument	28
	C. 1-m Seya-Namioka Monochromator	34
	D. Filter-detector Combinations	35
	E. Residual Gas Analyzer	36
	F. Fast Ionization Gauge	37
	G. Plasma Current Monitor	37
	H. Rogowski Coils	38
	I. Microwave Interferometer	38
	J. Langmuir Probes	38
	K. Electric Field Probe	39
	L. Magnetic Probes	39
	M. External Field Measurements	40
	N. Computer	40
4.	SPECTROSCOPY PRIMER	42
	A. Introduction to the VUV Region	42
	B. Line Radiation	43
	C. Coronal Equilibrium	48
	D. Time Dependent Coronal Model	50
	E. Spectroscopic Electron Temperature Measurements	54
	F. Radiated Power Measurements	55
	G. Radiometry-Theory	55
	H. Radiometry-Practical Application	62

5. CHARACTERISTICS OF TOKAPOLE II DISCHARGES 72
A. Fields and Timing 72
B. Gross Plasma Characteristics 75
C. Spatial and Temporal Electrical Measurements 82
D. Equilibrium and Stability 95
E. Discharge Evolution 104

6. IMPURITY OBSERVATIONS 110
A. Dirty Discharge 110
B. Standard Discharge-General Observations 113
B.1. Impurity Identification 113
B.2. Temporal Impurity Behavior 117
B.3. Radiated Power 125
C. Phenomenological Impurity Study 128
C.1. Impurity Concentrations 129
C.2. Impurity Contributions to Radiated Power 132
C.3. Z_{eff} Estimate 143
C.4. Amp-Second Behavior 143
C.5. Model of AS Behavior 149
D. Impurity Production 155
D.1. Location of Impurity Generation 155
D.2. Metallic Impurities 160

7. TEMPERATURE MEASUREMENTS 167
A. Rate Coefficients 167
B. Electron Temperature in the Dirty Discharge 168
C. Computer Modeling of Oxygen Radiation 169
D. Impurity Influx 176
E. Ion Temperature Measurements 178

8. POWER BALANCE CONSIDERATIONS 193
A. Basic Data 193
B. Energy Loss Mechanisms 206
C. Energy Confinement Time Scaling Laws 208

9. DISCUSSION 215
A. Summary 215
B. Conclusions 217
C. Discussion 220

CHAPTER 1

INTRODUCTION

A. Background and History

Impurities alter the resistivity and contribute to the power loss mechanisms of tokamak plasmas. Impurities could have devastating results in a fusion reactor; indeed, they produce many undesirable effects in present-day tokamaks.

Post, in making perhaps the earliest mention of the impurity problem, noted that Bremsstrahlung from high-Z (high atomic number) impurities would increase the difficulty of igniting a fusion reactor.[1] A calculation by Meade indicated that a 0.2% tungsten impurity in a D-T reactor would prevent ignition at any temperature.[2] More recent calculations by Jensen, Post, and Jassby show that the restrictions on heavy metal content in driven toroidal fusion reactors are severe.[3]

The importance of impurities in tokamaks has long been recognized. Vacuum vessel wall conditioning, consisting of baking and discharge cleaning, was employed on the early Soviet tokamaks to produce stable discharges and to reduce the power radiated by the plasma.[4] More recently, spectroscopic studies performed on a number of tokamaks have shown that impurity radiated power is typically 10-80% of the ohmic input power.[5-10] Carbon and oxygen, in particular, are the most troublesome low-Z impurities, and limiter and wall materials can also play major roles in the plasma dynamics.

The enhancement of the plasma resistivity over that expected from a pure hydrogen plasma (by factors of typically 3-10) is due to the

resistivity contribution of the impurities.[11] Low-Z impurities, which recycle at the periphery of the plasma, cool the plasma edge by radiation and ionization losses, increase the edge resistivity, and produce peaked electron temperature and current density profiles.[12] High-Z, partially ionized impurities radiate from the center of the current channel. In extreme cases this radiation has resulted in a radical reduction of the central electron temperature and the production of a hollow electron temperature profile.[13] Impurities can contribute to plasma disruptions by cooling the plasma periphery, shrinking the current profile which decreases the safety factor at the edge of the plasma, and thereby allowing the growth of the dangerous m=2, n=1 tearing mode which can lead to a disruption.[14]

Several studies have obtained detailed spatial information on the temporal behavior of impurities.[15-17] The results indicate that the impurities diffuse inward, but the diffusion mechanisms are not fully understood.[17] Impurities also diffuse to the chamber walls in all of the ionization states present in the plasma.

Light (low-Z) impurity release into the plasma is attributed to desorption by ions, electrons, photons, and neutrals.[18,19] Heavy metal production is strongly linked to the existence of sheath potentials at the limiter and wall interfaces with the plasma. Metal production in DITE is explained as resulting from unipolar arcs.[20] Work on DIVA has shown that sputtering and evaporation as well as unipolar arcs are responsible for metal production.[21]

Control of impurities in tokamaks is based on the judicious selection of materials which can be exposed to the plasma and discharge

cleaned to remove low-Z impurities. The Taylor discharge cleaning method[22] is the best technique known for removing oxygen impurities and has resulted in the production of $Z_{eff} \simeq 1\text{-}3$ in several machines.[23,24,25] Titanium gettering of vacuum surfaces produces plasmas with low Z_{eff} and raises the electron density limit before disruption.[26,27]

Other impurity control techniques have been attempted. Bundle[28] and poloidal divertors[29] have successfully reduced the impurity flow into the main plasma body. (PDX and ASDEX are two new poloidal divertor experiments going into operation now.[30,31]) Electron injection into the plasma has reduced heavy metal production by reducing the sheath potential at the wall.[32] An impurity flow reversal experiment, in which an influx of hydrogen gas was used to reverse the inward diffusion of impurities, produced mixed results. The diffusion of neon impurities responded to the gas flow but the normal light impurities were rather unaffected.[33] A variety of limiter materials has been used in tokamaks.[26,34,35] The results show that low-Z materials reduce the central radiation which is present with high-Z (molybdenum and tungsten, in particular) limiters. A carbon limiter has produced very encouraging results on PLT.[26]

B. Statement of the Problem

This thesis addresses the question: What is the role of impurities in Tokapole II ohmic discharges and how seriously do they affect plasma performance? The research to be described is not a detailed study of any one aspect of the impurity problem; rather, it is an integrated study of several facets of the problem. To characterize the impurity problem, the following studies have been performed:

(1) the impurities have been identified or tentatively identified and their concentrations determined where possible;

(2) the impurity radiated power has been measured;

(3) impurity release mechanisms have been studied;

(4) the power balance has been quantified;

(5) a phenomenological study has been performed to determine the effects of impurities on the plasma behavior.

A subsidiary goal of this work is to characterize the behavior of the gross plasma parameters. This effort is composed of the following parts:

(1) ion and electron temperatures have been measured by spectroscopic means;

(2) available data have been compiled and analyzed to provide an overall picture of the plasma behavior and development.

C. Motivation

There are several reasons for the pursuit of the impurity study. Tokapole II is a tokamak device; all such devices are characterized by impurity problems which are machine dependent. This research has determined the way in which impurities affect plasmas in the Tokapole II device. Furthermore, Tokapole II is a tokamak with a poloidal magnetic divertor; as such, the machine might be characterized by impurity effects different from those of conventional tokamaks. This work is a study of impurity behavior in a divertor machine. One of the research goals of this device is the study of the plasma-wall interaction. This thesis describes the initial work of that nature and is a prelude to

further detailed studies of the impurity problem. Finally, the results of this research may suggest techniques of impurity control for Tokapole II.

The more general discussion of the basic plasma characteristics is included primarily because it has not appeared anywhere else yet, since Tokapole II is a new research device. The background presented is needed to put the results of the impurity investigation into perspective. Also, spectroscopic studies of impurities were used to measure the ion and electron temperatures, quantities which have not yet been determined by other techniques, and these studies are presented here.

D. Preview of the Thesis

Chapter 2 is a detailed description of the Tokapole II device, and Chapter 3 is a discussion of the diagnostics used to acquire the data for this study. The impurities were studied primarily with the techniques of vacuum ultraviolet spectroscopy, and in-depth descriptions of the spectroscopic instrumentation will be presented. Chapter 4 is essentially an introduction to the field of vacuum ultraviolet spectroscopy; it contains discussions of instrumentation problems and of the use of spectroscopic information to measure basic plasma parameters. A discussion of the time development of several plasma quantities in Tokapole II discharges is presented in Chapter 5, and the results are analyzed to provide a coherent picture of the discharge behavior. Chapter 6 presents the basic impurity measurements: impurity identifications and concentrations, Z_{eff}, impurity radiated power, impurity doping experiments, and impurity sources. Chapter 7 introduces a computer code

to model oxygen radiation. This code was used to determine the electron temperature and to study the influx of impurities in the discharge. Doppler broadening measurements of the ion temperature are also presented. An analysis of the power balance, calculations of the energy confinement time, and comparisons of the confinement time with empirical scaling laws are presented in Chapter 8. The final chapter contains a summary of the results, an analysis of the role of impurities in Tokapole II discharges, suggestions for further impurity studies, and suggestions for impurity control techniques.

REFERENCES

1. R. F. Post, Rev. Mod. Phys. 28, 338 (1956).
2. D. M. Meade, Nucl. Fusion 14, 289 (1974).
3. R. V. Jensen, D.E. Post, D. L. Jassby, Princeton Plasma Physics Lab. Rep. PPPL-1350, 1977.
4. L. L. Gorelik, S. V. Mirnov, V. G. Nikolaevsky, V. V. Sinitsyn, Nucl. Fusion 12, 185 (1972).
5. J. L. Terry, K. I. Chen, H. W. Moos, E. S. Marmar, Nucl. Fusion 18, 485 (1978).
6. Equipe TFR, Nucl. Fusion 15, 1053 (1975).
7. N. Bretz, D. L. Dimock, E. Hinnov, E. B. Meservey, Nucl. Fusion 15, 313 (1975).
8. K. Odajima et al., Nucl. Fusion 18, 1337 (1978).
9. L. A. Berry et al., in Plasma Physics and Controlled Nuclear Fusion Research (Proc. 6th Int. Conf. Berchtesgaden, 1976) Vol 1, IAEA, Vienna, 49 (1977).
10. M. Shiho et al., Nucl. Fusion 18, 1705 (1978).
11. E. Hinnov, L. C. Johnson, E. B. Meservey, D. L. Dimock, Plasma Phys. 14, 755 (1972).
12. H. P. Furth, Nucl. Fusion 15, 487 (1975).
13. E. Hinnov et al., Nucl. Fusion 18, 1305 (1978).
14. R. J. Bickerton, Culham Laboratory, Report CLM-R 176, 1977.
15. S. A. Cohen, J. L. Cecchi, E. S. Marmar, Phys. Rev. Lett. 35, 1507 (1975).
16. E. Hinnov et al., Plasma Phys. 20, 723 (1978).

17. T.F.R. Group, Plasma Phys. 20, 735 (1978).

18. T.F.R. Group, in Proceedings of The International Symposium on Plasma Wall Interaction, Jülich, 1976 (Pergamon Press, New York, 1977), p. 3.

19. P. Staib, G. Staudenmaier, J. Nucl. Materials 76 & 77, 78 (1978).

20. G. M. McCracken, D.H.J. Goodall, Nucl. Fusion 18, 537 (1978).

21. K. Ohasa et al., Nucl. Fusion 18, 872 (1978).

22. L. Oren, R. J. Taylor, Nucl. Fusion 17, 1143 (1977), and Univ. of Calif. at Los Angeles, Report PPG-294, 1977.

23. M. Murakami et al., Phys. Rev. Lett. 42, 655 (1979).

24. R. J. Taylor, J. DeVilliers, F. Martin, Bull. Am. Phys. Soc. 20, 1373 (1975).

25. E. Meservey et al., Bull. Am. Phys. Soc. 22, 1075 (1977).

26. K. Bol et al., Princeton Plasma Physics Lab. Rep. PPPL-1492, 1978.

27. S. J. Fielding et al., Nucl. Fusion 17, 1382 (1977).

28. J. W. M. Paul et al., Culham Laboratory, Rep. CLM-P 502, 1977.

29. DIVA Group, Nucl. Fusion 18, 1619 (1978).

30. D. M. Meade, J. C. Sinnis, in Plasma Wall Interaction, Proc. Int. Symp. Jülich, 1976 (Pergamon Press, New York, 1977), p. 683.

31. G. Haas, M. Keilhacker, in Plasma Wall Interaction, Proc. Int. Symp. Jülich, 1976 (Pergamon Press, New York, 1977), p. 691.

32. R. J. Taylor, L. Oren, Phys. Rev. Lett. 42, 446 (1979).

33. K. H. Burrell et al., Phys. Rev. Lett. 41, 1382 (1978).

34. E. B. Meservey, N. Bretz, D. L. Dimock, E. Hinnov, Nucl. Fusion 16, 593 (1976).

35. R. Bardet et al., in Plasma Physics and Controlled Nuclear Fusion Research (Proc. 6th Int. Conf. Berchtesgaden, 1976), Vol II, IAEA, Vienna, 259 (1977).

CHAPTER 2

TOKAPOLE II -- THE MACHINE

Tokapole II, the University of Wisconsin's newest internal ring machine, is the successor to the venerable Wisconsin Supported Toroidal Octupole.[1] The vacuum chamber and internal rings were constructed by the University of Wisconsin Physical Sciences Laboratory machine shop, much additional hardware was fabricated by the University of Wisconsin Physics Department machine shop, and the machine was assembled by the plasma physics group of the University of Wisconsin Physics Department. The first plasma in this machine was produced on March 29, 1978. This chapter discusses the design characteristics, specifications, and noteworthy features of Tokapole II. Much more detail about the hardware aspects of the machine can be found elsewhere.[2,3]

A. Design Characteristics

Tokapole II is a toroidal magnetic containment device with a square minor cross section and four internal rings, each supported by three rods. Figure 2-1, a view of the cross section of the toroid, shows the vacuum poloidal magnetic field flux plot produced by current in the rings. The poloidal field strength is zero at the center of the flux plot and increases as the cube of the minor radius.

This device was designed to operate well as a pure octupole or as a tokamak. Good octupole confinement legislated that the amount of poloidal flux inside the last MHD stable flux surface be as large as possible and that the area of the supports for the internal rings be as small as possible. Good tokamak performance was suggested by the

Fig. 2-1: Vacuum poloidal magnetic field flux plot. Major axis is to left.

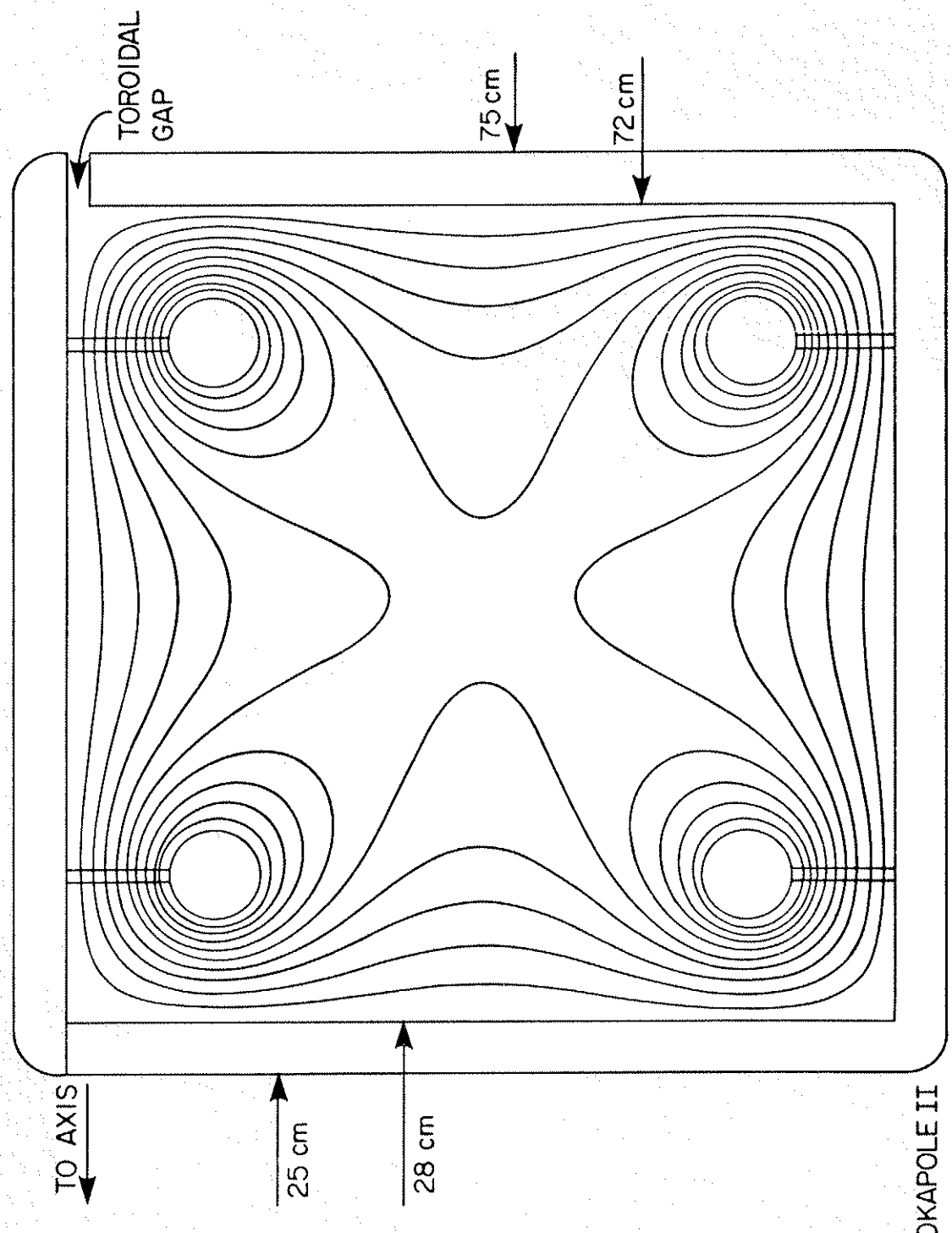
TOROIDAL GAP
75 cm
72 cm
TO AXIS
25 cm
28 cm
TOKAPOLE II

empirical tokamak scaling laws: $n_e \propto B_T/R$ and $\tau_E \propto n_e a^2$ where n_e is electron density, B_T is toroidal field strength, R is the machine major radius, a is the plasma minor radius and τ_E is the energy confinement time. The product $n_e \tau_E$ is therefore proportional to $(B_T a/R)^2$, and to maximize this product a large toroidal field and a small aspect ratio (R/a) are desirable. Thus, Tokapole II was designed with a major radius of 50 cm and a 44 cm square minor cross section. This provided a machine with the largest minor diameter and smallest aspect ratio which could reasonably fit inside the window of the existing transformer core.

The toroidal field was designed to operate up to 10 kG. With existing capacitors a field of 5 kG can be achieved; capacitors currently being acquired will allow operation to 8.5 kG. A 20 msec L/R time was chosen for the toroidal field to provide a discharge length much longer than the energy confinement time.

Great attention was paid to magnetic symmetry and to the reduction of field errors. A degenerate octupole magnetic field null was deemed very important to allow easy start-up of the toroidal plasma current and formation of the desired Tokapole equilibrium. The machine was designed to be as clean as possible and to operate at a high base vacuum (low pressure). A clean machine is essential to reduce the severity of the impurity problem in tokamak operation.

Another requirement was that the number of diagnostic ports be large and that diagnostic access be adequate. A closely related requirement was that access for maintenance be good and that disassembly of the machine be as simple as possible. Over-riding concerns in all phases of the design were that components be as reliable and maintenance-

free as possible.

B. The Vacuum Vessel

Figure 2-2 shows a view from the top of the Tokapole II vacuum vessel, while Fig. 2-3 shows a view of the tank cross section. As already indicated, the major radius is 50 cm while the minor cross section is square with sides of 44 cm. The minor diameter of the rings is 5 cm, and their positions are indicated in Fig. 2-3. The vacuum vessel itself consists of two pieces -- a tank consisting of two concentric cylinders welded to the bottom plate and a lid. This vessel is constructed from three cm thick type 6061-T6 aluminum, which has a good compromise of yield strength (40,000 lb/in^2) and conductivity (45% IACS). The resulting L/R time is about 15 msec.

Conducting walls have several advantages. For instance, machines with conducting walls have a higher degree of magnetic symmetry than machines with non-conducting walls. However, conducting walls require the existence of insulated gaps to allow penetration of the magnetic fields into the vacuum chamber. The toroidal and poloidal gaps are made with ¼" viton sheet which has been compressed to 0.180". Shields of Macor (Corning machineable ceramic) and stainless steel have been used to protect the gaps from plasma.

A total of 42 ports are located along radial lines at 30° intervals around the machine. This layout permits good diagnostic access, allows the toroidal field windings to be straight and short, and thus has permitted a high degree of symmetry in the winding of the toroidal field coil. See Fig. 2-2.

Fig. 2-2: Top view of vacuum vessel, toroidal field coil channels, and transformer core. Top leg of core is not shown.

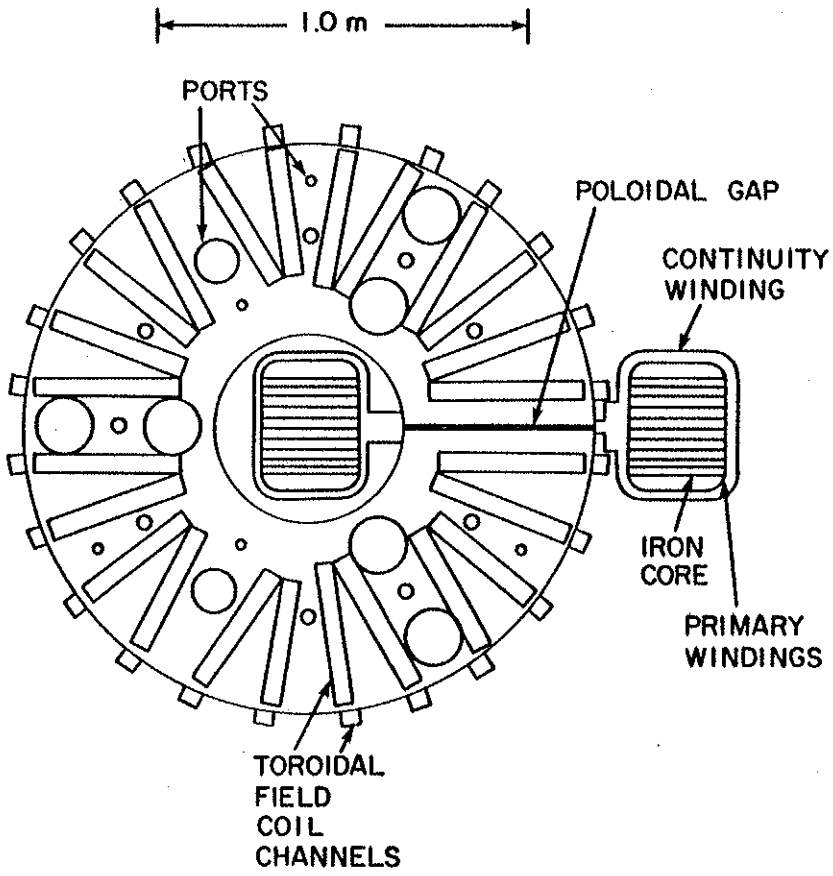
1.0 m
PORTS
POLOIDAL GAP
CONTINUITY WINDING
IRON CORE
PRIMARY WINDINGS
TOROIDAL FIELD COIL CHANNELS

TOKAPOLE II

Fig. 2-3: Vacuum tank cross section with dimensions and positions of internal rings. Midplane and midcylinder are indicated by dotted lines.

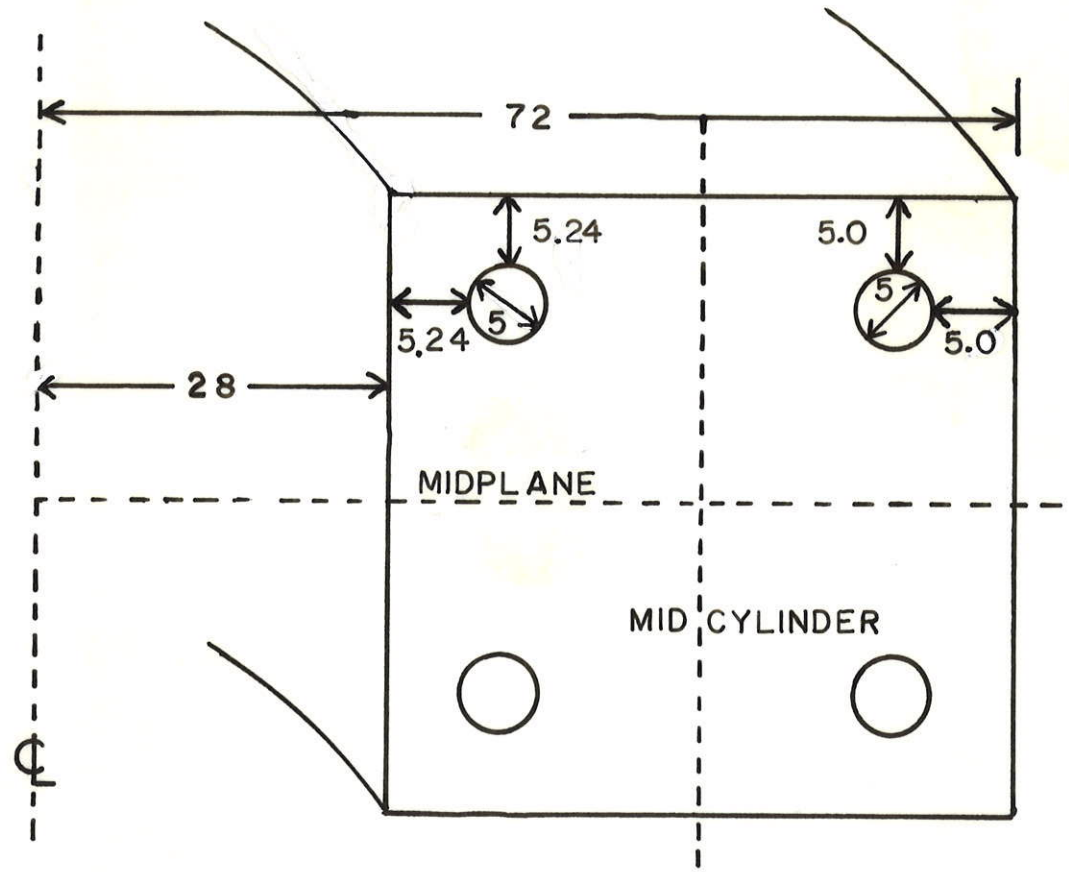

DIMENSIONS IN cm

C. Poloidal Field

Figure 2-1 shows the computer-drawn poloidal flux plot chosen for Tokapole II. In this magnetic configuration, half of the poloidal flux is common (is linked by all four rings) and half is private (is linked by only one ring), so that a filament of current on the magnetic axis links half of the total flux. Since the iron core saturates at 0.15 volt-seconds (with cocking), the available poloidal flux is 0.15 webers.

Computer calculations showed that the degenerate field null is very sensitive to ring positioning and that a movement of one ring by 1 mm was sufficient to break the null into three non-degenerate field nulls separated by a few cm. Thus, considerable attention was directed to ensuring that the tank, supports, and rings were manufactured to high precision and that the rings would be positioned properly with respect to the tank walls. Furthermore, the rings can be adjusted vertically ± 5.0 mm from their normal positions to permit fine-tuning of the null.

Careful design was used to minimize poloidal field errors which are inevitably associated with the poloidal gap in the conducting wall. Toroidal currents, images of the ring currents, flow in the walls and these are returned around the transformer core with copper shells, called continuity windings. The conductivity of these windings was tailored to the current density in the walls to reduce the poloidal component of the current flowing through the walls and continuity windings. The primary windings were placed very close to the continuity windings to reduce leakage flux. Furthermore, the turns of the primary winding were spaced non-uniformly so that the current density in the primary would be proportional to the surface current density in the

walls, in order to further reduce poloidal currents at the poloidal gap.[2]

Holes in the conducting wall introduce a dipole field error in the poloidal field, but the effect of these can be minimized if the holes are placed symmetrically about the midplane. Thus, magnetic symmetry was preserved by arranging ports, where possible, in pairs about the midplane. The major exceptions to this are two 7.5" diameter pumping ports on the bottom of the tank. Field errors at these ports have been reduced by inserting partially transparent copper plugs in the holes to carry the image currents.

At peak designed magnetic field, each inner ring experiences a vertical magnetic force of about 12,500 lb while each outer ring experiences a force of about 8000 lb. The three supports for each ring also experience the same magnetic forces as the ring. During a current pulse, each ring-support system rebounds after the initial impulse, and the applied forces during the rebound exceed the original forces by a factor of about 1.7. During the rebound, each inner support experiences a force of about 7000 lb while each outer support experiences a force of about 4500 lb. The rings also support horizontal forces. The requirements for the ring material of good conductivity and high strength were satisfied best by a chromium-copper alloy, Ampcoloy 97, which has a yield strength of 43,000 lb/in^2 and a conductivity of 78% IACS. A heat-treated beryllium-copper alloy, Berylco 25 HT, which has a yield strength of 165,000 lb/in^2, was chosen as the hanger material. The hangers collectively expose a total area of 133 cm^2 to the plasma.

For the results presented in this thesis, the poloidal field

energy source was a bank of 30-240 μF, 5 kV capacitors. Thus, the total capacitance was 0.0072 F and the maximum energy available was 90 kJ. The inductance L_R and resistance R_R of the rings are given as functions of time by[4]

$$L_R = 0.219 + 0.06834\ (1 - e^{-396\ t})\ \mu H \qquad (2\text{-}1)$$

$$R_R = 7.8 + 16.9\ e^{-396\ t}\ \mu\Omega, \qquad (2\text{-}2)$$

where t is time in seconds after the beginning of the poloidal field pulse. The time dependences take into account the penetration of the magnetic field into the rings. With a 40:1 turns ratio on the transformer, the poloidal field shape in time is sinusoidal with a half period of 5.6 msec. From Eqns. 2-1 and 2-2, the L/R time of the rings is 9 msec at t = 0 and 37 msec at t = ∞.

A power crowbar, consisting of a 900 V, 0.025 F, 10 kJ capacitor bank can be used to extend the length of the poloidal field pulse. This bank will be replaced by a new 450 V, 0.5 F, 50 kJ bank.

D. Toroidal Field

The location of the toroidal field windings is illustrated in Fig. 2-2. With the 30° port spacing, a toroidal field coil of 24 sections was allowed. Since the vacuum vessel is conducting, toroidal field symmetry is assured if the toroidal winding crosses the toroidal gap at evenly spaced intervals. The winding was carefully installed to maximize the symmetry. Three channels made of 2" x 1 3/4" x 1/8", 6063-T52 aluminum fasten each section to the tank. The winding actually consists of 96 turns so that each section includes four turns. For the work to be described, the winding was made from two 400 ft sections

of AWG 4/0 high-temperature welding cable. The insulation of this wire suffered excessive abrasion during its use, and it has been replaced with a new winding of AWG 4/0 wire with a highly abrasion-resistant insulation, called hypalon. The mechanical strength of the channels and stainless steel hold-down studs is sufficient to permit toroidal fields of 10 kG.

Energy for the toroidal field is supplied by a bank of 42-240 μF, 5 kV capacitors with a maximum storage capacity of 126 kJ. With the 96 turn toroidal winding, this bank can produce a field of 5 kG on the magnetic axis, and as a function of time the field is sinusoidal with a half period of about 10 msec. An ignitron is used to passively crowbar the toroidal field when it reaches peak strength, and thus the toroidal field varies slowly (by ~20%) for the duration of a typical plasma discharge.

E. Vacuum System

Tokapole II has a volume of 600 liters and an internal surface area of about 6 square meters. These surfaces are primarily aluminum and copper. Vacuum pumps are a 1500 liter/sec turbomolecular pump (Sargent Welch model 3133) and a 1000 liter/sec 10° K Ultek cryopump. Experience on Tokapole I and on Tokapole II has been that in a leak-tight vacuum system, the main residual gas is water vapor. A 50 hour, 60-80 °C bake on Tokapole I reduced its base pressure by a factor of about 2 and helped to produce a record vacuum in that machine. An analysis of the vacuum system of Tokapole II suggests that a 100-150 °C bake of Tokapole II should reduce the pressure due to metal outgassing to the low 10^{-10} Torr range.[5] At that point, the Viton vacuum seals

used on the machine would be expected to limit the base pressure. After a 150 °C bake, Viton has a much higher outgassing rate than the metal; furthermore, permeation of atmospheric gasses through the Viton would then become comparable to or greater than the outgassing. After a bake, Viton is predicted to contribute a partial pressure of about 8×10^{-9} to 1.6×10^{-8} Torr to the base pressure.[5] Because of the difficulty in predicting vacuum performance of various materials and pumps, these calculations are a crude estimate, but they suggest that a base vacuum of at least 1×10^{-8} Torr should be achievable on this machine. To date, the record base vacuum has been 3×10^{-8} Torr after a 70-75 °C bake.

Because of the serious nature of the impurity problem in hot plasmas, great care has been taken to eliminate undesirable materials from the interior of Tokapole II. Vacuum grease is not allowed anywhere. Prior to assembly, the interior of the tank was cleaned with barcothene (similar to tricloroethylene), and this was followed with an acetone rinse and then an alcohol rinse. Vacuum pumps which would not introduce oil into the vacuum chamber were chosen, and great care has been taken to prevent roughing pump oil from backstreaming under any circumstances into the vacuum chamber. Only a limited number of materials is permitted in the vacuum. The following materials may be exposed to the plasma: aluminum, copper, stainless steel, Macor, alumina, 95/5 solder, beryllium, chrome, and gold. The following materials may be used but must be shielded from the plasma: viton, teflon, quartz, pyrex, tungsten, nickel, mica, kovar, and Sauereisen cement.

At the present time, baking is accomplished by circulating hot water through a set of aluminum bosses placed between the toroidal field coils on the side of the machine. Eventually, hot oil will be flowed through this system to raise the machine temperature to ~150 °C. Cold water is circulated through the same system to quickly cool the machine to room temperature.

Discharge cleaning is performed by pulsing the toroidal field to about 1 kG every 2 sec and ringing the poloidal gap with a decaying sine wave voltage which has an initial amplitude of about 60 volts and a frequency of 2.7 kHz. Reference 3 contains a circuit diagram of the discharge cleaning apparatus.

Table 2-1 is a summary of Tokapole II parameters.

TABLE 2-1: PARAMETERS OF TOKAPOLE II

MAJOR RADIUS: 50 cm

MINOR CROSS SECTION: 44 cm x 44 cm square

TOROID WALLS: Aluminum, 3.0 cm thick with poloidal and toroidal insulated gaps

VACUUM VOLUME: 600 liters

VACUUM SURFACE AREA: 6 square meters

NUMBER OF INTERNAL RINGS: 4 (copper, 5 cm dia., supported at 3 points)

PORTS: 2-7.5" dia., 5-4.5" dia., 22-1.5" dia., 13-0.25" dia.

B_T ON AXIS: 5 kG (extendable to 10 kG by the acquisition of additional capacitors)

L/R TIME OF B_T: 20 msec

AVAILABLE OH VOLTAGE: 125 volts

POLOIDAL FLUX: 0.15 webers

AVAILABLE ENERGY (POLOIDAL + TOROIDAL FIELDS): 216 kJ (72-240 μF, 5 kV capacitors)

BASE VACUUM: 5×10^{-8} Torr (1×10^{-8} Torr expected after 150 °C bake is available)

PUMPING SYSTEM: 1500 ℓ/sec turbomolecular pump, 1000 ℓ/sec 10° K cryopump, (titanium getter pump might be installed)

BAKEOUT TEMPERATURE: 75 °C (150 °C with hot oil system), quick cool to <50 °C in 15 minutes

PREIONIZATION: 5 kW, 2.45 GHz; 10 kW, 9 GHz; 10 kW, 16 GHz ECRH

REFERENCES

1. R. A. Dory, D. W. Kerst, D. M. Meade, W. E. Wilson, C. W. Erickson, Phys. Fluids 9, 997 (1966).

2. J. C. Sprott, T. W. Lovell, University of Wisconsin Plasma Studies PLP 744, 1978.

3. J. C. Sprott, Proceedings of the Small Toroidal Device Users' Meeting in Monterey, CA, May 18, 1978, and University of Wisconsin Plasma Studies PLP 750, 1978.

4. J. C. Sprott, University of Wisconsin Plasma Studies PLP 777, 1979.

5. R. J. Groebner, University of Wisconsin Plasma Studies PLP 124, 1977.

CHAPTER 3

DIAGNOSTICS

This chapter describes the diagnostics which were used to accummulate the data for this thesis. Most of the data were taken with the three spectrometers to be described and with the soft x-ray (SXR) detector. Some of the diagnostics were used by other individuals, and certain results obtained by them are quoted here. These diagnostics include all electrical probes which were used to obtain spatial profiles of plasma parameters: $\dot{B}$ coils, the electric field probe, the small Rogowski coil, and Langmuir probes. Reference 1 contains additional information about the spectroscopic diagnostics.

A. Near Ultraviolet-Visible Monochromator

A Model 82-010, 1/2-meter Jarrell-Ash monochromator, equipped with a 1180 line/mm grating blazed at 5000 Å, was used to perform spectroscopic measurements in the range 2000-6600 Å. The instrument has an Ebert-Fastie grating mounting,[2] and it can be scanned to 8500 Å. The reciprocal linear dispersion of the grating at the exit slit is 16 Å/mm. Normally, 50 micron entrance and exit slits were used for routine work, and 10 micron slits were used for high resolution. The maximum resolution was about 0.4 Å for the hydrogen λ4861 Å line (hereafter to be denoted as HI 4861.) Photons were detected by an RCA 1P28 photomultiplier tube or by an EMI 9635 QB photomultiplier tube (PMT), which had a better signal to noise ratio than the 1P28.

This monochromator views the plasma through a 4-1/2 inch diameter

quartz window, which transmits well down to about 2000 Å. The instrument can be mounted on a TV camera base and tilted at various angles to provide spatial information about the origin of the impurity radiation.

B. Vacuum Ultraviolet Survey Instrument

A 1/2-meter Seya-Namioka spectrometer, designed and built by Prof. R. N. Dexter's group, was used to provide a quick panoramic view of the vacuum ultraviolet (VUV) spectrum in the 500-1250 Å region. A 1200 line/mm magnesium fluoride-coated aluminum concave grating, blazed at 1300 Å, with a radius of curvature of 50 cm and a reciprocal linear dispersion of 14.5 Å/mm, has been used for the data presented in this thesis. At present, a gold grating, with 1200 line/mm and a blaze at 700 Å is being used in the instrument, and this grating extends the useful range to 300-400 Å.

This survey instrument is illustrated schematically in Fig.3-1. A typical Seya has fixed entrance and exit slits which subtend an angle of 70.5° at the grating. This mounting provides an instrument which can be scanned by rotating the grating about its axis while minimizing focusing errors at the exit slit.[2] The concave grating serves to disperse the incident light and to focus images of the entrance slit onto the exit plane.

The instrument used here has a 50 micron entrance slit while the exit slit has been replaced by a 75 mm diameter microchannel plate in the exit plane. This detector is essentially an electronic piece of film; it records all of the spectral lines incident upon it as a piece of photographic film would. The detector used is a Bendix BL 6075

Fig. 3-1: Schematic of vacuum ultraviolet survey apparatus.

SCHEMATIC OF VUV SURVEY APPARATUS

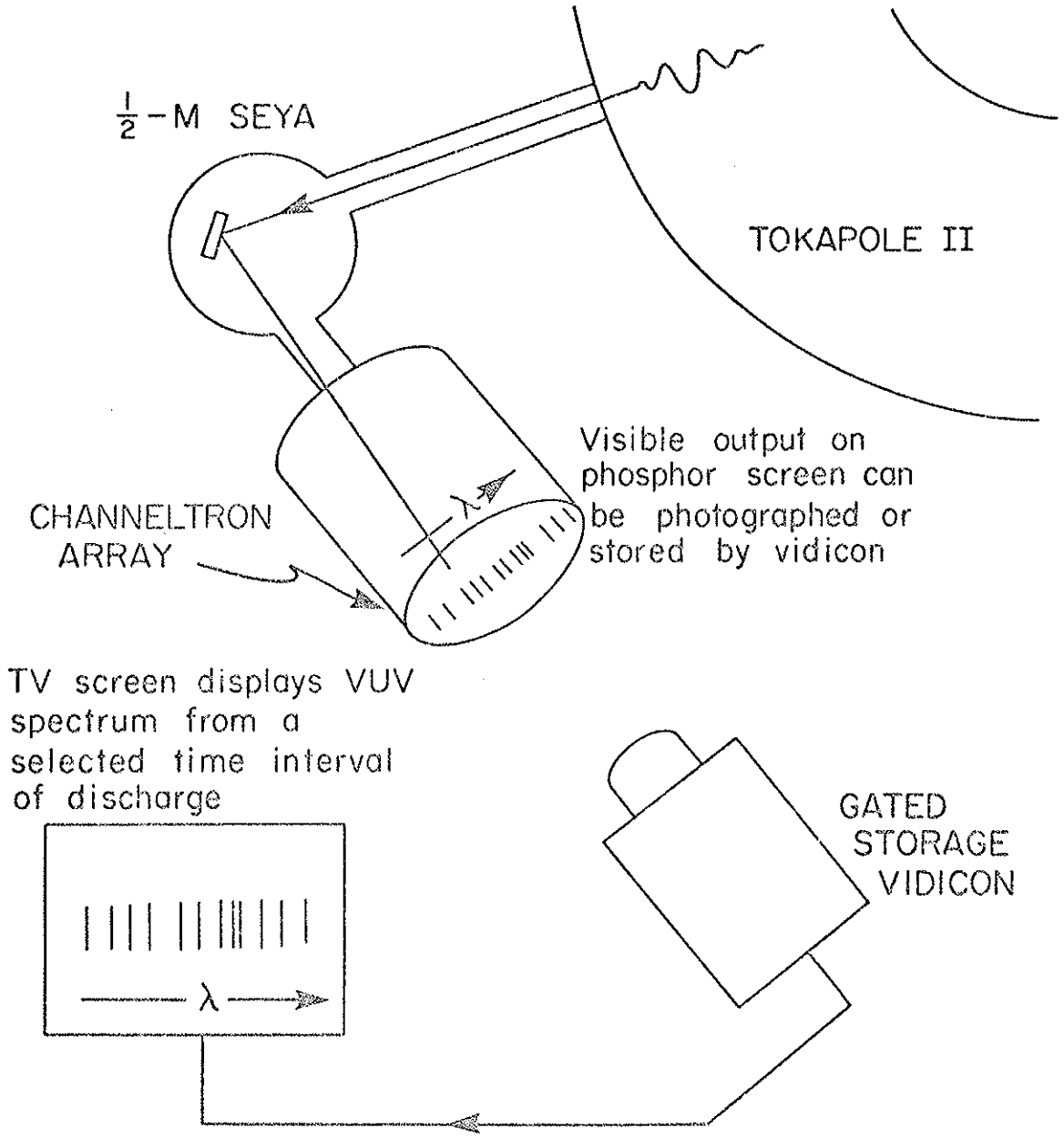

Channeltron Electron Multiplier Array which will also be called a CEMA or channeltron array. It consists of thousands of glass tubes of diameter 45μ which are internally coated with a secondary emitting semiconductor material and which are placed side by side as illustrated schematically in Fig.3-2a. Fig. 3-2b shows a side view of one of the tubes. A potential difference of ~1 kV is applied between the ends of the tube. Photons incident inside the tube produce secondary electrons which are accelerated toward the positive end of the channel and continue to produce more secondary electrons as they collide with the walls of the tube. Typically, 10^3 - 10^4 electrons are produced for each incident photon. Some microchannel plates, including the one used on the 1/2-m Seya, have a phosphor-coated screen which is at a positive potential (~5 kV) with respect to the positive end of the channels. The electrons strike this screen, produce visible photons, and the result is that one VUV photon has been converted into visible light. Fig. 3-2a shows how several channels produce a visible image of a VUV spectral line. Microchannel plates have a sensitivity range of about 2-1500 Å. The CEMA has 18 detecting elements/mm.

A photographic film can be exposed to the phosphor screen for the duration of a discharge to produce a record of all plasma VUV spectral lines in the range of accessibility. Since the phosphor,type P-11, has a useful time response of less than 1 μsec, it can be used to provide information on the time evolution of the VUV spectrum and this has been done in the manner illustrated in Fig.3-1. A gated storage vidicon (Quantex Integrating Digital TV System) can be turned on for short time periods during the discharge. (It can be triggered whenever desired

Fig. 3-2a: End view of channels in micro-channel plate (CEMA).

Fig. 3-2b: Side view of one channel in CEMA. Phosphor screen and biasing power supplies are illustrated.

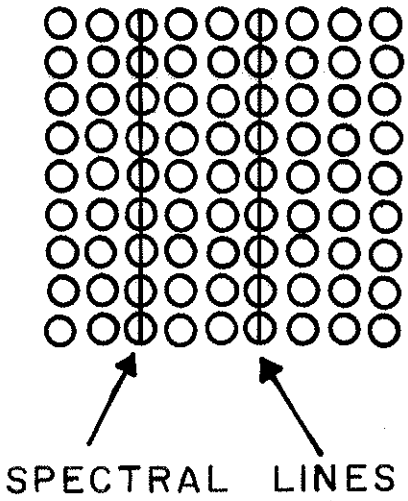

CEMA

END VIEW
of
CHANNELS

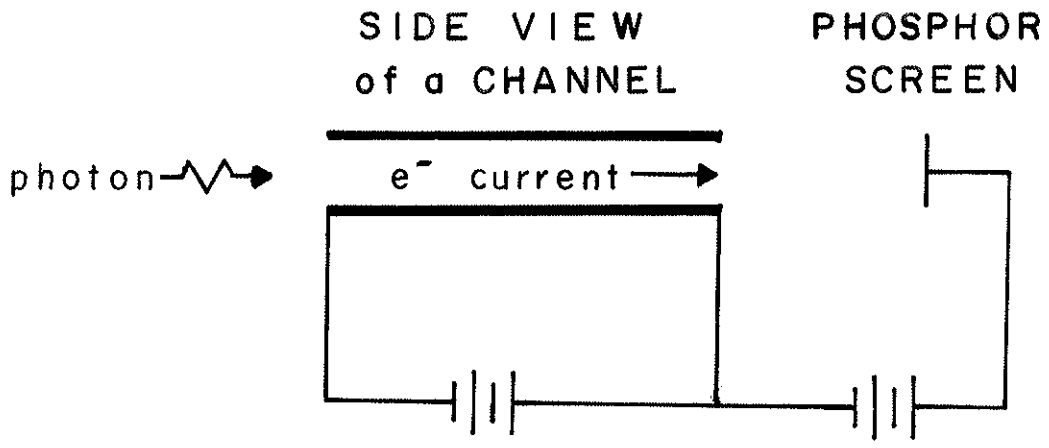

and maintained in the on condition for periods of 5 μsec - 100 msec.) During the time that the vidicon is on, it views the phosphor screen and stores in its memory all of the observed information. A continuous display of the contents of the memory, a picture of the spectral lines from the CEMA, is produced on the TV screen, and this can be photographed. Clearly, with a small number of discharges, the CEMA and vidicon can be used to provide a series of pictures, which show the temporal evolution of the VUV spectrum. The vidicon camera has 200 x 256 elements.

As it is set up, the 1/2-m Seya is capable of a resolution of 1-2 Å at the center of the spectrum. If phosphor blume is avoided, the CEMA has a resolution of 1-2 Å. The typical resolution has been 2-4 Å for these experiments. The affect of the vidicon on the system resolution can be controlled by use of a lens.

C. 1-m Seya-Namioka Monochromator

A 1-m Seya-Namioka monochromator has been used to obtain detailed quantitative and qualitative information on individual spectral lines. This instrument's main features were conceived by Professors R. Dexter, C. Pruett, and J. Taylor, it was designed by Dr. C. Pruett, and the detailed design and construction were performed by the University of Wisconsin Physical Sciences Laboratory.

This device has adjustable entrance and exit slits and has a 1440 line/mm concave gold grating, blazed at 700 Å, with a radius of curvature of 1 meter and a reciprocal linear dispersion at the exit slit of 6 Å/mm.

This instrument is equipped with two detectors. One is an EMI

model 9643/2B windowless electron multiplier with Cu-Be dynodes which are sensitive to photons in the 200-1300 Å range. It is not sensitive to visible wavelength photons which become increasingly bothersome as scattered light when the monochromator is observing small wavelengths. An internal mirror can be used to deflect photons into a second detector. This detector consists of a sodium salicylate phosphor, which converts vacuum UV photons into visible photons in a wavelength range which is peaked at 4200 Å,[2] and of a standard visible photomultiplier tube with an S-11 response (peaked near 4000 Å) which is then used to observe the visible photons. The quantum efficiency of sodium salicylate is relatively flat at roughly 65% for the wavelength range 3400-4000 Å, and the phosphor decay time is ~7-12 nsec.[2]

This type of detector is very convenient as it replaces an open tube, whose dynodes are easily degraded by contact with water vapor and oil. The visible PMT used in this combination is an EMI model 9635B.

The one-meter instrument was absolutely intensity calibrated so that for a given signal, the number of photons striking the grating was known. The details of the calibration procedure can be found elsewhere.[1,3]

D. Filter-Detector Combinations

A useful diagnostic has been a combination of a filter which transmits photons in a small wavelength range and an appropriate detector to convert the photons into an electrical signal. Such an arrangement is compact and can be mounted on a swivel port and used to obtain spatial data on the origin of impurity radiation. The drawback is that such a detector observes several spectral lines at one time.

In the near ultraviolet and visible, interference filters with passbands of about 100-200 Å are used in combination with a PMT. In addition, filters designed specifically to pass the resonance lines of CuI, AlI, CrI, and BeI can be used to observe metal production in the plasma.

The choice of filters in the VUV is very limited. Lithium fluoride is used to transmit to about 1100 Å. For shorter wavelengths, thin, fragile films are used to transmit in various regions of interest. VUV filters used on Tokapole II and their passbands have been: Al: 1% Si alloy (120-900 Å), LiF (1100 Å - visible), Be (110-700 Å), and polypropylene (40-210 Å). Detectors used for these filters are channeltrons, which are simply larger versions of the individual tubes in the channeltron array, which has been described already. The main difficulty with the channeltrons is that they saturate at relatively low photon fluxes, although this can be prevented by reducing the high voltage on the detector.

A polypropylene filter has been the most useful of all. This material is cheap, transmits in the visible and usefully transmits between about 200 Å and 40 Å when stretched to sub-micron thickness. Since channeltrons are not sensitive to visible light, the polypropylene-channeltron combination is sensitive only to photons in the short wavelength soft x-ray region.

E. Residual Gas Analyzer

A Veeco SPI-10 monopole residual gas analyzer (RGA) is used to identify the gases present in the vacuum chamber. Its day-to-day function is to identify the presence of vacuum leaks, as the signature of a leak

is a nitrogen peak with small oxygen and argon peaks. In addition, the RGA is used to analyze the purity of hydrogen or other gases used in the vacuum chamber and to monitor the production of water vapor, methane, and carbon monoxide during discharge cleaning. This instrument has been used to study gas recycling in discharges on Tokapole I.[4] In conjunction with a stream of electrons used to desorb impurities from the vacuum chamber wall, it has been used to identify impurities present on the wall.[5] It was also used to study early wall-cleaning experiments in the Supported Octupole.[6]

F. Fast Ionization Gauge

A slightly modified Veeco RG 75K Bayard-Alpert ionization gauge has been mounted with a high conductance opening to the vacuum vessel. Its home-built power supply has been designed to provide a very well regulated electron emission current from the filament of the gauge. This gauge is used to follow fast pressure changes before, during, and after a discharge. It is also used to determine the filling pressure of H_2 and other gases which have been introduced into the machine by a fast-acting valve.

G. Plasma Current Monitor

Because of the presence of currents in the internal rings, it is difficult to measure the toroidal plasma current, which is about 20% of the current in the rings. Sprott has treated the plasma as a circuit element in the secondary of the ohmic heating transformer and developed an analog electronic circuit which determines the plasma current from measurements of the poloidal gap voltage and current in the primary of the transformer.[7,8] The most troublesome feature of this model is

an assumption that the plasma current flows only on the magnetic axis. Current flowing near the walls is over-estimated by a factor of nearly two. After a variety of measurements, however, the model has been shown to provide good results and probably is accurate to within 25%.

H. Rogowski Coils

A large Rogowski coil, with a square opening that measures 21.6 x 21.6 cm, can be rotated into the plasma. It surrounds as much as possible of the current flowing within the region bounded by the four internal rings and essentially surrounds all of the plasma current flowing within the separatrix created by the plasma. A smaller Rogowski coil, with an opening of area 4.0 cm^2 is installed in a swivel port and is used to obtain spatial data on the current density.

I. Microwave Interferometer

A 40 GHz phase shift microwave interferometer is used to measure the line-averaged electron density on the midcylinder. Although the cut-off density at this frequency is 2 x 10^{13} cm^{-3}, the signal is cut off at a density about half of that. Reasons for the early cutoff might be refraction of the microwave beam, reflections at steep density gradients, or scattering by turbulence. A 70 GHz interferometer will be installed in an attempt to avoid these problems.

J. Langmuir Probes

For operation of the machine in the octupole mode, a specially-shaped Langmuir probe, the line-average probe, is permanently situated in the bridge region and measures the ion saturation current averaged over all flux surfaces. A second electrode has been installed in the machine, and in normal operation the line-average probe is biased with

respect to this electrode and is operated as a double probe. In tokamak operation, this probe yields a density which is about 5 times smaller than the central density, and in fact it gives the density in what will be called the scrape-off region.

To obtain information on spatial variations of ion saturation current, electron density, and electron temperature, conventional single-tipped Langmuir probes, double probes, and triple probes are used in swivel ports to scan the plasma. Use of these and other electrical probes has been complicated by the fact that they are easily damaged in the hot plasma and because they produce considerable perturbations in the central current channel and may alter the parameters which they are intended to measure.

K. Electric Field Probe

To measure the toroidal electric field strength as a function of space, an electric field probe is used.[8] It consists of a single turn of wire, and is oriented so that the plane of the wire is perpendicular to the poloidal magnetic flux. The measurement technique is described in Reference 8.

L. Magnetic Probes

A magnetic or $\dot{B}$ probe consists of a coil of wire, and it measures the time rate of change of magnetic flux through the plane of the coil. The signal from such a probe has been time-integrated and used to obtain experimental poloidal flux plots.[9] Magnetic probes are used to observe magnetic fluctuations. A large coil, placed near a window, has been used to measure poloidal magnetic field fluctuations outside of the machine, and this coil is simply a monitor of MHD activity in the plasma.

M. External Field Measurements

The poloidal or toroidal gap voltage is measured directly by connecting an oscilloscope or analog-to-digital converter directly across the appropriate gap. Current in the poloidal field primary is determined by measuring the voltage across a resistor in series with the primary. The toroidal magnetic field is measured by integrating the toroidal gap voltage over time.

N. Computer

A PDP 11/20 digital computer and a set of Biomation analog-to-digital converters are used for data acquisition and reduction. The Biomation units will be replaced with Camac modules.

REFERENCES

1. R. N. Dexter, R. J. Groebner, University of Wisconsin Plasma Studies PLP 768, 1978.

2. J. A. R. Samson, Techniques of Vacuum Ultraviolet Spectroscopy (John Wiley & Sons, Inc., New York, 1967).

3. R. J. Groebner, University of Wisconsin Plasma Studies PLP 791, 1979.

4. R. J. Groebner, University of Wisconsin Plasma Studies PLP 742, 1978.

5. R. J. Groebner, University of Wisconsin Plasma Studies PLP 650, 1975.

6. R. Droll, R. Groebner, University of Wisconsin Plasma Studies PLP 720, 1977.

7. J. C. Sprott, University of Wisconsin Plasma Studies PLP 712, 1977.

8. S. C. Prager, J. C. Sprott, T. H. Osborne, K. Miller, University of Wisconsin Plasma Studies PLP 756, 1978.

9. B. Lipschultz, et al, University of Wisconsin Plasma Studies PLP 764, 1978.

CHAPTER FOUR

SPECTROSCOPY PRIMER

This chapter presents an introduction to the analysis of plasmas by spectroscopic techniques. It includes discussions of line radiation, of the coronal equilibrium and time-dependent coronal models used to interpret plasma emissions, of techniques used to obtain information on electron temperature, radiated power, and impurity densities and influxes, and of basic radiometric concepts which are needed to convert signals from a detector into quantitative information about radiation in a plasma.

A. Introduction to the VUV Region

In the electromagnetic spectrum, the 4000-7000 Å region is referred to as the visible region, the 2000-4000 Å region as the near ultraviolet, and the 2-2000 Å region as the vacuum ultraviolet. The vacuum ultraviolet range of wavelengths is sometimes subdivided into the extreme ultraviolet (EUV), extending from 300 Å to 1000 Å, and the soft x-ray region (SXR), extending from 2 Å to 300 Å.

The atmosphere strongly absorbs radiation at wavelengths shorter than about 2000 Å, so that spectrometers used below 2000 Å must normally be evacuated (hence, the name "vacuum ultraviolet"). Some gases, such as nitrogen and the noble gases transmit for a few hundred Å below 2000 Å, and spectrometers are occasionally filled with those gases for work in the accessible wavelength regions.

The choice of transmitting and reflecting materials in the VUV is very restricted, and the efficiencies of available optical materials

is seldom near 100%. As a result, the number of elements in a VUV spectrometer is kept as low as possible; typically, the only optical element is a concave grating, which disperses light and forms a focused image of the entrance slit on the exit plane. Usually, the spectrometer is connected directly to the radiation source with no intervening window. The performance of most materials and detectors in the VUV is seriously degraded by exposure to hydrocarbons (from vacuum pump oil, for instance) and by exposure to water vapor. Therefore, VUV materials and detectors must be maintained in clean, dry environments. For more information about useful materials or experimental technique for the VUV, the interested reader is referred to Refs. 1-3.

B. Line Radiation

Most of the electromagnetic energy radiated from tokamak plasmas is in the form of line radiation. (Bremsstrahlung becomes increasingly important as the average plasma electron energy increases.) Line radiation is a description of the emission at discrete wavelengths from excited atoms or ions; these photons produce the familiar spectral lines. Photons radiated from tokamak plasmas have energies which are typically comparable to or less than the average electron energy. Thus, the 100 eV electrons in Tokapole II discharges produce photons primarily in the 10 - 100 eV (1200 - 120 Å) range.

Line radiation during the ionization phase of a discharge is produced mainly by hydrogen atoms. After the hydrogen is ionized, it can no longer emit line radiation, and the bulk of the line radiation in a tokamak discharge is produced by impurity ions which are not fully ionized. Plasma electrons can strip, from ions, electrons whose ionization

energies are less than or comparable to the average energy of the plasma electrons. Table 4-1,which lists the ionization energies of the oxygen ions,[4] helps to illustrate this idea. (The spectroscopic notation OI refers to atomic oxygen, OII refers to O^+, etc.) Oxygen ions in charge states up to and including OVII can be produced by the 100 eV electrons in Tokapole plasmas; however, the plasma is unlikely to remove the OVII optical electron, which has an ionization energy of 739 eV, to form OVIII. All of the oxygen ions in Tokapole plasmas, therefore, produce line radiation. Other impurities in Tokapole discharges behave similarly, both qualitatively and quantitatively, to oxygen.

TABLE 4 - 1

ION	IONIZATION ENERGY (eV)
OI	13.6
OII	35.1
OIII	54.9
OIV	77.4
OV	113.0
OVI	138.1
OVII	739.1
OVIII	871.4

The character of the line radiation from a typical impurity ion will be illustrated by an analysis of the energy level diagram of OV[4-6] (Fig. 4-1). The term diagram is split into singlets and triplets, corresponding respectively to a total spin S of 0 or 1, and there are few transitions of any kind between the singlets and triplets. Nearly all of the OV ions are in the $1s^2 2s^2\ {}^1S_o$ ground state or the $1s^2 2s2p\ {}^3P^o$

Fig. 4-1: Energy level diagram of OV.

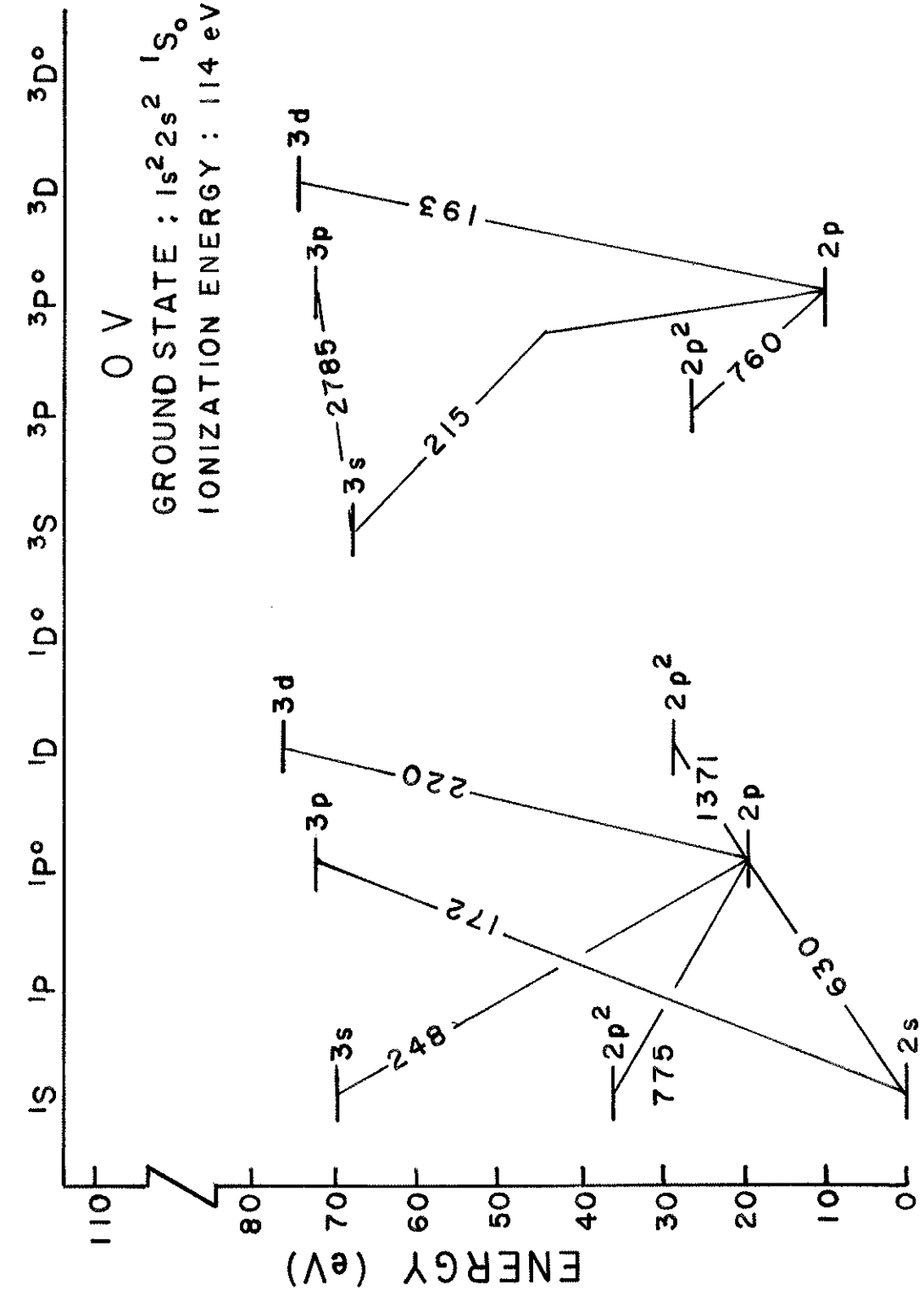
O V
GROUND STATE : $1s^2 2s^2\ {}^1S_o$
IONIZATION ENERGY : 114 eV
^1S ^1P $^1P^o$ ^1D $^1D^o$ ^3S ^3P $^3P^o$ ^3D $^3D^o$
ENERGY (eV)
0 10 20 30 40 50 60 70 80 110
2s
2p
3s
3p
3d
$2p^2$
630
172
220
1371
248
775
2785
215
193
760

metastable state. In Fig. 4-1, the designations of each level refer to the electron(s) which must be excited to produce the level.

The singlet system will now be discussed. The 2p state has the highest probability of any level of being excited (by electron collisions) from the ground state. For electron temperatures above 10 eV, the electron excitation rate coefficient $\langle \sigma V \rangle_{exc}$ is about 2×10^{-8} cm^3/sec.[7] If, in addition, the electron density n is 1×10^{13} cm^{-3}, then an OV ion will be excited from the 2s to the 2p level in about 5×10^{-6} sec $(1/n \langle \sigma V \rangle_{exc})$. The ion de-excites in about 3×10^{-10} sec,[4] and so a very bright line is produced at 630 Å. (Transitions for which the principal quantum number n does not change are called $\Delta n = 0$ transitions and typically produce the brightest lines for ions.)

Other states in the n = 2 shell are the $2p^2\ {}^1S$ and the $2p^2\ {}^1D$ levels. These levels can be excited from the ground state or the metastable ${}^3P^o$ level,[6] but the excitation rates to those levels are smaller than to the $2p\ {}^1P^o$ term. Excitations to the n = 3 shell start to become important only when the average electron energy is comparable to the required excitation energy of 70 eV. Even then, the excitation rates to these levels is roughly an order of magnitude smaller than those to the 2p level. Thus, the 630 Å line is normally the brightest line of the singlets.

Similar considerations apply to the OV triplets and to the other important ions in Tokapole discharges. The dominant line radiation in Tokapole discharges occurs at wavelengths shorter than 1500 Å and can only be studied by the techniques of VUV spectroscopy.

C. Coronal Equilibrium

To make quantitative measurements from observed spectral lines, knowledge of the population densities of excited states of an ion and of the population densities of ions in different ionization states is needed. These populations are simply calculated if the plasma is in thermodynamic equilibrium,[3,8-10] but the energy levels and ionization states of ions in tokamak plasmas are not in thermodynamic equilibrium.[8,11]

The coronal model, originally devised to describe the low density, high temperature plasma of the solar corona, applies well to tokamak plasmas for which the relevant atomic processes are in equilibrium. The basic assumptions of the model are the following:[8,9]

1) The electrons have a Maxwellian distribution. The ions have a mean velocity comparable to or less than that of the electrons so that excitation and ionization by the ions can be neglected.

2) The densities of the ions in excited levels are negligible compared to the densities of the ions in the ground states.

3) There is a balance between ionization by electron collisions and recombination by the radiative and dielectronic recombination processes. This is expressed as

$$n_e n_z^g \, S(T_e,z,g) = n_e n_{z+1}^g \, \alpha(T_e,z+1,g) \qquad (4\text{-}1)$$

where n_z^g is the density of ions of charge z in the ground state g, S is the ionization rate coefficient for these ions, and α is the sum of the dielectronic and radiative recombination rate coefficients for the ions of charge z+1. A rate coefficient has units of cm^3/sec and is a Maxwel-

lian average over the cross section for the given atomic process. For example,

$$S(T_e,z,g) = \langle \sigma\ (v,z,g) \rangle \tag{4-2}$$

where v is the electron velocity, σ is the cross section for ionization of ion z and T_e is the electron temperature.

4) The population of excited level m of an ion is determined by a balance between the rate of electron excitations to level m from the ground state and the rate of spontaneous radiative decay of the excited level:

$$n_e n_z^g\ Q_{g,m}(T_e) = n_z^m \sum_{q<m} A_{m,q} \tag{4-3}$$

where $Q_{g,m}$ is the electron excitation rate coefficient from the ground state to level m, n_z^m is the density of ions of charge z in level m and $A_{m,q}$ is the transition probability for spontaneous emission from level m to level q, where level q has a lower energy than level m.

5) The emission E of a line produced by a transition between levels m and j is given by

$$E_{m,j} = n_z^m A_{m,j} = \Gamma_{m,j}\ n_e n_z^g\ Q_{g,m}(T_e) \tag{4-4}$$

where $E_{m,j}$ is the number of photons being emitted from a cubic cm of the plasma per second (units of photons/sec/cm^3) by transitions which take level m to j and $\Gamma_{m,j}$ is the branching ratio. This is expressed as

$$\Gamma_{m,j} = \frac{A_{m,j}}{\sum_{q<m} A_{m,q}} \tag{4-5}$$

Caution is often necessary in applying the coronal equilibrium model. Equation (4-1), which describes the population densities of the

various ionization states of an element, is applicable only when the electron temperature, the electron density, and the densities of the ionization states are not changing. McWhirter provides a general estimate of the relaxation time τ for the achievement of ionization state coronal equilibrium[8] of

$$\tau \simeq \frac{10^{12}}{n_e} \text{ sec}, \tag{4-6}$$

where n_e is in cm^{-3}. The relaxation time is about 0.1 sec for Tokapole plasmas. Clearly, Eq. 4-1 cannot be applied to Tokapole plasmas, although it can be used to provide a lower estimate of T_e.

In general, coronal equilibrium of the excited states of an ion is achieved relatively quickly (on the order of 10^{-8} sec),so that Eqs. (4-3) and (4-4) are appropriate for the time scales of tokamak plasmas. However, the application of Eqs. (4-3) and (4-4) to any level other than the first excited level might be incorrect since there are other mechanisms which could populate the level. Excitation from metastable levels and cascading from higher excited levels are two such possibilities.[6,8,12-15] The model normally works well for the first excited states of ions and for lithium-like ions, which have three electrons and no metastable levels, and it is applicable to other levels in favorable cases.

D. Time Dependent Coronal Model

To calculate the densities of the ionization states of an element for a plasma in which ionization equilibrium has not been obtained, the following set of rate equations must be solved:[8,15]

$$\frac{dn_o}{dt} = -S_o(T_e)\ n_e\ n_o + \alpha_1(T_e)\ n_e n_1 - n_o/\tau + \phi_o$$

$$\frac{dn_z}{dt} = -S_z(T_e)\ n_e n_z - \alpha_z(T_e)\ n_e n_z + S_{z-1}(T_e)\ n_e n_{z-1} + \alpha_{z+1}(T_e) n_e n_{z+1} - n_z/\tau$$

$$\frac{dn_{zl}}{dt} = -\alpha_{zl}(T_e)\ n_e n_{zl} + S_{zl-1}(T_e)\ n_{zl-1}\ n_e - n_{zl}/\tau \quad . \qquad (4\text{-}7)$$

In these equations, n_z is the density of ions of charge z, n_e is the electron density and is a function of time, τ is the particle confinement time, ϕ is the influx rate of fresh impurities, which are assumed to be in the atomic state, and zl refers to the most highly charged ion (the limit ion) produced by the discharge. S_z is the ionization rate coefficient for ionization of ion z and α_z is the recombination rate coefficient for ion z going to ion z-1.

The set of equations (4-7) has two useful limits for the steady state case ($dn_z/dt = 0$ for all z). If τ is large enough that the terms n_z/τ can be neglected, and if the source term ϕ_o can be neglected, then the set (4-7) reduces to Eq. (4-1) for all z. This situation is well approached in the hot core of a long-lived tokamak discharge.[15]

Another limit of the set (4-7) can be applied to the recycling impurities, which are in cylindrical shells[16] at the periphery of a tokamak discharge. For this case, the particle confinement time is low, the source term cannot be neglected, and T_e is sufficiently high that recombination can be neglected.

In this limit, τ is sufficiently small so that for some limit ion of charge zl, the following relation is true:

$$S_{zl} < 1/n_e\tau < S_{zl-1} <. . . . . < S_o . \qquad (4-8)$$

This condition is actually met in Tokapole plasmas where OVII is the limit ion for the oxygen ions, and the condition means that the limit ions are lost before they can be ionized to the next charge state. If recombination can be neglected, then the set of equations (4-7) becomes in steady state

$$\begin{aligned} \phi_o &= n_o\, n_e\, S_o + n_o/\tau \\ 0 &= n_z\, n_e\, S_z - n_{z-1}\, n_e\, S_{z-1} + n_z/\tau \ , \ 1 \le z \le zl-1 \\ 0 &= -n_{zl-1}\, n_e\, S_{zl-1} + n_{zl}/\tau \ . \end{aligned} \qquad (4-9)$$

These equations are written this way to show clearly that, when added up, they yield

$$\phi_o = \sum_{z=0}^{zl} n_z/\tau = n/\tau \ , \qquad (4-10)$$

where n is the total density of all ions of the chemical species under consideration. For the recycling plasma, the source term is equal to the loss term.

Equations (4-9) can be rewritten

$$\begin{aligned} \phi_o &= n_o\, n_e\, (S_o + 1/n_e\tau\,) \\ n_{z-1}\, S_{z-1} &= n_z\, (S_z + 1/n_e\tau), 1 \le z \le zl-1 \\ n_{zl-1}\, S_{zl-1} &= n_{zl}/n_e\, \tau. \end{aligned} \qquad (4-11)$$

Condition (4-8) has the result that $1/n_e\,\tau$ can be neglected for all ions except zl. Thus (4-11) becomes

$$\phi_o = n_o\, n_e\, S_o$$

$$n_{z-1}\, S_{z-1} = n_z\, S_z\,, \qquad 1 \leq z \leq zl - 1$$

$$n_{zl-1}\, S_{zl-1} = n_{zl}/n_e\, \tau, \tag{4-12}$$

with the consequence that

$$\phi_o = S_z\, n_z\, n_e\,, \quad 0 \leq z \leq zl-1\,. \tag{4-13}$$

The results of sections C and D will now be summarized. A tokamak plasma cannot be treated as though the ionization levels and energy levels of impurity ions were in thermal equilibrium, but rather the atomic processes governing the population of these levels are determined by a blend of the coronal equilibrium and time-dependent coronal models. The time evolution of the densities of impurities which are initially present in the plasma are described by the rate equations (4-7). During the steady state phase of the discharge, the densities of impurities at the center of the discharge (for sufficiently long times) are described by the coronal equilibrium condition (4-1), while the influx of impurities in the recycling peripheral shell is determined by equation (4-13). Finally, the actual densities of the ions can be calculated from equation (4-4) if the emission of an appropriate spectral line is known.

For situations in which the coronal equilibrium among energy levels of equation (4-3) is too simplistic, a more complicated approach must be taken in which the atomic processes which populate the energy levels under consideration are described in detail.[6,8,12-14] To more carefully treat the behavior of the impurity ionization states, the set of equations (4-7) is expanded to one dimension, the radial diffusion

of impurities is included, and various diffusion coefficients are used to obtain agreement between the calculations and the observations.[17-19]

E. Spectroscopic Electron Temperature Measurements

Two techniques to determine T_e will be discussed. For cases in which two excited levels m and n of an ion are known to be populated only by excitation of the ground state, T_e can be determined from a measurement of the relative intensity of spectral lines produced by transitions from these levels. The relative intensity of the lines is obtained with the aid of Eq. (4-4):

$$\frac{E_{m,k}}{E_{n,j}} = \frac{\Gamma_{m,k}}{\Gamma_{n,j}} \frac{Q_{g,m}(T_e)}{Q_{g,n}(T_e)} \tag{4-14}$$

where level m decays to level k and n decays to j. This technique requires that levels m and n be separated by an energy comparable to the electron energy. Theoretical calculations are usually used to obtain the excitation rate coefficients, the branching ratios are known for a large number of transitions, and a relatively calibrated spectrometer is required to measure the ratio of the emissions of the two lines. The technique is particularly suitable for measurements of lithium-like ions (CIV, NV, or OVI, for example).

A procedure which can be used to infer T_e during the early phase of a tokamak discharge[15,19,20] is based on the set of rate equations (4-7). Experimental observations are made to determine the times of the ionization peaks of the ions of an impurity element, and the electron density is measured as a function of time. The impurities are assumed to be uniformly distributed so that all spatial effects are ignored in the calcu-

lation. Appropriate values for the particle influx rate and for the particle confinement time are assumed, although the calculation to be described is not strongly dependent on those numbers. Fairly good ionization rates and adequate recombination rates are available for use in the equations. In the simulation, $T_e(t)$ is varied until the predicted and observed times of the ionization peaks agree. This gives an electron temperature which is some volume average of the true T_e.

F. Radiated Power Measurements

Figure 4-2 shows the basic setup for measuring the radiated power. The plasma column is assumed to be of square cross section with a width of 2a, the column is centered on an x-y coordinate system, and θ is the plasma toroidal angle. The emission $E_\lambda(x,y,\theta)$ is the basic plasma parameter which is needed to determine the power radiated by a spectral line of wavelength λ. (Emission is the number of photons radiated per sec per cm^3.) The radiated power P_λ at the wavelength λ is obtained from an integration of the emission over the plasma volume V

$$P_\lambda = h\nu \int_V E_\lambda(x,y,\theta)\, dV \qquad (4\text{-}15)$$

where $h\nu$ is the energy of the photons. An assumption here is that the plasma is optically thin to this radiation, and this assumption is accurate for normal tokamak densities.

G. Radiometry -- Theory

A variety of measurements which has been discussed require a knowledge of the plasma emission E. A spectrometer measures the plasma brightness B, which is the line integral of E, and the science of radiometry must be invoked to provide a relation between E and B.

Fig. 4-2: Setup for radiated power measurements.

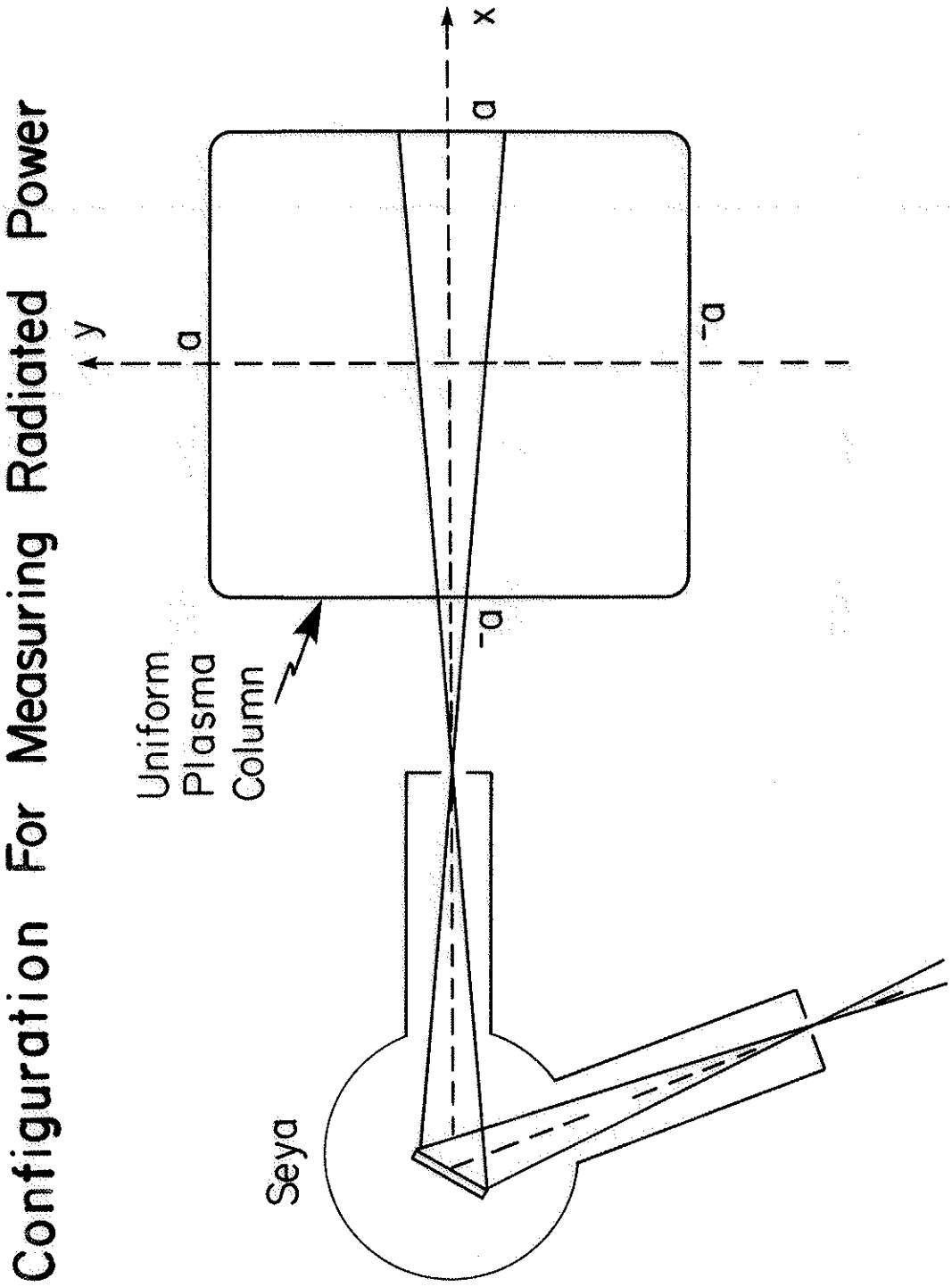
Configuration For Measuring Radiated Power
x
a
-a
y
a
-a
Uniform
Plasma
Column
Seya

This is done in the following way. A small radiating cube is assumed to be located on the x-axis of the plasma cross section (Fig. 4-2). This region has an emission E, sides of length dL and a volume $dV = dL^3$. Its photons are radiated into a solid angle of 4π steradians. The photon output of this region can also be characterized by its brightness dB, where

$$dB = \frac{1}{4\pi} EdL. \tag{4-16}$$

The brightness has units of photons per cm^2 per steradian per sec, and it is the number of photons emitted by the cube through one of its faces into a steradian per sec. As long as the photons are not absorbed by the medium through which they pass, brightness is an invariant quantity along any ray from the source region.[21] One consequence of this is that brightnesses of several source regions along a ray will add. Thus, the brightness of the plasma viewed along the x-axis, will be

$$B = \frac{1}{4\pi} \int_{-a}^{a} E(x,0)dx \tag{4-17}$$

where the integration is performed along the line of sight of the monochromator through the plasma.

The monochromator actually views a solid angle which is centered on the x-axis, and in principle the brightness of the plasma along all rays which pass through the entrance slit and intersect the grating must be known (Fig. 4-2). Clearly, for most cases the brightness will essentially be the same along all such rays, and B is given by Eq. (4-17).

In any calibration procedure, the actual flux of photons onto the grating must be determined. Figure 4-3a shows an extended source with area S and uniform brightness B and a detector of area D, whose

Fig. 4-3a: Source-Detector Geometry.

Fig. 4-3b: Extended source illuminating grating through slit. The area of the slit is the effective source area.

Fig. 4-3c: Two apertures between source and grating. The effective source area is a function of position on the grating.

Fig. 4-3d: Source does not fully illuminate grating. Effective source area is half of slit area.

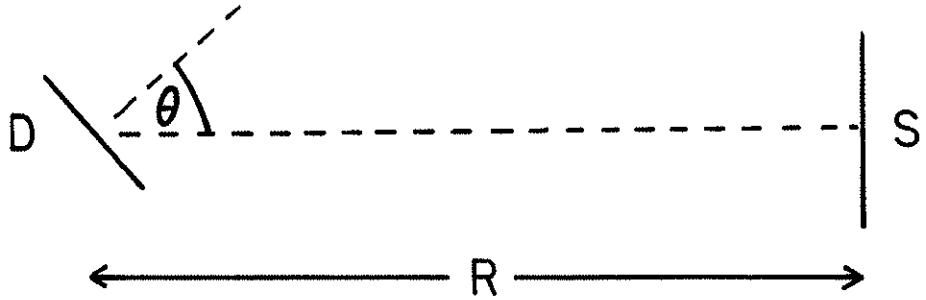
D
θ
S
R

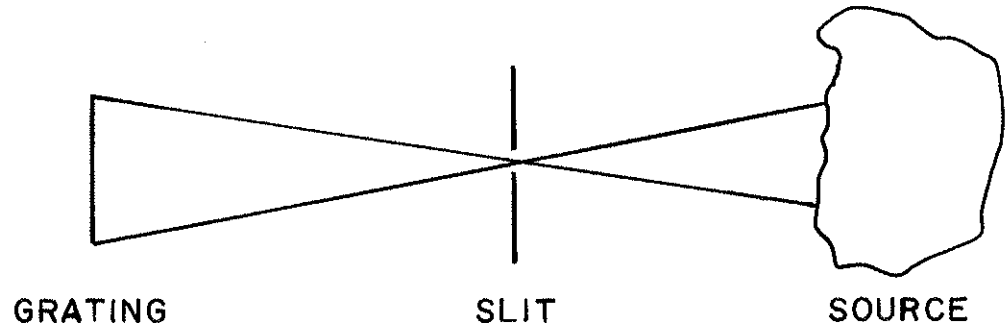
GRATING
SLIT
SOURCE

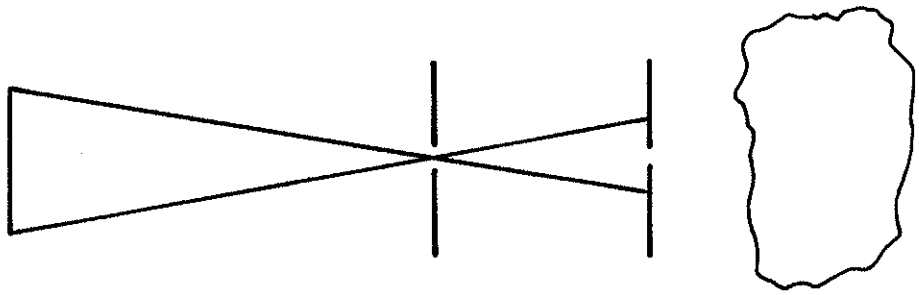

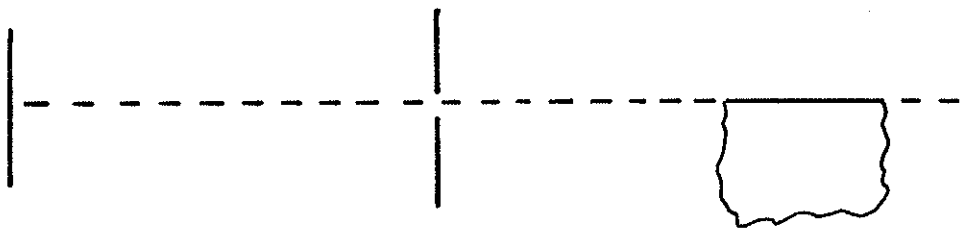

normal is at an angle θ with respect to the line joining the centers of the source and detector. Source and detector are separated by a distance R which is assumed to be large with respect to the dimensions of the source or the detector; thus, the source subtends the same solid angle $\Omega = S/R^2$ at all points on the detector and vice versa. The flux of photons F (number of photons per sec) incident on the detector is[21,22]

$$F = \frac{B\ DS\ \cos\theta}{R^2} \tag{4-18}$$

where $\frac{D\ S\ \cos\theta}{R^2}$ is sometimes called the etendue of the system.

Figure 4-3b shows an example in which an aperture is placed between a source and the detector. A grating is illuminated by a plasma through a slit. (The area of the grating is the detector area, since presumably all photons which strike the grating also pass into the PMT or other photon counting device.) As the figure is drawn, the grating is fully illuminated, since every part of the grating is illuminated by the source of brightness B. However, the effective source area is now the slit area, and the flux of photons onto the grating is given by Eq. (4-18) with S being the slit area.

Figure 4 -3c shows a case in which two apertures have been placed between the source and the detector. The aperture nearer to the source shadows portions of the second aperture from the source, so different portions of the detector view different effective areas of the source. The photon flux onto the grating can be determined only by an appropriate integral over the two apertures. Another type of problem is illustrated in Figure 4-3d; the source does not fully illuminate the detector. As drawn, this system can be treated by assuming that the area of the source

is half of the slit area.

To eliminate doubts as to the actual detector area in quantitative measurements, the grating should be fully illuminated (Fig. 4-4). Figure 4-4a illustrates a view from the top (looking down on narrow portion of the slit) of the grating-slit-source system. The grating is fully illuminated from this direction because the source fully fills the solid angle subtended by the grating at the slit.[2,23] Figure 4-4b shows a grating fully illuminated in the direction parallel to the slit's length, because the source subtends the region enclosed by the extreme rays of the figure.[2,23] This latter condition is more difficult to check than the first condition; the best procedure is to draw the optical system and all apertures to scale.

H. Radiometry -- Practical Application

References15 and 19 describe the standard techniques for obtaining quantitative data about impurities from spectroscopic observations. The first problem in quantitative spectroscopy is to determine the plasma emission from a knowledge of the plasma brightness. Equation (4-17) gives the desired relationship between E and B,

$$B = \frac{1}{4\pi} \int_{-a}^{a} E(x,0,\theta)\, dx \quad . \tag{4-17}$$

Clearly, E cannot be determined as a function of space from a single measurement of B. Furthermore, there is not even a unique solution E which will satisfy Eq. (4-17). A reasonable simplification is the assumption that E is axisymmetric or independent of toroidal angle. However, this is usually not completely true. In particular, there generally is more light coming from the region near the limiter than from

Fig. 4-4a: Top view of a grating which is fully illuminated by an extended source. Rays from edge of grating which pass through slit intersect the source.

Fig. 4-4b: Side view of fully illuminated grating. The extreme rays AA' and BB', which graze the edge of the grating and the edge of the slit, intersect the source.

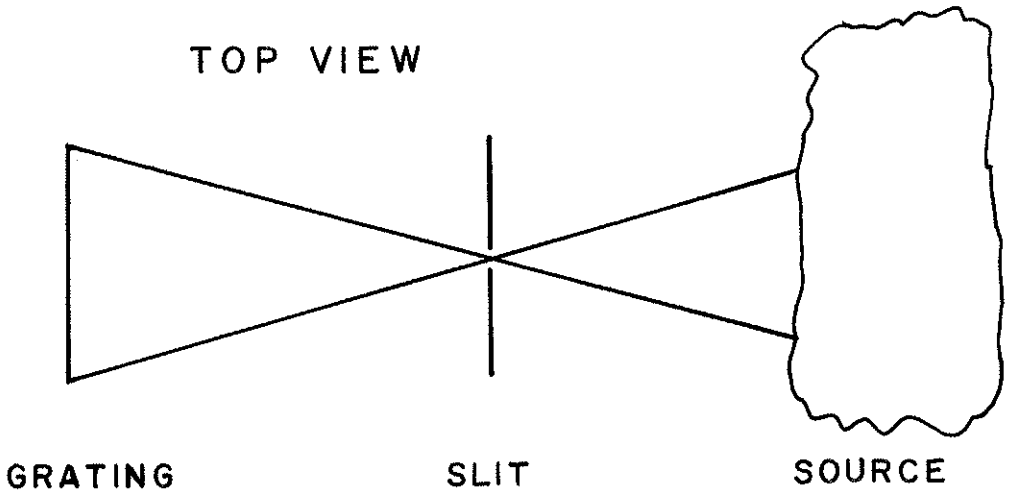
TOP VIEW
GRATING
SLIT
SOURCE

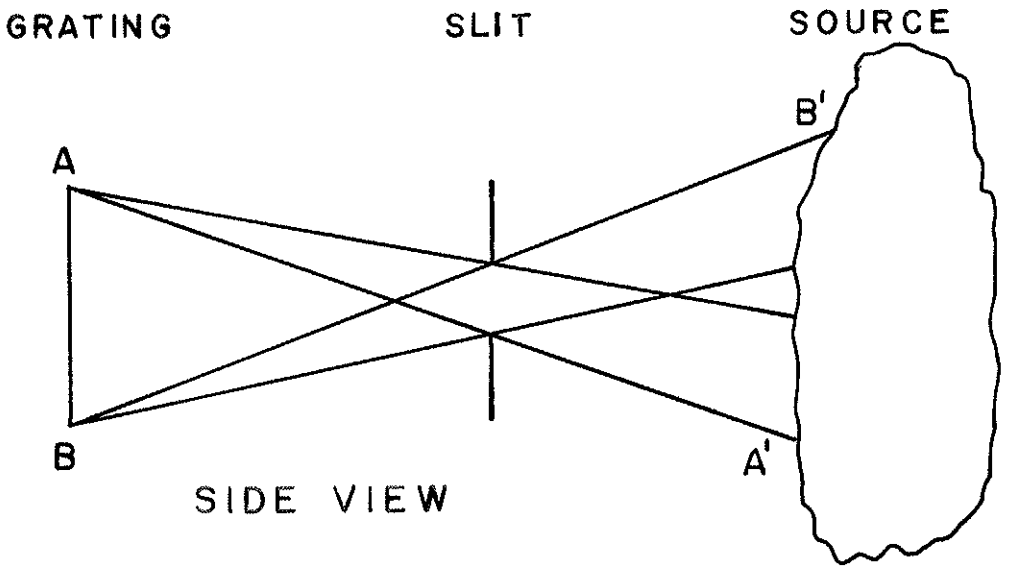
GRATING
SLIT
SOURCE
B'
A
B
A'
SIDE VIEW

other regions in a standard tokamak, and if gas is injected into a plasma, the emission is increased in the vicinity of the injection.

In tokamaks, cylindrical symmetry of the emission is usually assumed. If observations of the brightness are made along several chords, then the brightness data can be deconvoluted by an Abel inversion to yield emission as a function of minor radius.[10,16,24,25] Presumably, the emission in a Tokapole discharge has square symmetry. This has yet to be proven, but if it is true, the Tokapole brightness will probably be more difficult to deconvolute than the data in the circular tokamak case. Algebraic reconstruction techniques[26,27] might be needed to deconvolute Tokapole spatial emissions.

In the majority of cases Eq. (4-17) is simplified by the assumption that E is constant along a magnetic flux surface (has square symmetry in the Tokapole) and that the emission has some average value, which will simply be denoted as E, over a spatial region of width Δr. The emission is 0 outside that region. Since the spectrometer's line of sight passes through this region twice, Eq. (4-17) can be written as

$$B = (1/4\pi)(2E\ \Delta r) = \left(\frac{E\Delta r}{2\pi}\right) . \qquad (4\text{-}19)$$

Impurity measurements will be discussed for two limiting cases: the impurities are uniformly distributed throughout the plasma which has a width 2a, or the impurities are localized in shells centered on the magnetic axis. In the first case, $\Delta r = a$ and Eq. (4-19) becomes

$$B = \frac{aE}{2\pi} \qquad (4\text{-}20)$$

Uniform impurity distribution characteristically occurs in the early phases of a tokamak discharge, and Eqs. (4-4) and (4-20) can be combined

to give an expression for the average ion impurity density

$$B = \frac{a\Gamma\, n_z\, n_e\, Q}{2\pi} \quad , \tag{4-21}$$

where n_e is the line-averaged electron density.

The power radiated by the transition under observation is obtained from Eq. (4-15) by removing E from the integral, substituting for it from Eq. (4-20), and multiplying by the plasma volume $4\, a^2\, 2\pi\, R$:

$$P = 16\, \pi^2\, h\nu\, B\, a\, R \tag{4-22}$$

where R is the plasma major radius. Equations (4-13) and (4-4) can be combined to give an expression for the impurity influx term ϕ_o;

$$\phi_o = \frac{S_z\, E}{\Gamma\, Q} \quad , \tag{4-23}$$

and in turn Eq. (4-23) can be combined with (4-20) to yield an expression for ϕ_o in terms of a measurable quantity (B) and other known quantities:

$$\phi_o = \frac{2\pi\, S_z B}{\Gamma\, Q\, a} \tag{4-24}$$

which is the number of particles arriving in each cm^3 of the plasma per sec. For this case, the flux ψ_o of particles (particles/cm^2/sec) at the plasma periphery is[15]

$$\psi_o = \frac{a\, \phi_o}{2} = \frac{\pi\, S_z\, B}{\Gamma\, Q} \tag{4-25}$$

The second case of interest is that of a well developed tokamak plasma in which impurity ions are found in shells surrounding the central hot current channel, and a particular shell occurs in a region where T_e is less than or on the order of the ionization potential of the ions in question. As indicated above, the shell has square symmetry, E is constant inside the shell and 0 outside, the shell is centered at a distance ρ from the

center of the current channel and has a width Δr (Fig. 4-5). The brightness is still given by Eq. (4-19), which can be combined with (4-15) to yield the radiated power in terms of B. As in the previous calculation of power, E can be removed from the integral, so the integral is then over the shell volume, which is $\Delta r\ 8\rho\ 2\pi\ R$. The power radiated from the shell is:

$$P = 16\pi\ h\nu\ \ B\ \rho\ \ 2\pi\ R. \tag{4-26}$$

The influx of impurities into the shell is given by (4-23) and (4-19):

$$\phi_o = \frac{2\pi\ S_z\ B}{\Gamma\ Q\ \Delta r}\ , \tag{4-27}$$

while the flux of impurities at the plasma edge is $\psi_o = \phi_o\ \Delta r$ or

$$\psi_o = \frac{2\pi\ S_z\ B}{\Gamma\ Q}\ . \tag{4-28}$$

Most of these formulas have been derived in slightly different and more rigorous ways in Refs. 15 and 19. The results here are the same as the standard results, when they are transformed into square geometry.

Fig. 4-5: Impurity shell of width Δr. Center of shell is at minor radius ρ.

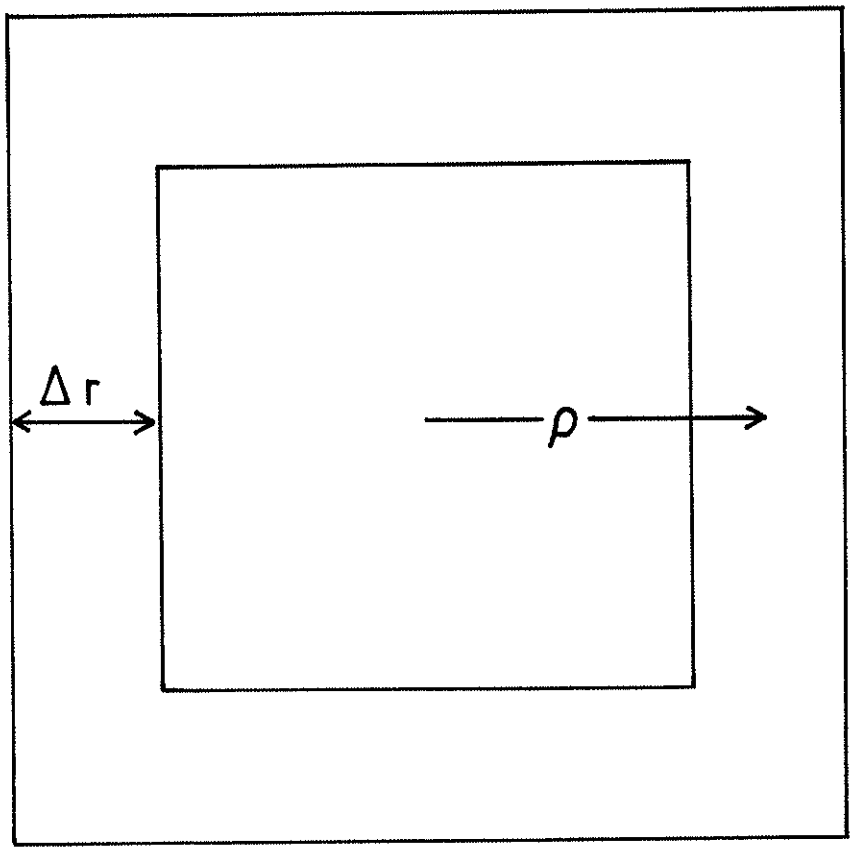

IMPURITY SHELL

REFERENCES

1. J. A. R. Samson, Techniques of Vacuum Ultraviolet Spectroscopy (John Wiley & Sons, Inc., New York 1967).

2. A. N. Zaidel, E. Ya. Shreider, Vacuum Ultraviolet Spectroscopy (Ann Arbor - Humphrey Science Publishers, Ann Arbor, 1970).

3. A. P. Thorne, Spectrophysics (Chapman & Hall Ltd., London, 1974).

4. W. L. Wiese, M. W. Smith, B. M. Glennon, Atomic Transition Probabilities, NSRDS-NBS 4 Report, National Bureau of Standards, 1966, p. 108.

5. S. Bashkin, J. O. Stoner, Jr., Atomic Energy Levels & Grotrian Diagrams 1 (North-Holland Publishing Co., Amsterdam, 1975) p. 190.

6. A. H. Gabriel, C. Jordan in Case Studies in Atomic Collision Physics II, M. R. C. McDowell, E. W. McDaniel (eds.) (North-Holland Publishing Co., Amsterdam, 1972), Ch. 4.

7. J. Davis, P. C. Kepple, M. Blaha, J. Quant. Spectrosc. Radiat. Transfer 15, 1145 (1975).

8. R. W. P. McWhirter in Plasma Diagnostic Techniques, R. H. Huddlestone, S. L. Leonard (eds.) (Academic Press, New York, 1965).

9. H. R. Griem, Plasma Spectroscopy (McGraw-Hill Book Company, New York, 1964).

10. F. Cabannes, J. Chapelle in Reactions under Plasma Conditions, Vol. 1, M. Venugopalan (ed.) (John Wiley & Sons, Inc., New York, 1971).

11. R. J. Groebner, R. N. Dexter, University of Wisconsin Plasma Physics Studies PLP 769, 1978.

12. S. Suckewer, Plasma Phys. 10, 527 (1968).

13. S. Suckewer, Phys. Rev. 170, 239 (1968).

14. S. Suckewer, J. Phys. B. 3, 380 (1970).

15. Equipe TRF, Nucl. Fusion 15, 1053 (1975), and Euratom-CEA Association Fontenay-aux-Roses, Report EUR-CEA-FC-777, 1975.

16. TFR Group, Plasma Phys. 20, 207 (1978), and Euratom-CEA Association Fontenay-aux-Roses, Report EUR-CEA-FC-892, 1977.

17. TFR Group, Plasma Phys. 20, 735 (1978).

18. E. Hinnov, S. Suckewer, K. Bol, R. J. Hawryluk, J. Hosea, E. Meservey, Plasma Phys. 20, 723 (1978).

19. J. L. Terry, K. I. Chen, H. W. Moos, E. S. Marmar, Nucl. Fusion 18, 845 (1978), and Johns Hopkins University, Technical Report COO-2711-3, 1977.

20. M. Shiho et al., Nucl. Fusion 18, 1705 (1978).

21. F. E. Nicodemus, Am. J. Phys. 31, 368 (1963).

22. R. C. Jones, Appl. Opt. 1, 607 (1962).

23. R. A. Sawyer, Experimental Spectroscopy, 3rd ed. (Dover Publications, Inc., New York, 1963), Ch. 3.

24. W. Lochte-Holtgreven in Plasma Diagnostics, W. Lochte-Holtgreven (ed.) (North-Holland Publ. Co., Amsterdam, 1968), p. 184.

25. K. Bockasten, J. Opt. Soc. Am. 51, 943 (1961).

26. K. H. Carpenter, N. H. Lazar, ORNL/TM-6500, 1978.

27. B. R. Myers, M. A. Levine, Rev. Sci. Instrum. 49, 610 (1978).

CHAPTER FIVE

CHARACTERISTICS OF TOKAPOLE II DISCHARGES

Two reviews of tokamak physics,[1,2] a description of the evolution of a tokamak discharge,[3] and a survey of experimental tokamak results[4] are some sources which discuss the behavior of circular tokamak plasmas. Prior to the operation of Tokapole II, it was not clear how much of the circular cross section tokamak lore could be used to accurately predict the characteristics of plasmas in the magnetic divertor configuration of Tokapole II. This chapter presents experimental data obtained from Tokapole II during its first year of operation, and these data are used to characterize Tokapole II plasmas. The data have all been obtained from a standard discharge, operated at fields and pulse lengths well below the design limits of the device and presumably do not reflect the ultimate parameters achievable with Tokapole II. A number of researchers have acquired the information presented in this chapter, and their contributions are referenced as appropriate.

A. Fields and Timing

The fields and timing used for the discharges for which the data in this thesis are presented are illustrated in Fig. 5-1a. A fast piezoelectric valve (Veeco PV-10) was triggered to introduce about 3×10^{-4} Torr of H_2 gas into the machine. This gas pressure was sufficient to fill the machine with an average plasma density of 1×10^{13} cm^{-3} if there were no losses or sources of plasma. About 12.7 msec after the triggering of the puff valve, the toroidal magnetic field was triggered; it reached peak strength in about 4 msec and was then passively crow-

Fig. 5-1a: Timing of toroidal magnetic field, poloidal gap voltage V_{PG}, and preionization pulse.

Fig. 5-1b: Line-averaged electron density and plasma current as functions of time.

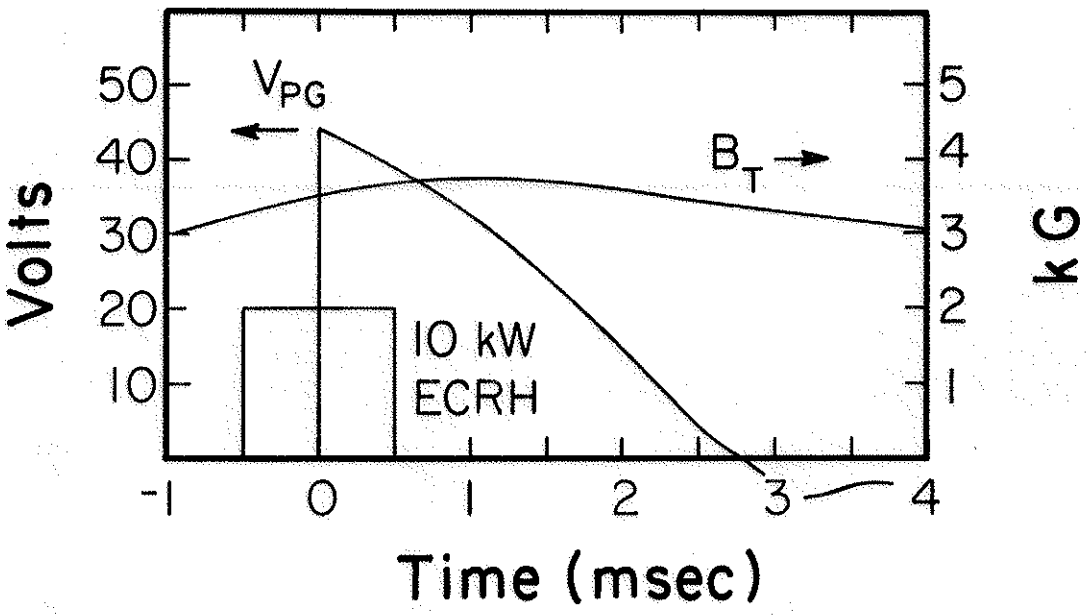
Volts
50
40
30
20
10
V_{PG}
B_T
10 kW
ECRH
5
4
3
2
1
kG
-1
0
1
2
3
4
Time (msec)

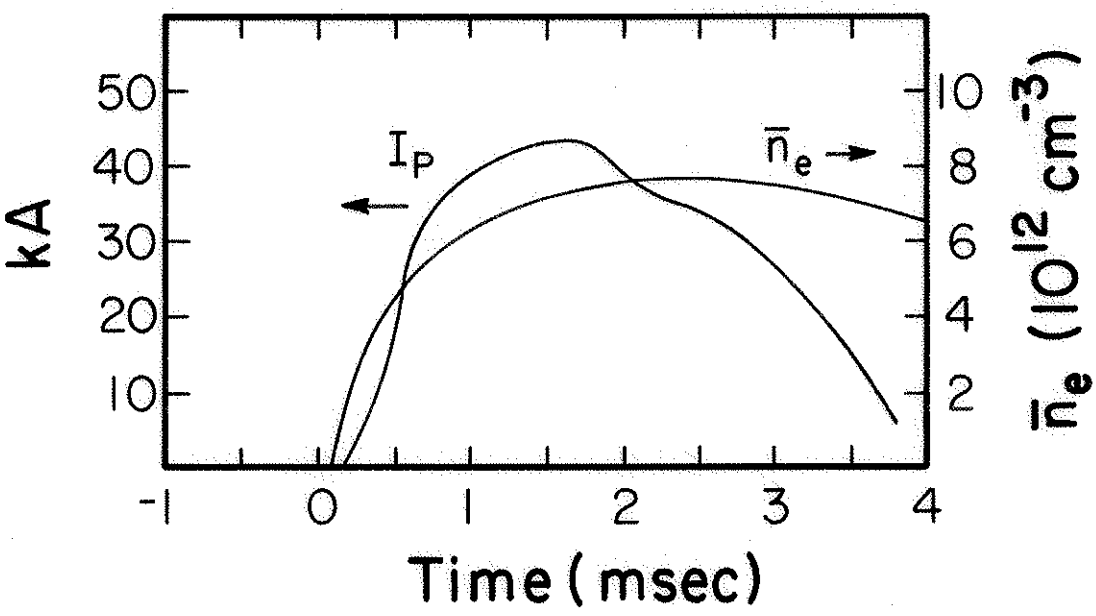
kA
50
40
30
20
10
I_P
$\bar{n}_e$
10
8
6
4
2
$\bar{n}_e$ (10^{12} cm^{-3})
-1
0
1
2
3
4
Time (msec)

barred. Shortly before the peak of the toroidal field, a 1 msec pulse of 10 kW, 8.8 GHz electron cyclotron resonance heating (ECRH) was applied to the plasma chamber to produce a plasma of about 10^{10} cm^{-3} density. This plasma was peaked on the ECRH resonance surface which was near the center of the machine for the toroidal field used. Five hundred μsec after the start of the ECRH pulse, the ohmic heating transformer was pulsed. The resulting poloidal gap voltage had a cosine waveform with an initial peak of 44 volts and a quarter period of 2.8 msec.

B. Gross Plasma Characteristics

Figure 5-1b shows the temporal development of the plasma current as measured with the current monitor. As will be shown, the plasma current was peaked near the wall for about the first msec of the discharge; since the current monitor overestimated the current flowing near the wall by a factor of less than or equal to two, the initial current (before ~ 1.5 msec) was overestimated by the monitor. Between 1.5 and 2.0 msec, the current peaked at about 40 kA. Near peak current, about half of the total current flowed inside the large Rogowski coil, when the coil was inserted into the plasma. This coil essentially measured the current flowing within the perturbed separatrix (Fig. 5-2). Insertion of a baffle plate between one of the rings and the wall (Fig. 5-2) reduced the plasma current by a factor of about two during the first one-half msec of the discharge and by a smaller factor thereafter (Fig. 5-3a). The presence of the baffle at the edge of the plasma reduced the edge current, so that the current reduction early in the discharge with the baffle inserted in the plasma was evidence of the current skin effect.

The time behavior of the line-averaged electron density through the

Fig. 5-2: Positions of divertor baffle plate (end view)
and large Rogowski coil in vacuum chamber.
Both objects are retractable from plasma region.

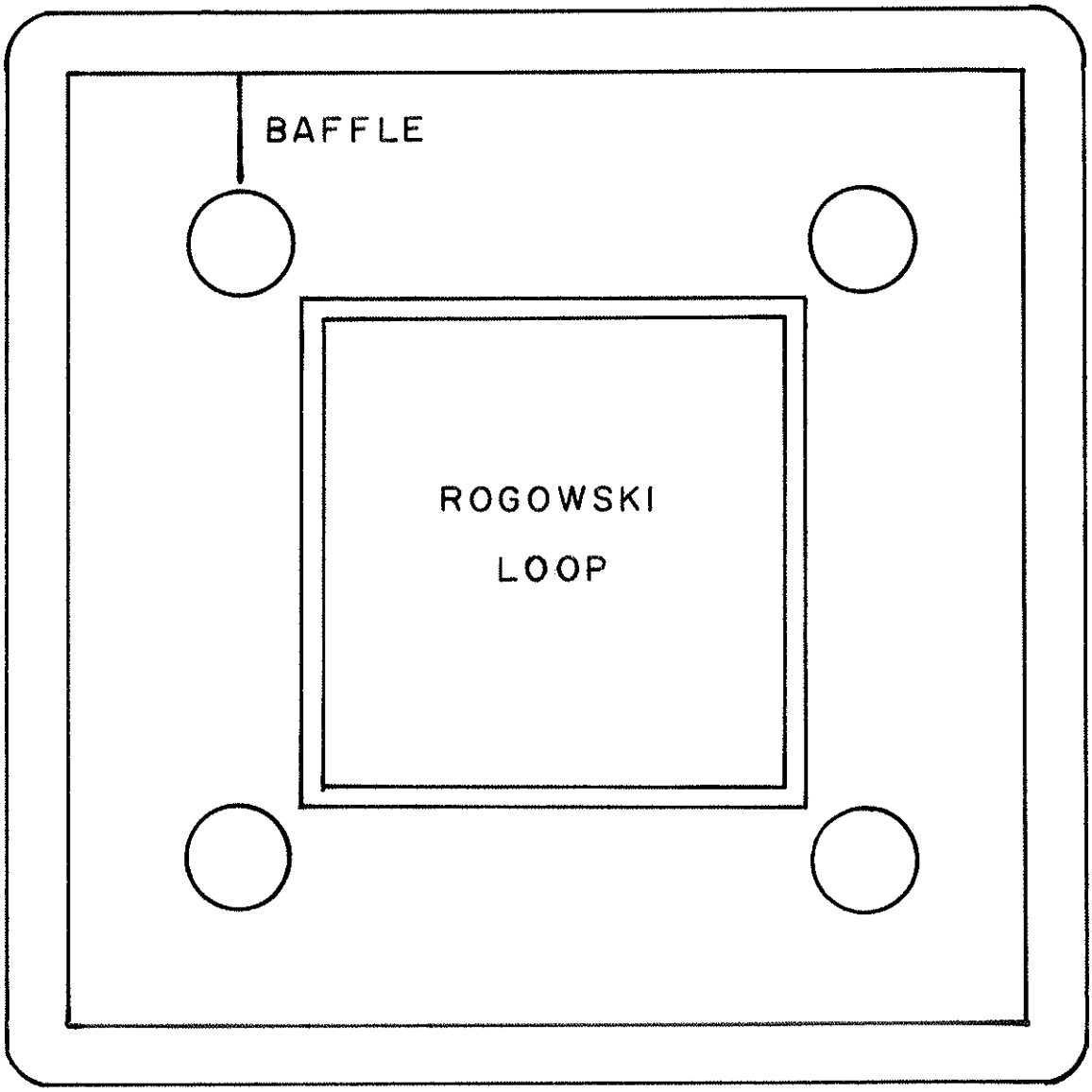
BAFFLE
ROGOWSKI
LOOP

Fig. 5-3a: Comparison of plasma currents with and without baffle plate in plasma.

Fig. 5-3b: Brightness of hydrogen L_{α} emission line.

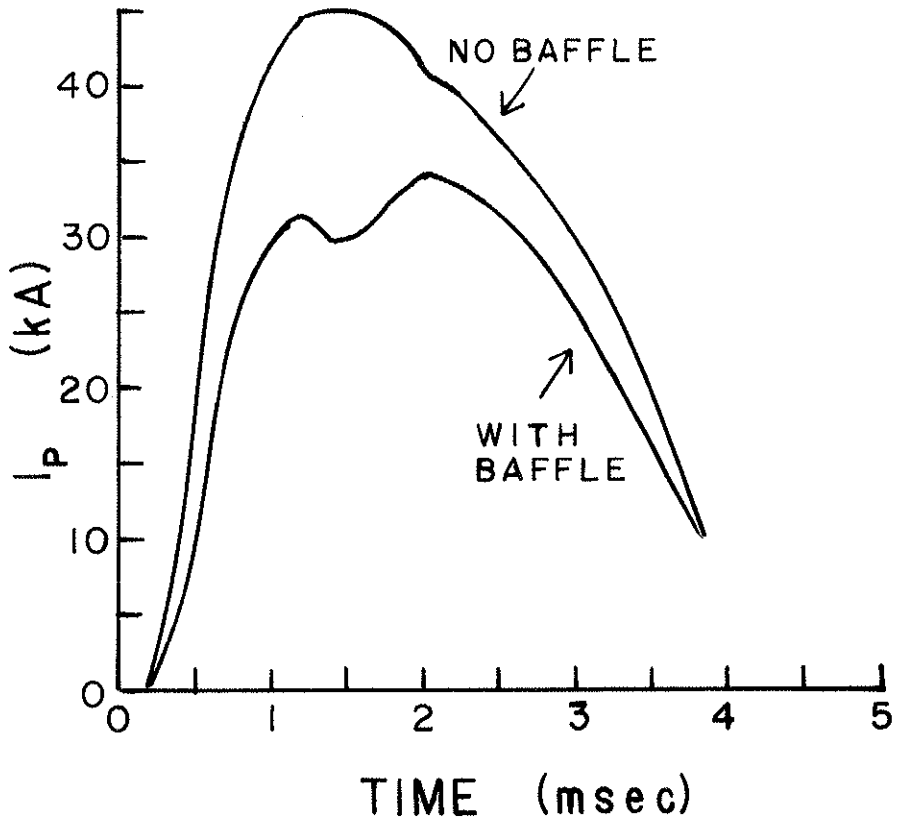
NO BAFFLE
WITH BAFFLE
I_p (kA)
0
10
20
30
40
0
1
2
3
4
5
TIME (msec)

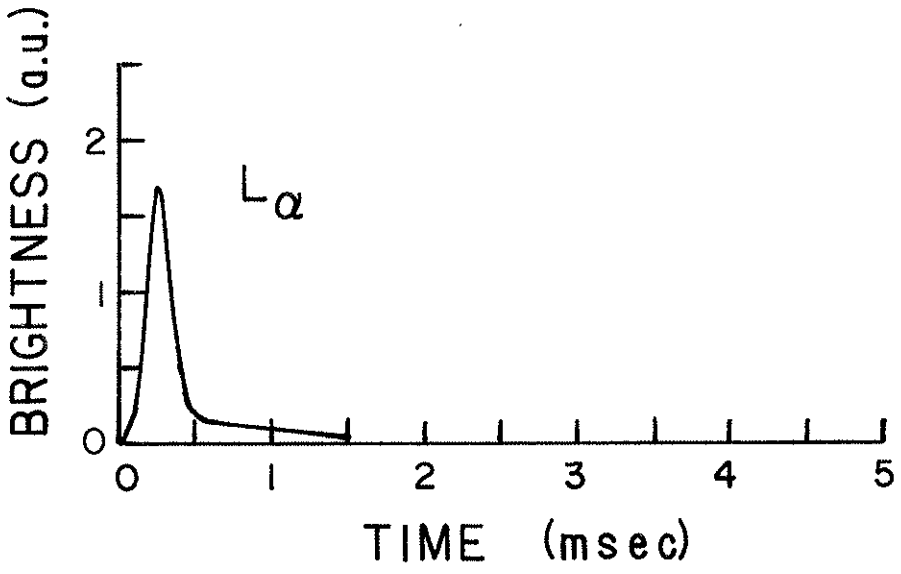
BRIGHTNESS (a.u.)
L_α
0
1
2
0
1
2
3
4
5
TIME (msec)

midcylinder, as determined from the fringes of the microwave interferometer, is illustrated in Fig. 5-1b. The relation between the interferometer fringes and the electron density is[5]:

$$N = (1/\lambda) \int_{-a}^{a} \{1 - [1 - \frac{n(x)}{n_c}]^{1/2}\} \, dx \qquad (5\text{-}1)$$

where N is the fringe number, λ is the vacuum wavelength of the microwave radiation, n(x) is the electron density profile, n_c is the electron density for cutoff ($\omega_p = \omega$), and the integration is performed over the path length of the microwave beam. In the limit that $n(x) << n_c$, the expression under the square root in Eq. 5-1 is approximately $1 - \frac{1}{2} n(x)/n_c$, and then it follows simply that the line-averaged electron density $\overline{n}_e$ is:

$$\overline{n}_e = \frac{\int_{-a}^{a} n(x)dx}{\int_{-a}^{a} dx} = \frac{\lambda}{a} n_c N \qquad (5\text{-}2)$$

where a is the plasma radius. When n(x) is comparable to n_c, the approximation breaks down and the integration must be made over the actual density profile.

Examination of ion saturation current profiles suggested that the electron density profile could be approximated by a cosine. Heald and Wharton[5] provide the results of a numerical integration of equation 1 over a cosine distribution for different values of n_c, the maximum density in the distribution. These results have been used to convert fringes into the data for Fig. 5-1b.

Due to plasma turbulence early in the discharge, the fringes before cutoff were not distinct, and it was not possible to unambiguously count them. After 4 msec, the fringes were distinct, and so the density

after that time is fairly well determined. Between 2 and 4 msec, the interferometer was cutoff, and the electron density during that time was estimated by smoothly completing the density curve in the cutoff region. Before 4 msec, the density is probably determined to an accuracy of 30-40%.

Figure 5-1b shows that the average electron density $\bar{n}_e$ reached a maximum of about 8×10^{12} cm^{-3} at about 2 msec and decreased slowly after that time. (This measurement of $\bar{n}_e$ was consistent with Langmuir probe measurements.) Figure 5-3b shows the hydrogen L_α emission line (n=2 to n=1 transition of atomic hydrogen) as a function of time. The large peak in L_α intensity at 0.25 msec corresponded to rapid ionization of the hydrogen fill gas. The hydrogen was essentially fully ionized by 0.5 msec, after which time the L_α intensity was due essentially to recycling hydrogen gas.[6] However, the electron density trace of Fig. 5-1b had reached only about 4.5×10^{12} cm^{-3} at 0.5 msec, and the electron density was still rapidly climbing at that time. Furthermore, the filling density of atomic hydrogen was about 1×10^{13} cm^{-3}, so evidently about half of the hydrogen was pumped by the wall during the hydrogen ionization phase.

Of the peak electron density, it must be assumed that roughly half of the electrons were from hydrogen and the other half were from impurities. If at 2 msec, the average central impurity ion charge was 6 (a reasonable assumption since oxygen, for example, would have become and remained O^{6+} at the center of the current channel), then Z_{eff}, as calculated from

$$Z_{eff} = \frac{\sum_i n_i Z_i^2}{\sum_i n_i Z_i} \qquad (5\text{-}3)$$

would have been 4. (In Eq. 5-3, n_i is the density of ion i, Z_i is the ion charge, and the summation is performed over all ion species present in the discharge.) This compares favorably with a spectroscopic estimate of Z_{eff} of 3 (Chapter 6).

Figure 5-4 shows the ion temperature T_i and the electron temperature T_e as functions of time. The measurements of these numbers will be described in Chapter 7. The data of Fig. 5-4 represent volume-averaged temperatures. During the first msec of the discharge T_e remained relatively constant at about 20 eV, and then T_e rose rapidly to about 100 eV. The peak electron temperature probably occurred at 1.7 - 1.8 msec (Chapter 6). Early in time, T_i was comparable to but less than T_e. As T_e increased, the ion-electron collision frequency decreased, and T_i became rather decoupled from T_e and remained at about 17 eV.

C. Spatial and Temporal Electrical Measurements

Figure 5-5 is a space-and time-resolved midplane scan of the ion saturation current, obtained with a Langmuir probe.[7] Since the ion saturation current is proportional to $n_e T_e^{1/2}$, for $T_e \gtrsim T_i$, the measurement gives a good qualitative indication of the spatial variation of n_e. Clearly, the electron density was peaked near the walls early in the discharge, while later in time, the profile was broad and peaked in the center of the machine.

A space- and time-resolved midcylinder scan of the toroidal electric field, obtained with the electric field probe,[8] is illustrated in Fig. 5-6. Except for times later than 2.5 msec, the electric field was

Fig. 5-4: Ion and electron temperatures as functions of time.

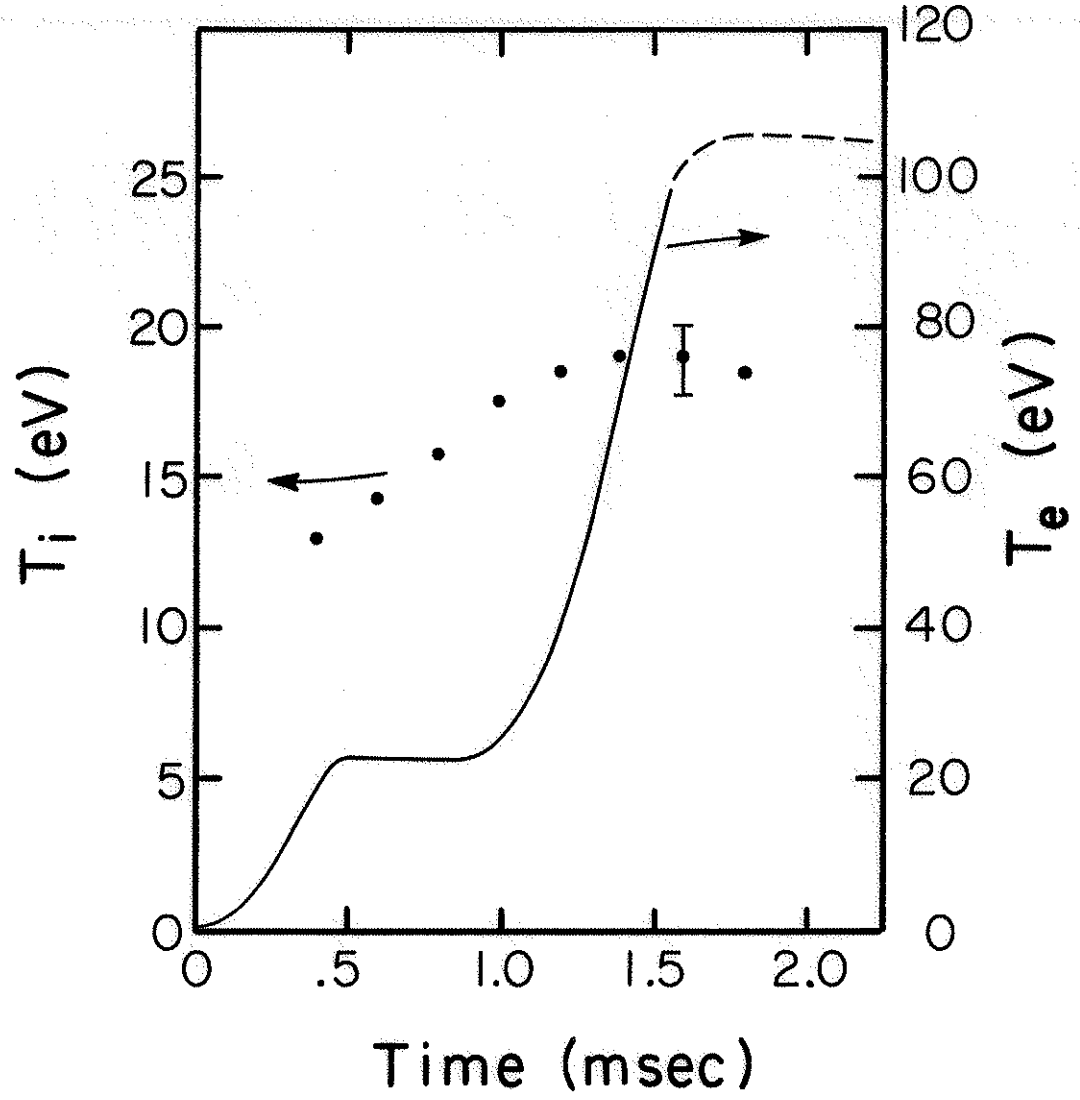
120
25
100
20
80
15
60
10
40
5
20
0
0
0
.5
1.0
1.5
2.0
T_i (eV)
T_e (eV)
Time (msec)

Fig. 5-5: Midplane scan of ion saturation current as a function of time. Minor axis located at zero cm.

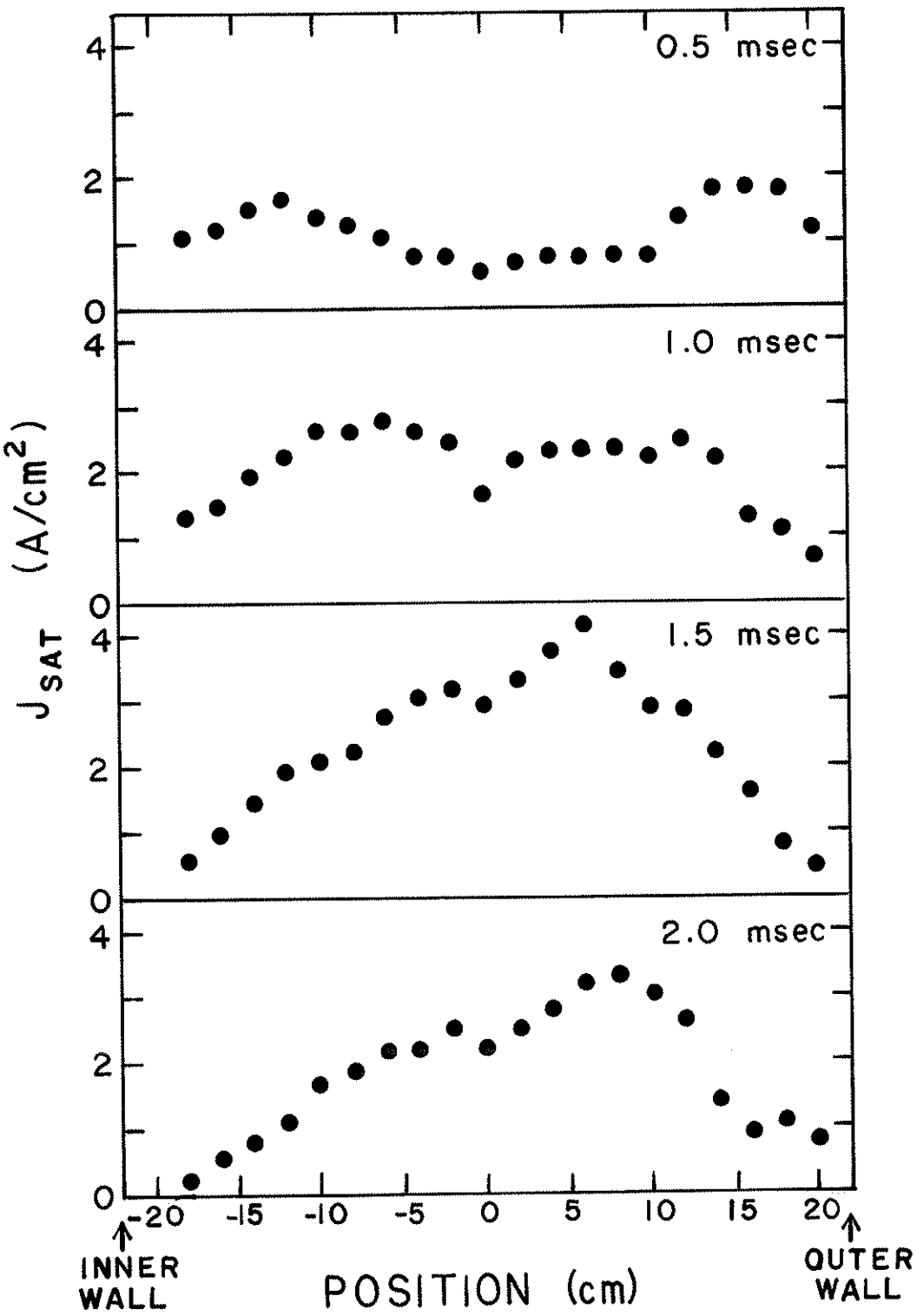
0.5 msec
1.0 msec
1.5 msec
2.0 msec
J_{SAT} (A/cm^2)
0
2
4
-20
-15
-10
-5
0
5
10
15
20
INNER WALL
OUTER WALL
POSITION (cm)

Fig. 5-6: Midcylinder scan of toroidal electric field as a function of time. Minor axis located at zero cm. Lid located at 22 cm. Time in msec indicated in upper right of each graph.

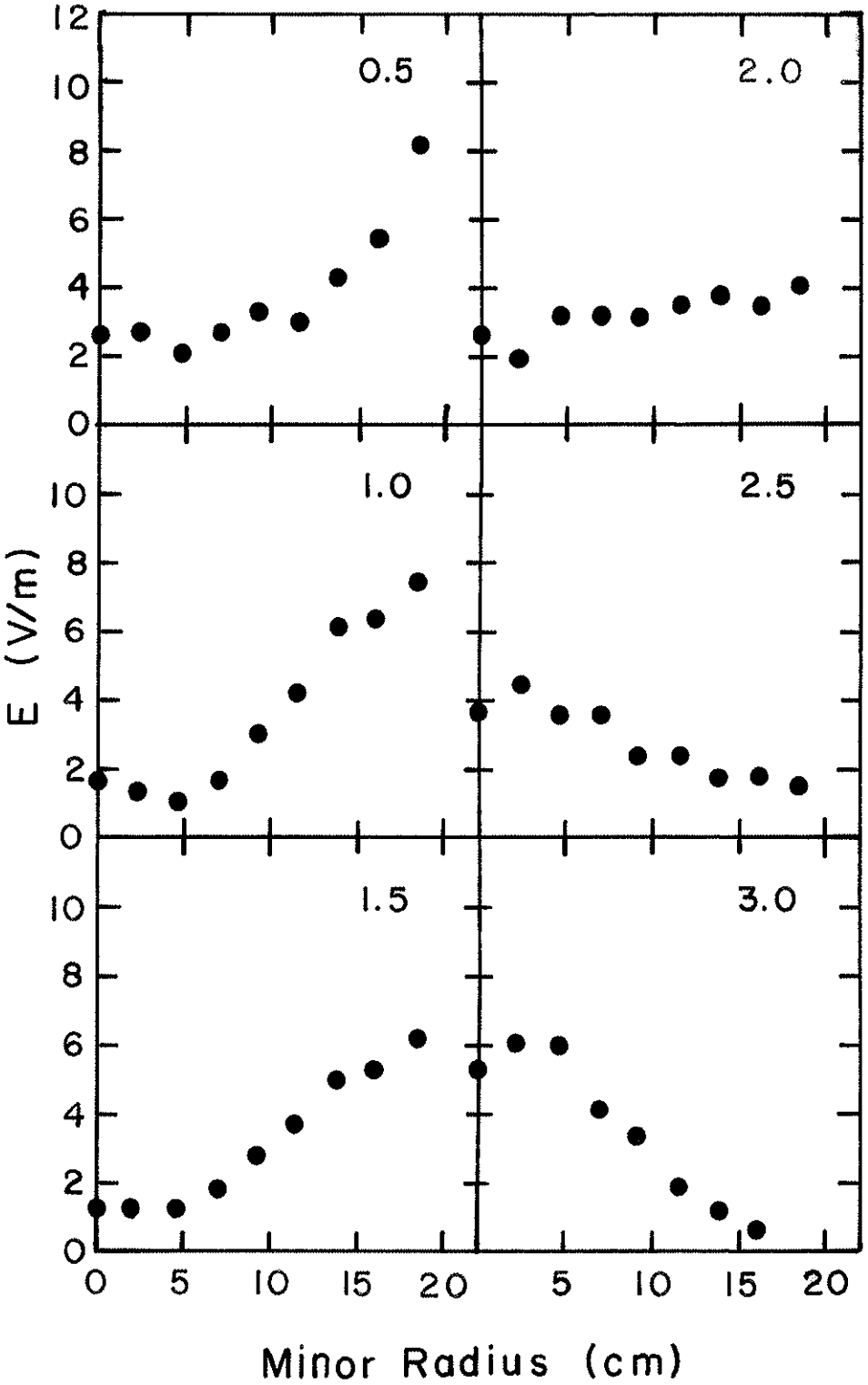
0.5
2.0
1.0
2.5
1.5
3.0
E (V/m)
Minor Radius (cm)
0
2
4
6
8
10
12
0
5
10
15
20

fairly constant in space from the minor axis to a minor radius of about 8 cm, which corresponded roughly to the position of the separatrix. From 8 cm to the wall, the electric field increased or decreased, as necessary, to reach the vacuum field level at the wall. At the plasma center, the field dropped to a minimum value of about 1V/m at 1.5 msec, which corresponded roughly to the peak of the plasma current. After that time, the central electric field increased due to the inductive electric field of the falling plasma current.

A midcylinder space- and time-resolved scan of the plasma current density, obtained with the small Rogowski coil,[8] is illustrated in Fig. 5-7. This figure clearly shows the current skin effect, the peaking of the current near the wall, early in the discharge. The current penetrated rapidly to the machine center, so that between 1.0 and 1.5 msec, the current started to peak near the machine center. The current profile was centrally peaked after that time, and the measured current density was about 50 A/cm^2 near the center of the machine.

The small Rogowski coil is known to cause significant perturbations of the current density when the probe is inside the separatrix. It is likely that the unperturbed current densities near the machine center were higher than those indicated, perhaps by as much as a factor of two. The current density in the machine center was negligible by 3.0 msec; the probe had wiped out the central current density by that time.

If it is assumed that the current density was constant in square shells centered on the machine center, then the total current can be calculated from the current density profiles. At 1.5 msec, the calculation yields 48 kA, which is consistent with the current of 43 kA, indica-

Fig. 5-7: Midcylinder scan of toroidal plasma current density as a function of time. Minor axis located at zero cm. Lid located at 22 cm. Time in msec indicated in upper right of each graph.

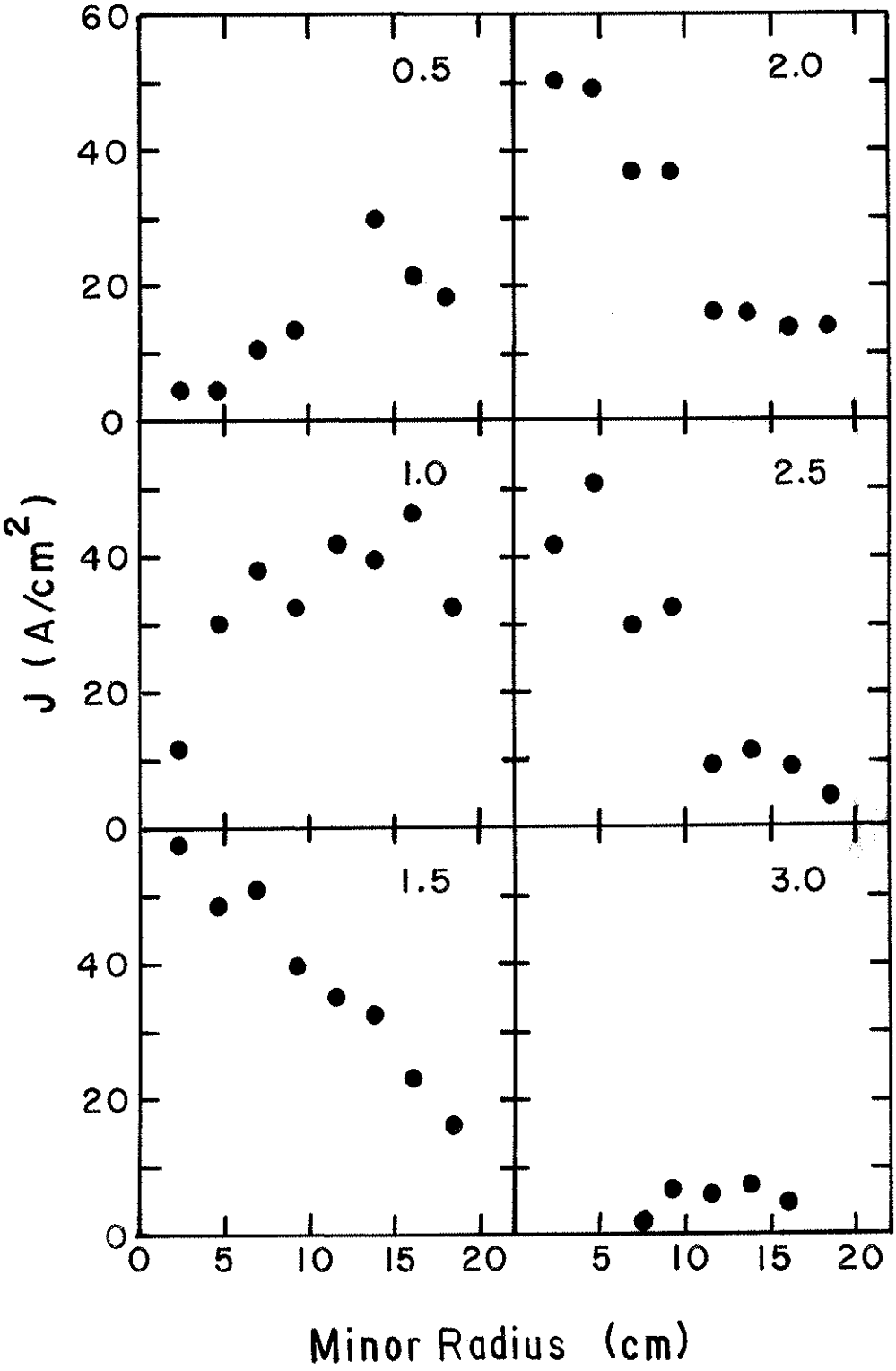
0.5
2.0
1.0
2.5
1.5
3.0
J (A/cm^2)
Minor Radius (cm)
0
20
40
60
0
5
10
15
20

ted by the current monitor.

With the assumption that the plasma resistivity obeyed the Spitzer law,[9] the electric field data and current density data of Figs. 5-6 and 5-7 can be used to calculate electron temperature spatial profiles. The assumption of Spitzer resistivity may be questionable outside the separatrix, since the plasma in that region would be influenced by the mirrors of the internal rings. That complication will be ignored. For Spitzer resistivity, the electron temperature is given by

$$T_e^{3/2} = 5.2 \times 10^{-3} Z_{eff} \ln\Lambda \ J/E_T \qquad (5\text{-}4)$$

where Z_{eff} is the effective ionic charge of the plasma, $\ln\Lambda$ is the Coulomb logarithm and is about 15 for Tokapole plasmas, J is the current density in A/cm^2, E_T is the toroidal electric field in V/cm, and T_e is in eV.

With the assumption that Z_{eff} was one (a pure hydrogenic plasma), the calculated T_e profiles are as given in Fig. 5-8. The electron temperature peaked near the wall early in the discharge. Between 1.0 and 1.5 msec, the T_e peak moved into the center of the plasma, and the temperature peaked at about 50 eV at about 1.5 msec. For most of the discharge, the central electron temperature is probably underestimated for the same reason that the current density is underestimated. If the best estimate of Z_{eff} of 3 is assumed to have been correct, then the electron temperatures should be increased by a factor of 2. Then, the central T_e would have been about 100 eV. This is consistent with the spectroscopic measurement of T_e (Fig. 5-4).

Fig. 5-8: Conductivity electron temperature along mid-cylinder as a function of time. Minor axis located at zero cm. Lid located at 22 cm. Time in msec indicated in upper right of each graph.

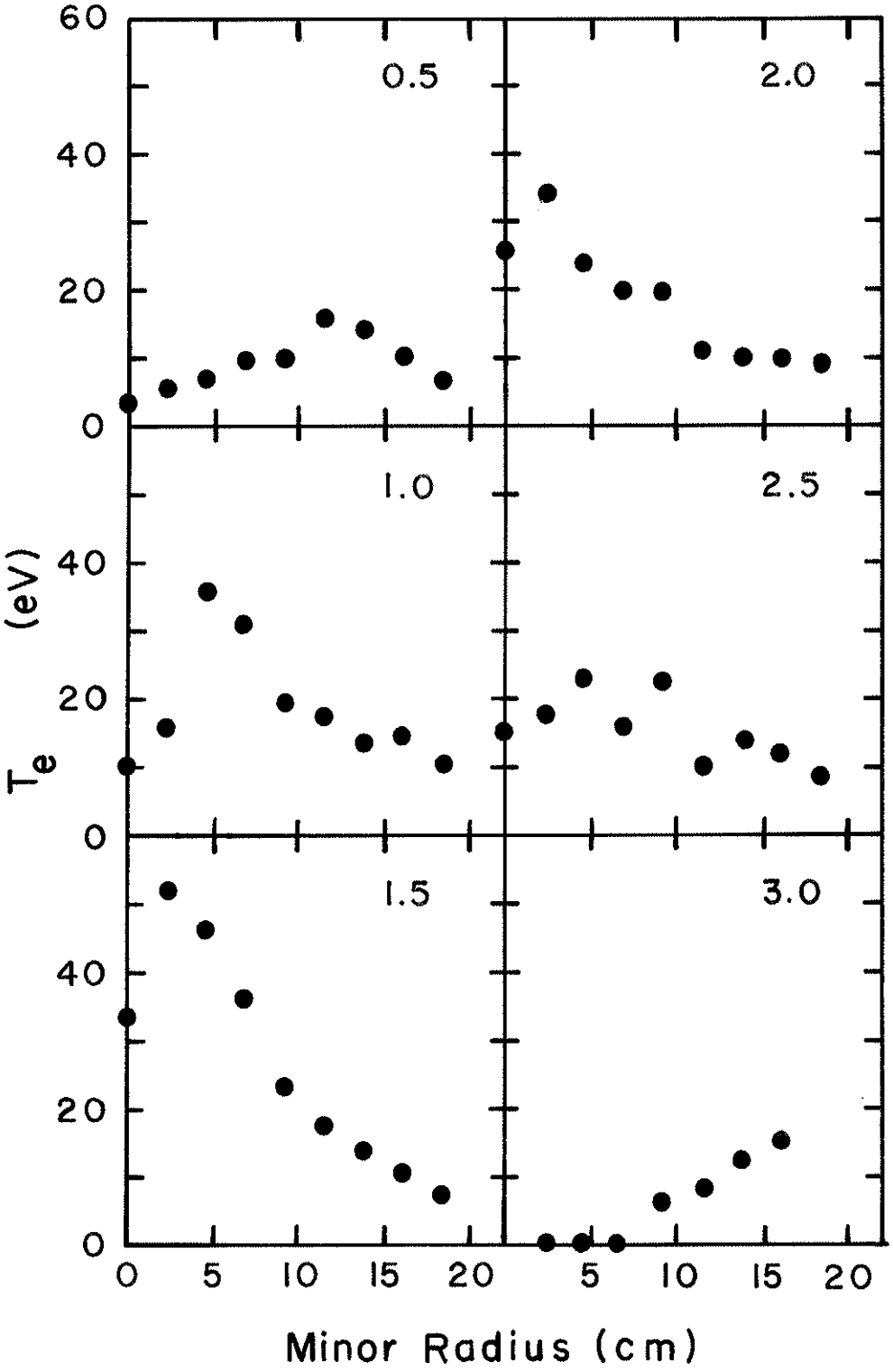
60
40
20
0
0.5
2.0
1.0
2.5
1.5
3.0
T_e (eV)
0
5
10
15
20
Minor Radius (cm)

D. Equilibrium and Stability

Theoretical calculations have shown that an equilibrium exists for a toroidal plasma current in the Tokapole II device.[10] An example of such an equilibrium is illustrated in the perturbed poloidal magnetic field flux plot of Fig. 5-9. The toroidal plasma current produces a set of nested closed flux surfaces, which are separated by two separatrices from the common flux surrounding all conductors and the private flux of the internal rings. There are four X-points, which are nulls in the poloidal magnetic field, and they occur at the points where a separatrix crosses itself. (The two separatrices are usually referred to jointly as "the separatrix.") The region outside the private flux of the plasma current will be referred to as the scrape-off region.

Experimentally-derived poloidal flux plots, obtained with a $\dot{B}$ probe, have shown that equilibria similar to that of Fig. 5-9 are produced by Tokapole plasmas.[11] Furthermore, the equilibria are stable on the time-scale of the discharge, if the rings are properly positioned. With incorrect ring positioning, the plasma moves axisymmetrically toward one of the rings.[11] To date, this axisymmetric instability has been observed only after about 2.5 msec, and it has not been a factor in the measurements described in this thesis.

There exists little, if any, theoretical analysis of the magnetohydrodynamic stability of a plasma in the Tokapole configuration. Tokapole plasmas are expected to experience the same types of instabilities as occur in circular tokamaks. However, the unique magnetic configuration of Tokapole II may enhance or suppress certain instabilities which are troublesome in standard tokamaks.

Fig. 5-9: Poloidal magnetic field flux plot with currents in the plasma and the rings. Plot calculated with an MHD equilibrium code. Dotted lines are the separatrices. Major axis is to left. The marks along the left and bottom sides indicate two cm intervals.

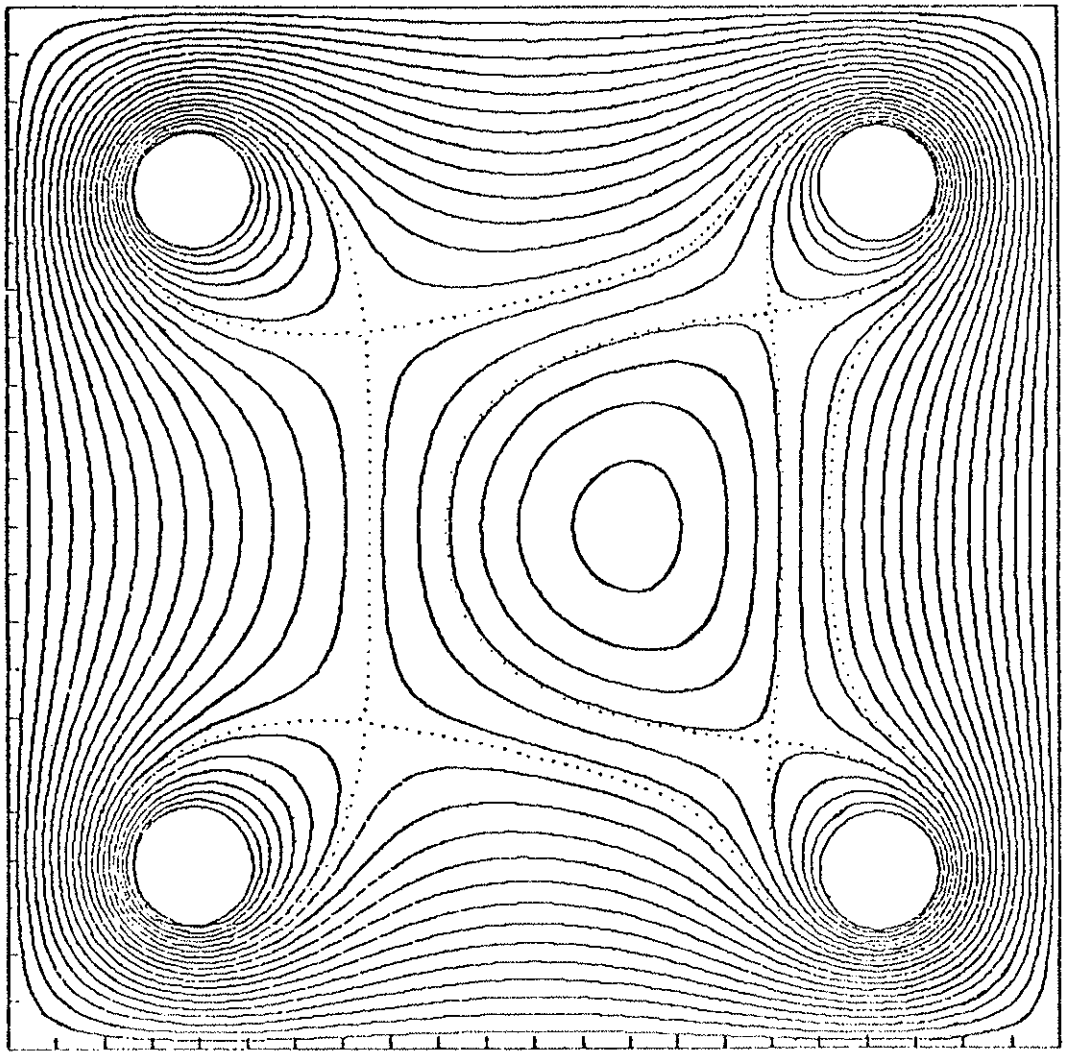

Significant MHD activity was observed with an external $\dot{B}$ coil during the current rise phase of Tokapole discharges. Figure 5-10a shows a typical $\dot{B}$ signal, and Fig. 5-10b shows the ion saturation current to the line-average probe during the same discharge. Both signals were very noisy during the early phase of the discharge. The $\dot{B}$ signal, in particular, became markedly quieter near the end of the current rise phase ($\sim$ 1.2 msec), and the decrease in MHD activity was correlated with the development of well-formed and well-centered magnetic flux surfaces.[13] Furthermore, since the plasma current was peaked near the wall during the first msec of the discharge, and since the $\dot{B}$ oscillations were correlated with the oscillations in the signal from the line average probe, which was located very close to the vacuum wall, the early MHD activity was very likely the manifestation of magnetic islands produced by the hollow current profile.[14]

The shape of the flux surfaces near the center of a Tokapole plasma is very similar to that of standard tokamaks; therefore, internal disruptions are expected to occur in the Tokapole. Internal disruptions are caused by m=1, n=1 (m and n are, respectively, the poloidal and toroidal mode numbers) tearing modes, which occur when the safety factor q drops below unity at the plasma center.[4,14] Figure 5-11 shows q profiles,[15] generated from experimentally measured flux plots, along the midplane. For the times illustrated (1.4 - 2.4 msec), the central values of q were very close to one. (The data are estimated to be accurate to about 20%.) Values of q at the magnetic axis q(0) are not available, but Fig. 5-11 suggests that q(0) dropped below one between 1.6 and 1.8 msec. After that time, the q-profile continued to become

Fig. 5-10a: Time derivative of poloidal magnetic field, outside a 4.5 inch window, as a function of time.

Fig. 5-10b: Ion saturation current to the line-average probe (in scrape-off region) as a function of time.

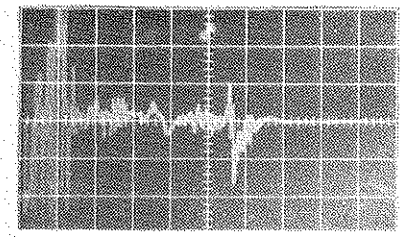

$\dot{B}_P$ TRACE

1 msec/d

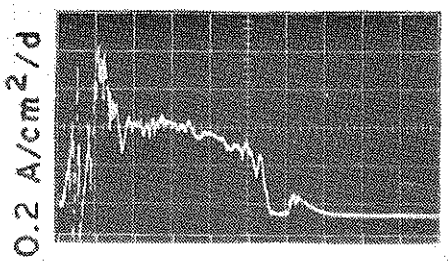

J_{SAT}

1 msec/d

Fig. 5-11: Midplane profile of safety factor as a function of time. Machine minor axis located at zero cm. Major axis lies to the left. Time in msec indicated in upper right of each graph.

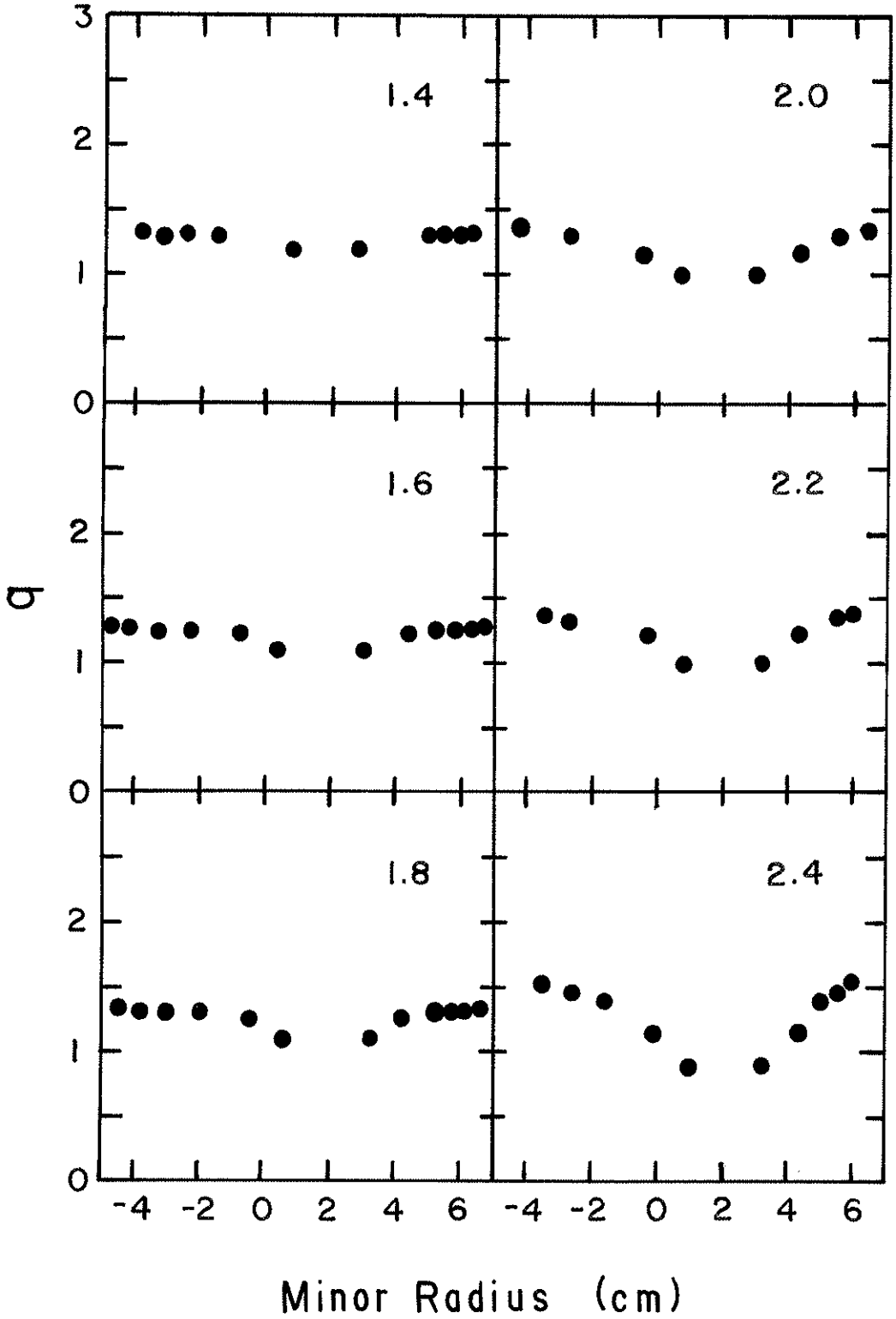
1.4
2.0
1.6
2.2
1.8
2.4
q
Minor Radius (cm)

more depressed at the plasma center. The fact that q(0) was about one suggests that internal disruptions could have occured in the plasma.

Typically, the external $\dot{B}$ coil picked up oscillations which began at about 1.7 msec. This time correlates well with the time when q(0) dropped below one, and they suggest that internal disruptions indeed did occur. Furthermore, the behavior of the soft x-ray signal was consistent with the hypothesis that disruptions started to occur at about 1.7 msec (see Chapter 6).

The value of the central current density which was needed to produce a q(0) of one can be calculated from the definition of q for circular flux surfaces:[2]

$$q(r) = \frac{r\ B_t}{R\ B_p} \quad , \tag{5-5}$$

where R and r are, respectively, the major and minor radii, and B_T and B_p are, respectively, the toroidal and poloidal fields. At the plasma center, the formula becomes

$$q(0) = 1.6\ \frac{B_T}{JR} \tag{5-6}$$

where B_T is in kG, J is the current density on axis in kA/cm^2, and R is in cm. For Tokapole discharges, R is 50 cm and B_T was 3.6 kG. A current density of 115 A/cm^2 would have produced a q(0) of one. This number is about a factor of two larger than the measured central current density; however, the current density measurement did perturb the plasma, and it is conceivable that the induced error was as large as a factor of two.

In circular tokamaks, magnetic islands may form at rational q

surfaces near the periphery of the plasma column. In particular, disturbances with poloidal mode numbers m = 2,3,4,5,... and toroidal mode number n=1 are observed at the edge of the plasma.[4] When the safety factor at the limiter q(a) drops below about three, the m=2, n=1 tearing mode is often observed to grow in amplitude, and this mode is often a precursor to the disruptive instability. Experimental observations and theory indicate that the disruptive instability may be caused by the interaction of m=2, n=1 and m=1, n=1 modes[4] or m=2, n=1 and m=3, n=2 modes.[14]

The q-profiles in the outer regions of Tokapole plasmas are very different from those in standard tokamaks, so it is not clear what types of instabilities might be expected to occur or where they might occur. Some reasonable guesses can be made, though. The data of Fig. 5-11 indicate that the q profile at the center of a Tokapole plasma is fairly flat. However, q on the separatrix is infinite since the poloidal field has zeroes on the separatrix. Therefore, the q profile must rise steeply at the edge of the central current channel and must fall fairly steeply between the separatrix and the wall. (At the wall, the magnetic field has a very large poloidal component, so q is close to one there.) Current-driven resistive tearing modes might occur near the separatrix, if the current density has a sufficiently large gradient in that region. Furthermore, the regions surrounding the four nulls in the poloidal magnetic field may also be problem regions since the confinement is poor near the nulls.

E. Discharge Evolution

With the data and observations already presented, a fairly complete picture of the evolution of a standard Tokapole discharge can be drawn.

The hydrogen fill gas is completely ionized by about 0.5 msec. However, the electron density continues to rise until about 2 msec. The source of the extra electrons is impurities, which are introduced into the discharge at a very early time.

The rapid current rise phase associated with the current penetration to the center of the machine, ends at about 1.2 msec. After that time, the current rises more slowly. During the rapid current rise, the electron density and current density profiles are hollow, the Tokapole magnetic flux plot is poorly formed, and magnetic islands are present in the skin current. Evidently, the energy confinement time is low during the current rise, as the plasma interacts strongly with the walls, and the electron temperature stays low at about 20 eV. After the current has penetrated to the center, the Tokapole flux plot is well formed, the confinement improves significantly and the electron temperature starts to rise.

The central current density and electron temperature continue to rise until about 1.7 msec, at which time some distrubance halts the rise. It is postulated that internal disruptions start to occur at 1.7 msec, as the q on axis drops below one.

From about 1 to 3 msec, the plasma current is slowly varying, and this period will be referred to as the steady state phase. During this time, the plasma is composed of a hot central current channel inside the separatrix with a relatively cool and less dense plasma between the separatrix and the walls. The separatrix forms a magnetic limiter, and the region outside of this limiter is the scrape-off region (Fig. 5-12). The electron temperature peaks at about 1.7 msec and starts to drop after that time.

Fig. 5-12: Central current channel separated from scrape-off region by separatrix.

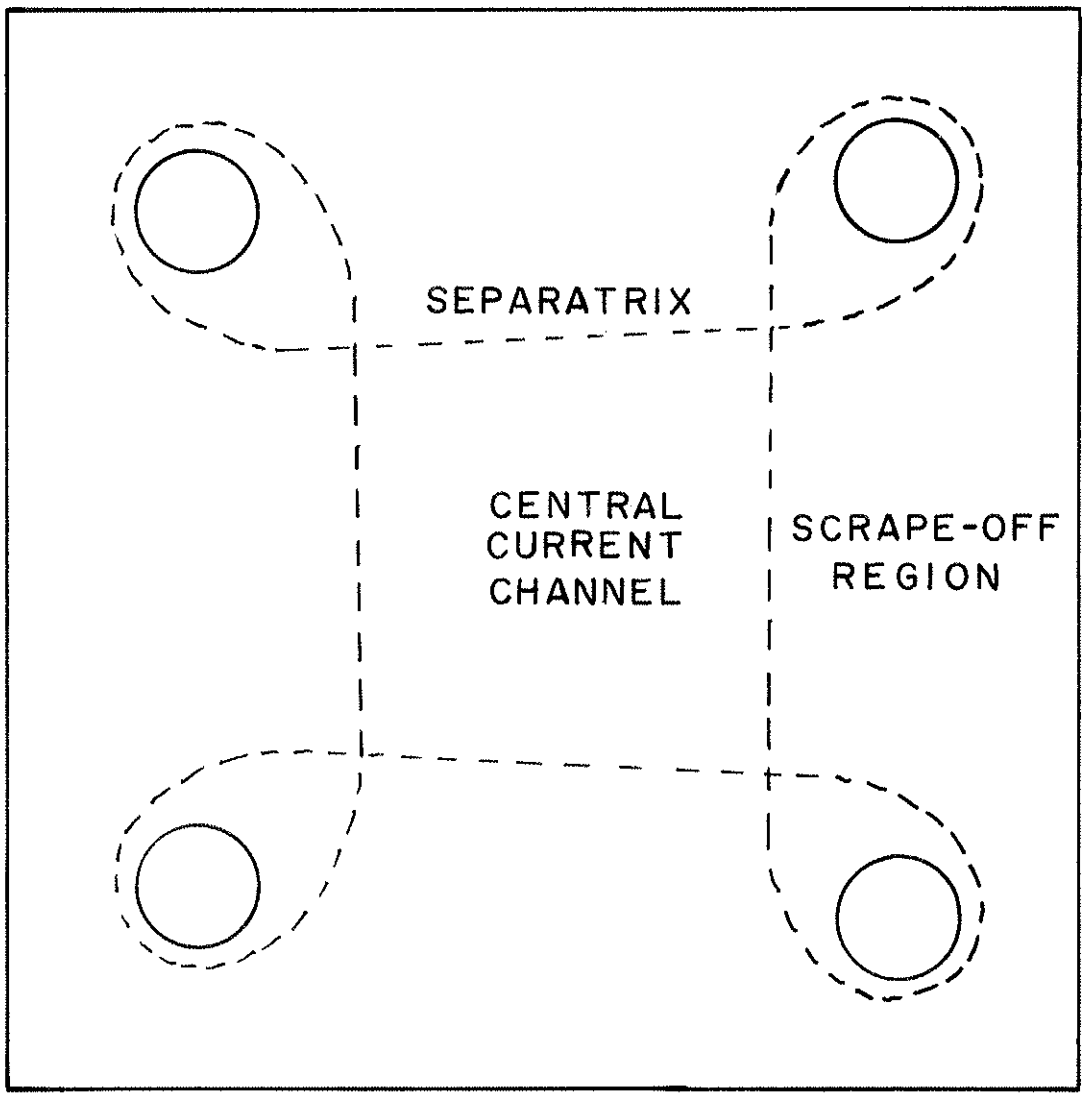
SEPARATRIX
CENTRAL
CURRENT
CHANNEL
SCRAPE-OFF
REGION

Eventually, as the poloidal gap voltage drops, the toroidal electric field drops, the ohmic input power drops, and the plasma current drops. A feedback mechanism develops because as the current decreases, the input power falls further, and the current eventually decreases to zero by about 3.5 msec. A power crowbar presently under development is expected to extend the discharge length to ~10 msec.

With the best available experimental information, it is apparent that Tokapole discharges are similar to discharges in comparable tokamaks, and one is justified in liberally applying tokamak knowledge to Tokapole plasmas.

REFERENCES

1. L. A. Artsimovich, Nucl. Fusion 12, 215 (1972).

2. H. P. Furth, Nucl. Fusion 15, 487 (1975).

3. D. L. Dimock et al., Nucl. Fusion 13, 271 (1973).

4. R. J. Bickerton, Culham Laboratory, Report CLM-R 176, 1977.

5. M. A. Heald, C. B. Wharton, Plasma Diagnostics with Microwaves (John Wiley & Sons, Inc., New York, 1965).

6. Equipe TFR, Nucl. Fusion 15, 1053 (1975), and Euratom-CEA Association Fontenay-aux-Roses, Report EUR-CEA-FC-777, 1975.

7. Measurements performed by D. Witherspoon.

8. Measurements performed by D. Shephard.

9. F. F. Chen, Introduction to Plasma Physics (Plenum Press, New York, 1974), p. 162.

10. M. W. Phillips, University of Wisconsin Plasma Studies PLP 765, 1978.

11. B. Lipschultz, S. Prager, T. Osborne, J. C. Sprott, K. Miller, M. Phillips, University of Wisconsin Plasma Studies PLP 764, 1978.

12. S. V. Mirnov, Nucl. Fusion 9, 57 (1969).

13. B. Lipschultz, private communication.

14. J. D. Callen et al., Oak Ridge Nat. Lab. Report ORNL/TM-6564, 1978 (to be published in Plasma Physics and Controlled Nuclear Fusion Research).

15. Data from M. Phillips.

CHAPTER SIX

IMPURITY OBSERVATIONS

This chapter contains the results of observations of the impurity problem in Tokapole II discharges. Impurity identification and radiated power measurements are presented for "dirty" and "clean" discharges. The results and conclusions from a series of impurity doping experiments, which were a phenomenological study of the effects of impurities in Tokapole II discharges, are discussed. The data from these studies also yield the low-Z impurity concentrations, the contributions of the low-Z impurities to the total VUV radiated power, and an estimate of Z_{eff}. Possible sources and mechanisms for impurity production are examined; in particular, it is shown that sheath potentials are important in the generation of the metal impurities. With the results presented here, an initial evaluation of the impurity problem in Tokapole II discharges is possible and will be discussed in Chapter 9.

A. Dirty Discharge

During the first weeks of machine operations, Tokapole II discharges were dominated by large impurity concentrations (predominantly carbon). Typical discharge parameters were $B_T \simeq 3$ kG, $n_e \simeq 1 \times 10^{13}$ cm^{-3}, $I_p \simeq 50$ kA, $T_e \simeq 10$ eV, discharge duration $\simeq 2$ msec. Impurity identification was facilitated with the aid of spectra obtained by photographing the CEMA output of the 1/2-m Seya survey instrument. To find reference wavelengths in the spectra, the ohmic heating voltage was reduced until only two or three bright lines were present in the spectra. These lines were members of the Lyman series of hydrogen. The Lyman lines were then

easily identifiable in more complex spectra; wavelength determination of unidentified lines was then accomplished with measurements of the distances on the photographs between identified and unidentified lines; these distances were converted into wavelengths by use of the plate factor for the photographs. Spectral lines were then identified with the aid of the literature.[1-4] In the dirty discharge, all of the bright lines were attributable to hydrogen, carbon, oxygen, or nitrogen (Table 6-1).

Radiated power measurements with the 1-m Seya indicated that about 290 kW of power were radiated (70% by carbon) while the ohmic input power was about 390 kW. These results were obtained at 1.2 msec into the discharge, which roughly corresponded to the peak in the radiated power. The power radiated by each of the important lines is tabulated in Table 6-1. Since T_e was about 10 eV, it is unlikely that significant amounts of power were radiated at wavelengths other than those tabulated. The radiated power measurements are estimated to be accurate to within a factor of two, and the input power measurements are accurate to about 50%. The data indicate that line radiation was the main energy loss mechanism for the dirty plasma.

Since the impurities were assumed to be uniformly distributed within a square plasma cross section with width 2a, the calculations of radiated power were made with Eq. 4-22, which is reproduced here:

$$P = 16 \quad \pi^2 h\nu \; B_a R \tag{6-1}$$

Because the central current channel was constrained to lie within the region bounded by the rings, the effective plasma width could not be much

TABLE 6-1.

RADIATED POWER IN DIRTY DISCHARGE

Line	P_{rad} (kW)	Line	P_{rad} (kW)
L_α 1216	9.7	N II 660	1.5
L_β 1026	1.3	N III 991	2.7
C I 1561	0.1	N III 764	15.9
C II 1335	13.5	N III 685	10.0
C II 1037	2.5	O II 718	0.9
C II 904	5.1	O II 797	0.1
C II 1010	2.4	O II/III 833	11.3
C II 858	0.5	O III 703	4.1
C II 806	0.4	O III 508	2.2
C III 977	57.0	O III 526	1.4
C III 386	2.5	O III 598	5.0
C III 1176	43.2	O IV 790	4.9
C III 1247	0.3	O IV 609	0.9
C III 538	6.1	O IV 554	6.5
C IV 1548	50.3	640	0.3
C IV 1551	25.2	972	1.6
N I 1134	0.1		
N II 1085	1.5		
N II 916	0.8		
N II 645	0.5		
N II 776	0.3		
		TOTAL	290 kW

wider than the distance between adjacent rings. With this consideration and an examination of the ion saturation current profile,[5] it was determined that 2a was about 25 cm. Photomultiplier signals were converted into brightnesses with the calibration curve for the 1-m Seya.[6]

The anode return current of the CEMA on the 1/2-m Seya is composed of electrons which are produced by all of the incident photons in the lines detected by the CEMA. Thus, the anode current is some function of the total radiated power, and as a reasonable approximation, this current has been assumed to be proportional to the VUV radiated power. When this current is passed through a resistor, the resulting voltage is called the VUV signal or integral VUV signal. This signal was calibrated in terms of radiated power by observing its value for a dirty discharge for which the radiated power was about 290 kW. The calibration factor was 350 kW/V.

B. Standard Discharge -- General Observations

After much discharge cleaning, the impurity levels dropped markedly and the discharge parameters improved significantly. This cleaner discharge, which will be referred to as the standard discharge, has been described in Chapter 5, and is the subject of the remainder of Chapter 6.

B.1. Impurity Identification

Identification of impurity lines was made with the aid of spectra from the 1/2-m survey instrument. Figure 6-1 shows a typical spectrum, and Table 6-2 is a compilation of the wavelengths and identities, when known, of the lines in Fig. 6-1. The expected lines of oxygen, nitrogen (associated with vacuum leaks), and carbon are present. Most of the lines that are not firmly identified can be attributed to oxygen, nitro-

Fig. 6-1: Vacuum ultraviolet spectrum from standard discharge.

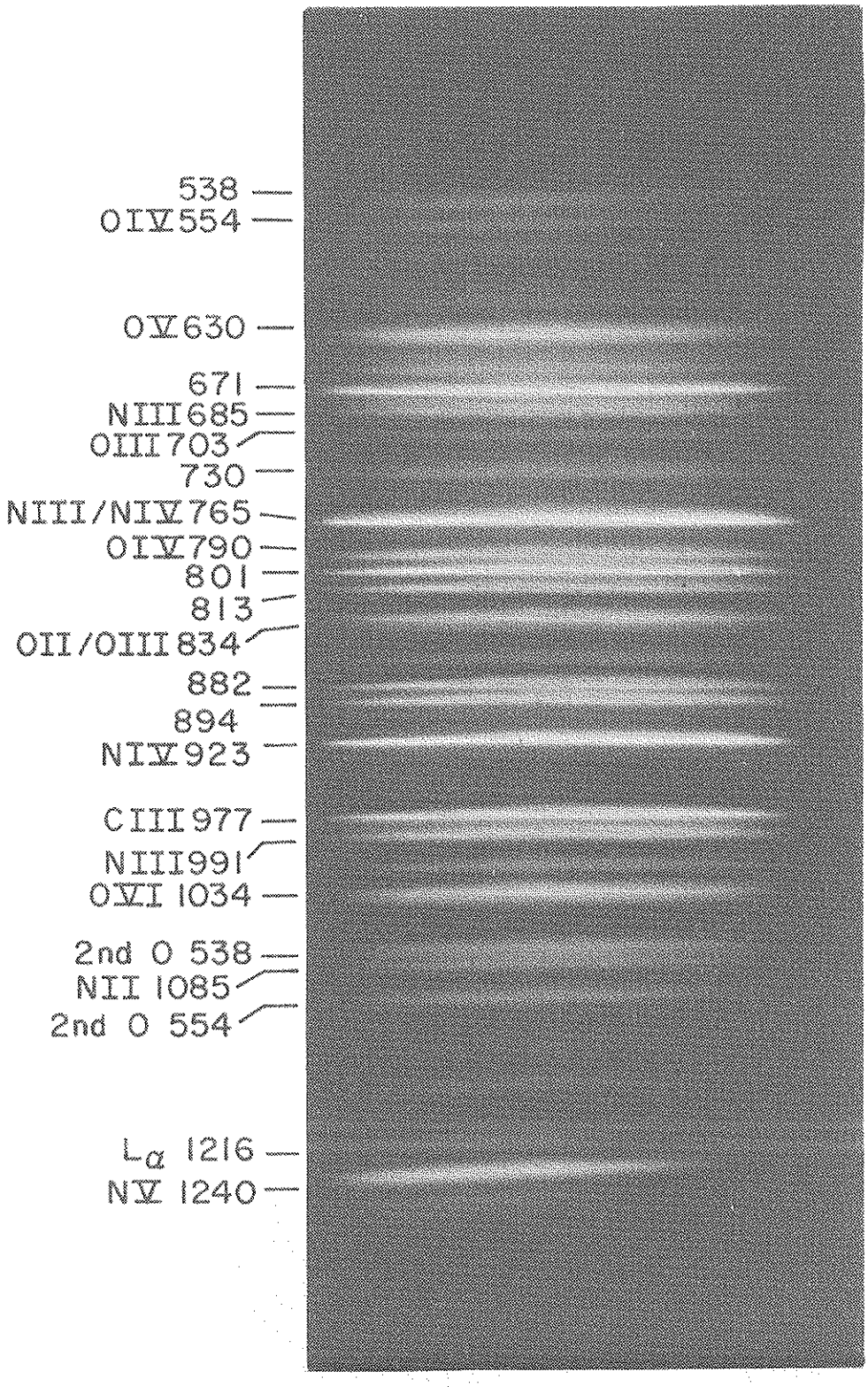

VUV SPECTRUM FROM CHANNELTRON

TABLE 6-2.

SPECTRAL LINES IN TOKAPOLE II DISCHARGES

λ(Å)	ION	INTENSITY
508	O III	vd
538	C III	b
542	Cu IV ?	b
554	O IV	b
575	Cr IV, Cu III?	d
582	O II	d
600	O III	d
608	F II,OIV ?	d
630	O V	b
635	Cr IV, N II ?	b
649	C II ?	m
658	N II,O III ?	b
671	Al III,N II, O II ?	b
678	Al III, Cu III, O V ?	m
685	N III	m
703	O III	d
730	Cu III, O V ?	d
747	N II	d
760	O V	m
765	N III/N IV	b
789	O IV	b
801	Cu III ?	b
813	Cu II, Cr III, Fe III ?	b
826	Cu II ?	m
834	O II/O III	b
841	Cu II ?	b
865	Cu II ?	m
882	Cu II or IV ?	b
894	Cu II ?	b
904	C II	d
916	N II	d
923	N IV	b
932	Cu II ?	vd
961	Cu II,N IV ?	vd
977	C III	b
991	N III	b
1015	2nd O 507	b
1032	O VI	b
1038	O VI	b
1076	2nd O 538	b
1085	N II	b
1109	2nd O 554	b
1124	Cr III ?	vd
1151	2nd O 575	vd
1162	2nd O 582	vd
1176	C III	vd
1200	N I	vd
1216	L_α	b
1239	N V	b
1243	N V	b

? = identification uncertain

2nd O = second order

b = bright

m = moderately bright

d = dim

vd = very dim

gen, carbon, or metals. Copper is the primary metallic candidate, since the rings and supports are manufactured from copper alloys, copper was eroded and distributed around the machine by the plasma, and bright copper lines have been identified in the near ultraviolet. Other metals which have been observed in the visible and near-UV are aluminum, beryllium, and chromium. Iron is also a candidate, since there was some stainless steel exposed to the plasma.

Spectra obtained from the 1/2-m Seya are known to vary over time (on the order of weeks or months). There is some evidence which suggests that low-Z and high-Z impurities are inversely related, as has been observed in other tokamaks.[7] That is, when the low-Z impurity concentration is high, metal impurities are scarce, and when the low-Z impurity concentration is low, the metallic concentration is high.

B.2. Temporal Impurity Behavior

Figure 6-2 is a sequence of pictures, obtained with the survey instrument and gated storage vidicon, which shows the temporal evolution of the impurity radiation. For each picture, the vidicon was gated on for 0.1 msec and succeeding pictures were delayed by 0.1 msec. Early in time, L_α was the only line present. Impurity lines appeared quickly, and for a given impurity element, the burnout from lower to higher ionization states with time can be readily observed.

The ionization state sequence of oxygen is illustrated in Fig. 6-3, which shows the time evolution of L_α and of resonance lines of OII-OVI, as obtained with the 1-m Seya. (The absolute calibration of the 1-m Seya is not valid for these data and the remaining data to be presented in this thesis.) Each spectral line showed a clear ionization peak, and

Fig. 6-2: Time evolution of VUV spectrum, obtained with survey instrument and gated storage vidicon.

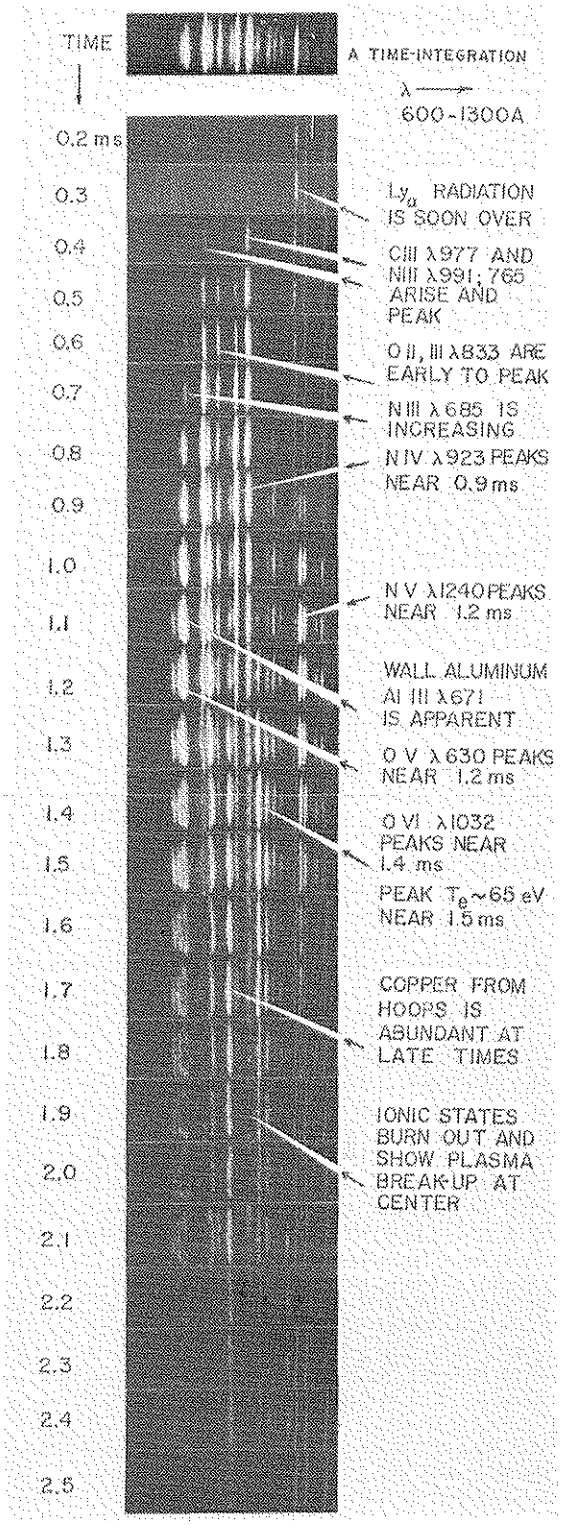
TIME
A TIME-INTEGRATION
λ
600-1300A
0.2 ms
0.3
0.4
0.5
0.6
0.7
0.8
0.9
1.0
1.1
1.2
1.3
1.4
1.5
1.6
1.7
1.8
1.9
2.0
2.1
2.2
2.3
2.4
2.5
Lyα RADIATION IS SOON OVER
CIII λ977 AND NIII λ991; 765 ARISE AND PEAK
O II, III λ833 ARE EARLY TO PEAK
N III λ685 IS INCREASING
N IV λ923 PEAKS NEAR 0.9 ms
N V λ1240 PEAKS NEAR 1.2 ms
WALL ALUMINUM AI III λ671 IS APPARENT
O V λ630 PEAKS NEAR 1.2 ms
O VI λ1032 PEAKS NEAR 1.4 ms
PEAK T_e~65 eV NEAR 1.5 ms
COPPER FROM HOOPS IS ABUNDANT AT LATE TIMES
IONIC STATES BURN OUT AND SHOW PLASMA BREAK-UP AT CENTER

Fig. 6-3: Emission line signals from L_α and OII to OVI from standard discharges. Each trace is an overlay of signals from three discharges.

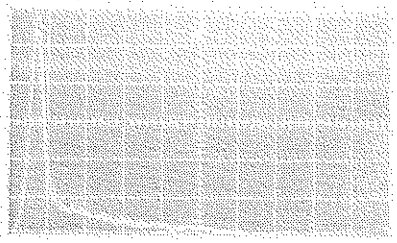

L_{α} 1216

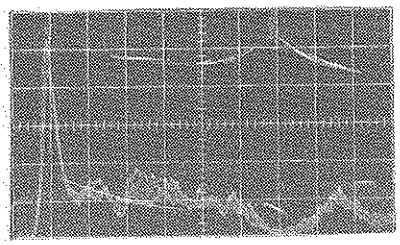

O II 718

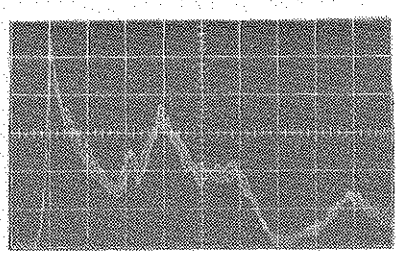

O III 703

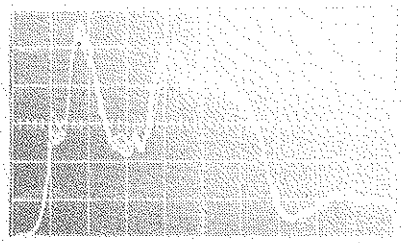

O IV 790

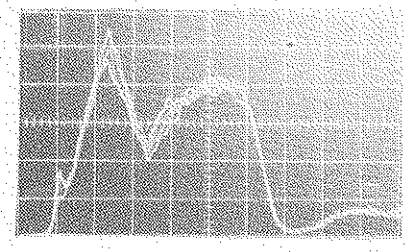

O V 630

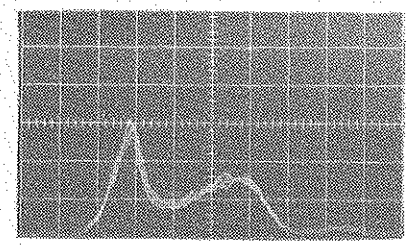

O VI 1032

ALL TIME SCALES = 0.5 ms/div

the oxygen ionization states appeared in the order of their charges. The oxygen which produced the ionization peaks is assumed to have been present early in the discharge and to have been uniformly distributed in the plasma volume.[8] After its ionization peak, the OII emission dropped to a relatively low plateau level, which was due to an influx of fresh oxygen into the plasma.[8] The emissions from OIII-OVI also decreased after their ionization peaks, but each of these emissions had a second peak which was not observed in the OII signal. Evidently, there was a local generation of oxygen at one or more places in the vacuum chamber, and oxygen from such places had burned through the OII state before it drifted into the field of view of the monochromator.

Figure 6-4 shows a typical integral VUV signal from the type of discharge used for the pictures of Fig. 6-3. This VUV signal shows qualitatively the behavior of the oxygen lines with an initial peak, which corresponds to volume ionization of impurities, and a second peak, corresponding to an impurity influx.

One of the first SXR traces available, obtained some weeks after the data of Figs. 6-3 and 6-4, is presented in Fig. 6-5. The SXR emission was characterized by a rapid rise and then an abrupt fall (cusp shape). Since the SXR detector was sensitive only to photons above 60 eV, and since at Tokapole II electron temperatures, the excitation rates to levels which can produce photons with energies greater than 60 eV are strong functions of T_e, the SXR signal was a strong function of T_e. Thus, the sudden drop in the SXR signal is evidence of an abrupt cooling of the current channel, and the cooling was probably due to an internal disruption.[9]

Fig. 6-4: Integral VUV signal from VUV survey instrument.

Fig. 6-5: Soft x-ray signal exhibiting cusp shape.

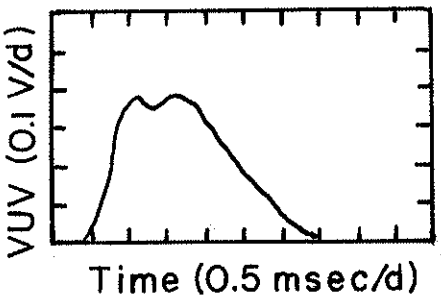

Fig. 6-4

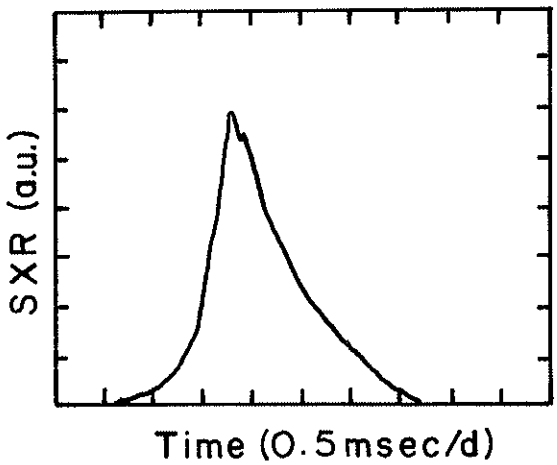

Fig. 6-5

In Fig. 6-6, pictures of the OIII-OVI traces,SXR traces, and a VUV trace from discharges in Dec., 1979 are presented to illustrate variations in good discharges. In this case, the ionization peaks of the oxygen ions were not distinguishable from the noisy plateau signals. The noise in the oxygen signals is a sign of plasma turbulence, which may have been due to MHD instabilities. The VUV signal had a low value, and it did not show any definite sign of an ionization peak either.

SXR signals from similar discharges are illustrated in Fig. 6-6. One of the signals shows the abrupt drop which was observed in Fig. 6-5. During the Dec. runs, the SXR signal usually showed the cusp behavior early in a run, but later in the run the SXR peak would be rounded as is also illustrated in Fig. 6-6. The rounding of the SXR signal was correlated with clean-up of the machine on a given run day. However, in all cases, the SXR peak occured at about 1.7 msec, and it was evidently correlated with the onset of MHD activity as indicated by the external magnetic coil. A compelling interpretation of the observations is that the central current density increased until a q=1 surface was produced inside the current channel. Internal disruptions at that surface then limited or decreased T_e.

B.3. Radiated Power

Line radiated power from standard discharges, as measured with the VUV detector, was 35-70 kW. The radiation power loss was about 10-20% of the ohmic input power, which was about 350 kW; therefore, line radiation accounted for only a small portion of the power loss.

The VUV detector was not sensitive to photons with energies greater

Fig. 6-6: Brightnesses of emission lines of OIII to OVI. Bottom right picture: top trace is VUV signal and bottom trace is SXR signal showing cusp behavior. Bottom left picture shows SXR trace in which peak signal is rounded. The OIII-OV traces and bottom left SXR trace are each overlays from two shots.

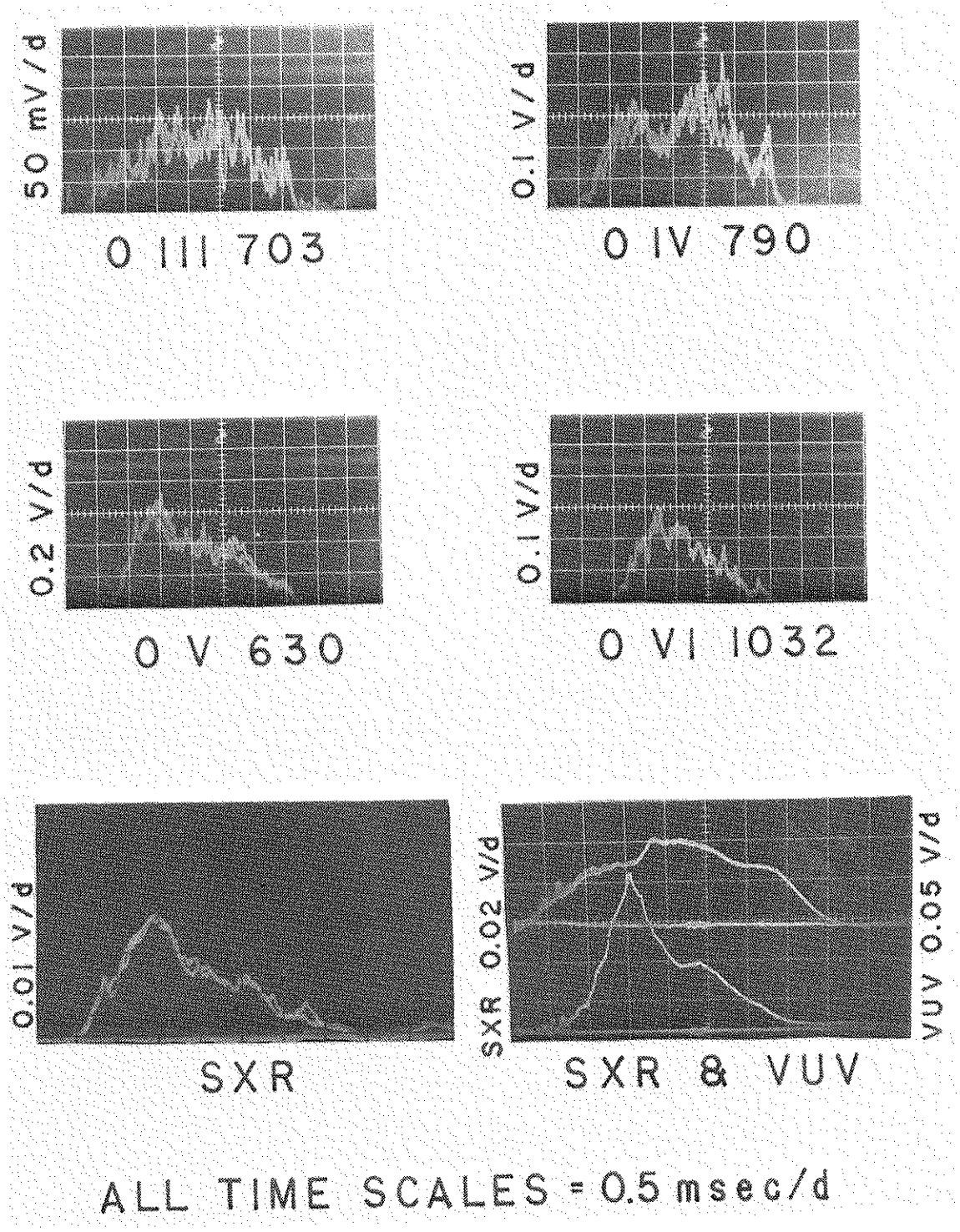
50 mV/d
O III 703
0.1 V/d
O IV 790
0.2 V/d
O V 630
0.1 V/d
O VI 1032
0.01 V/d
SXR
SXR 0.02 V/d
VUV 0.05 V/d
SXR & VUV
ALL TIME SCALES = 0.5 msec/d

than about 30 eV (400 Å), and it is likely that this detector did not measure all of the radiated power. To study this problem, the broad-band VUV filters, described in Chapter 3, section D, were used with a channeltron detector to compare the numbers of photons radiated in different wavelength regions. The results were that the power radiated outside the range of detectability of the 1/2-m Seya was negligible. Furthermore, during doping experiments the VUV signal has been increased by a factor of about 4 while the ohmic input power has increased by no more than 30%. This is consistent with the previous observations that the radiated power was no more than about 20% of the ohmic input power.

C. Phenomenological Impurity Study

To further characterize the effects of impurities on plasma behavior, a study was performed in which controlled amounts of impurities were added to the plasma and the corresponding variations of several plasma quantities were monitored.[10] A second puff valve was used to introduce O_2, N_2, or CH_4 into the vacuum chamber several milliseconds before the plasma was produced. Impurity densities were measured with the fast ion gauge. Parameters observed as functions of dopant density were the intensities of one or more lines of the injected impurity, the VUV signal, the SXR signal, and the integral of the plasma current over time (Amp-Seconds or AS). As a matter of experimental convenience, the peak values of the light signals were recorded, since at small doping levels, the peaks characterized quite well the behavior of the entire traces. In particular, the SXR and VUV traces maintained their shapes in time and scaled in size at small dopant densities. The intensity of the ionization peak of a spectral line was the most convenient parameter to charac-

terize the response of line radiation to doping. Results from the three dopants were similar. Oxygen, the most abundant low-Z impurity, was studied in the most detail.

C.1. Impurity Concentrations

The doping technique provided a convenient method to measure low-Z impurity concentrations early in the discharge. The results were that the oxygen concentration was typically 3-5% of the electron density, the carbon contamination was about 0.5%, and nitrogen was a 2-5% impurity when a leak resulting in a base pressure of 1-2 x 10^{-7} torr was present.

Determination of the oxygen concentration by the doping technique is illustrated in Fig. 6-7, which is a plot of the intensities of convenient lines of OIII-OVI as functions of the doping concentration of O_2. With the possible exception of the OV data, the data for all spectral lines extrapolate to a common point on the horizontal axis. This point corresponds to 1.6 x 10^{11} cm^{-3} of O_2 (3.2 x 10^{11} cm^{-3} of atomic oxygen) and is interpreted as the amount of oxygen which was present in the plasma with no doping. Since it is likely that some of the gas present in the machine during discharge formation was pumped by the walls, it is probably more accurate to express the oxygen contamination as a percentage of the H_2 filling density (5 x 10^{12} cm^{-3}). In this example, the oxygen concentration was 3% of the electron concentration. The probable error of this technique is estimated to be no more than 25%.

At the higher doping levels, the rate of increase of the OVI density with the dopant level decreased while the intensities of the lines of OIII-OV increased faster than linearly with the dopant concentration. These effects may have been caused by changes in the spatial profiles of

Fig. 6-7: Brightnesses of ionization peaks of OIII-OVI as functions of O_2 dopant concentration. Lines are least squares fits to the data.

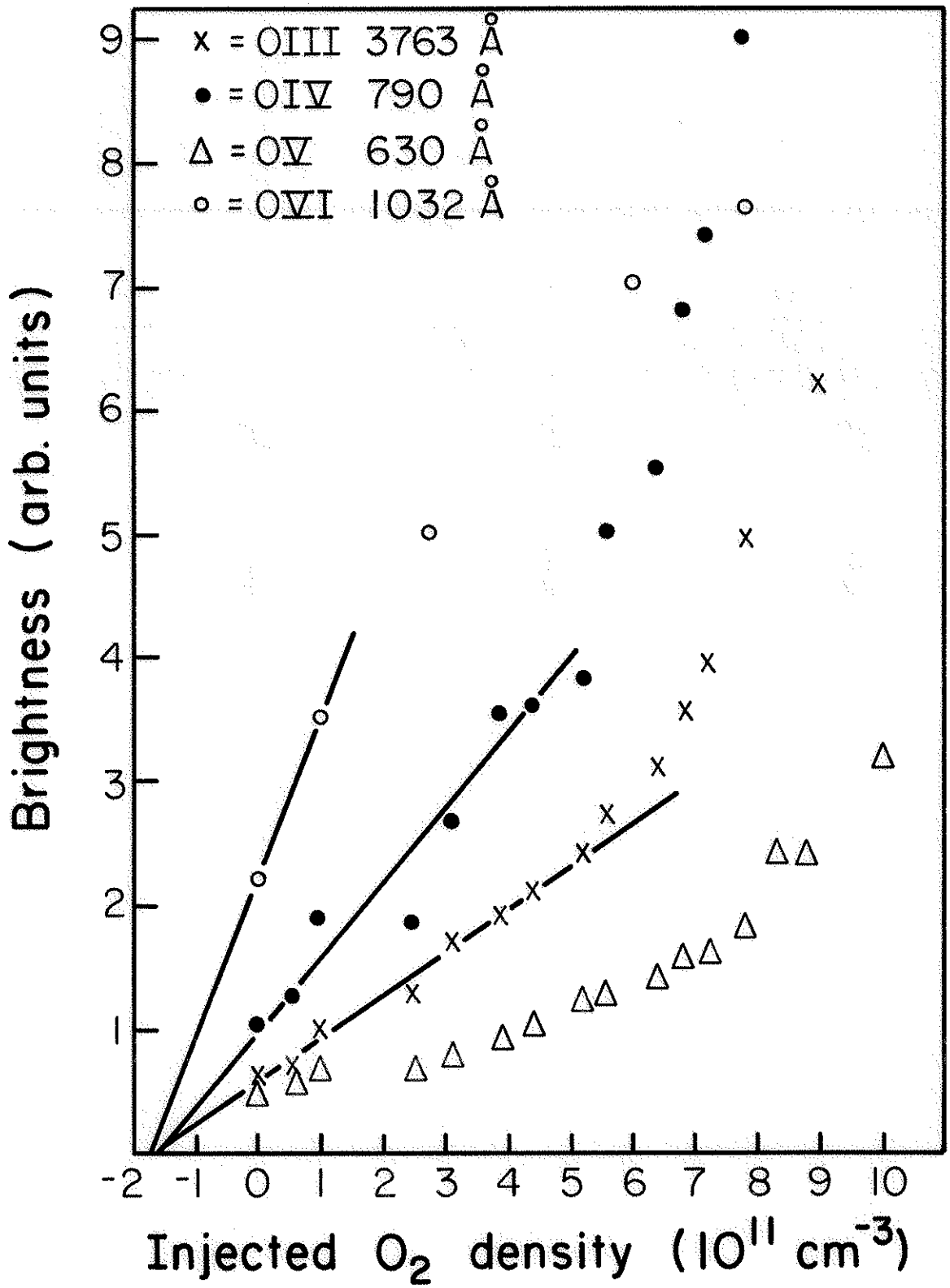
x = OIII 3763 Å
• = OIV 790 Å
Δ = OV 630 Å
o = OVI 1032 Å
Brightness (arb. units)
Injected O_2 density (10^{11} cm^{-3})
-2 -1 0 1 2 3 4 5 6 7 8 9 10
1 2 3 4 5 6 7 8 9

the impurities or in the T_e profile. Part of the explanation is probably that at the higher doping densities, T_e was reduced so that the production rate of OVI decreased. Then, a greater percentage of the oxygen was in the form of OIII-OV.

Figures 6-8 and 6-9 show, respectively, the variation of CIV 1549 as a function of the CH_4 dopant level and the variation of NIV 765 as a function of the N_2 dopant level. In the cases illustrated, the residual concentration of C was about 5×10^{10} cm^{-3} and of N, about 5×10^{11} cm^{-3}.

C.2. Impurity Contributions to Radiated Power

By a technique similar to that described above, the contributions of the low-Z impurities to the integral VUV signal (or, equivalently, the radiated power) were estimated. In Fig. 6-10, which is a plot of the OIV 790 intensity against the VUV signal during an oxygen doping run, an extrapolation of the data to the horizontal axis indicates that about 25% of the VUV signal was due to oxygen. Similar plots of the CIV 1549 line and the NIV 765 line in Figs. 6-11 and 6-12 show that 5% of the VUV was due to carbon radiation and about 26% was due to nitrogen.

The data typically indicated that 25-35% of the VUV signal was produced by oxygen, about 5% was due to carbon, and about 20-30% was due to nitrogen. (The machine had a persistent vacuum leak at the time that these data were obtained.) About 40% of the VUV signal was therefore not accounted for, and this portion was presumably due to metals. These numbers are probably accurate to about 25%.

Fig. 6-8: Brightness of C IV 1549 ionization peak as a function of CH_4 dopant concentration. Line is a least squares fit to data.

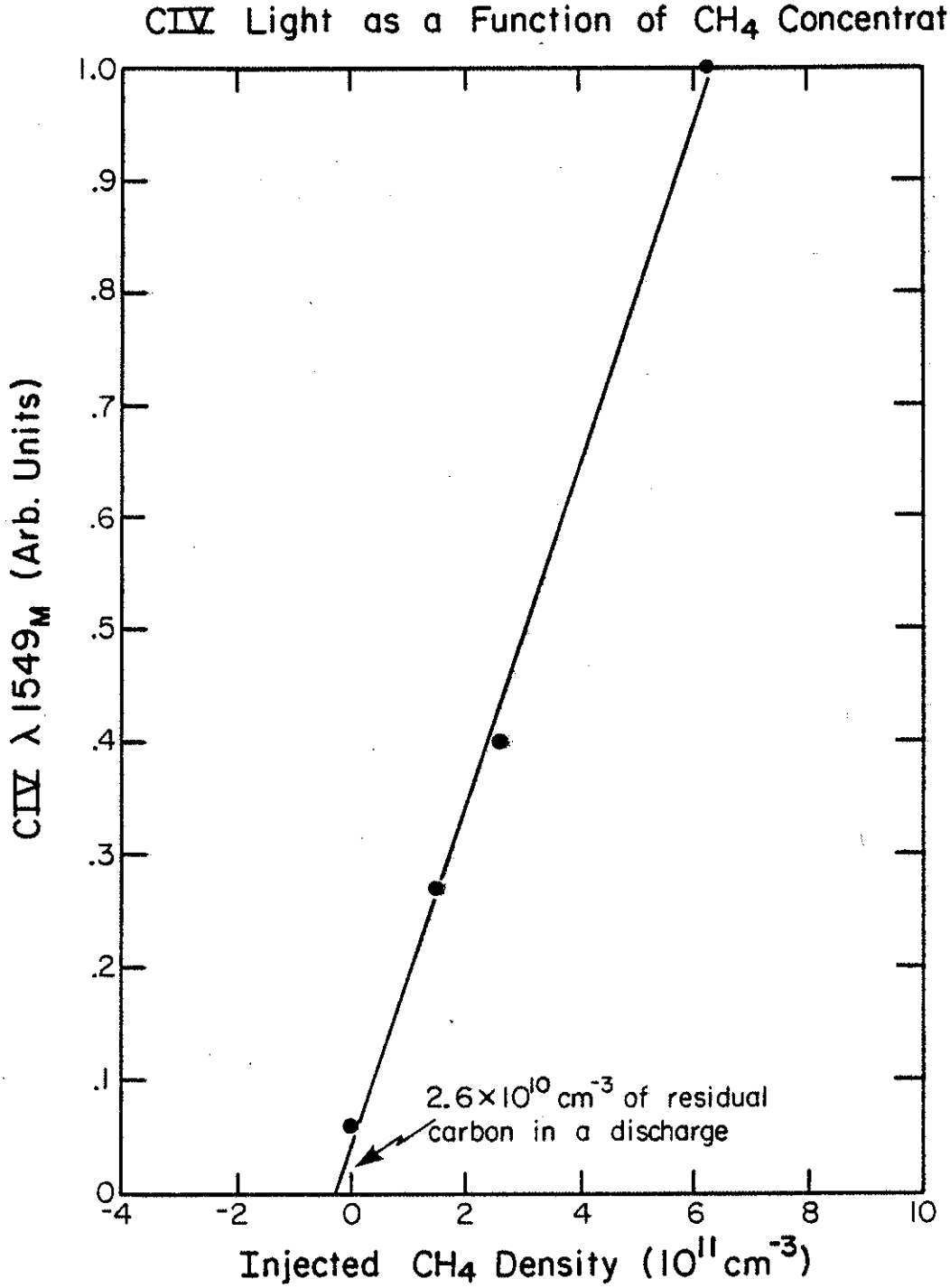
CIV Light as a Function of CH_4 Concentration
CIV $\lambda 1549_M$ (Arb. Units)
1.0
.9
.8
.7
.6
.5
.4
.3
.2
.1
0
-4
-2
0
2
4
6
8
10
Injected CH_4 Density (10^{11} cm^{-3})
2.6×10^{10} cm^{-3} of residual carbon in a discharge

Fig. 6-9: Brightness of N IV 765 ionization peak as a function of N_2 dopant concentration. Line is a least squares fit to data.

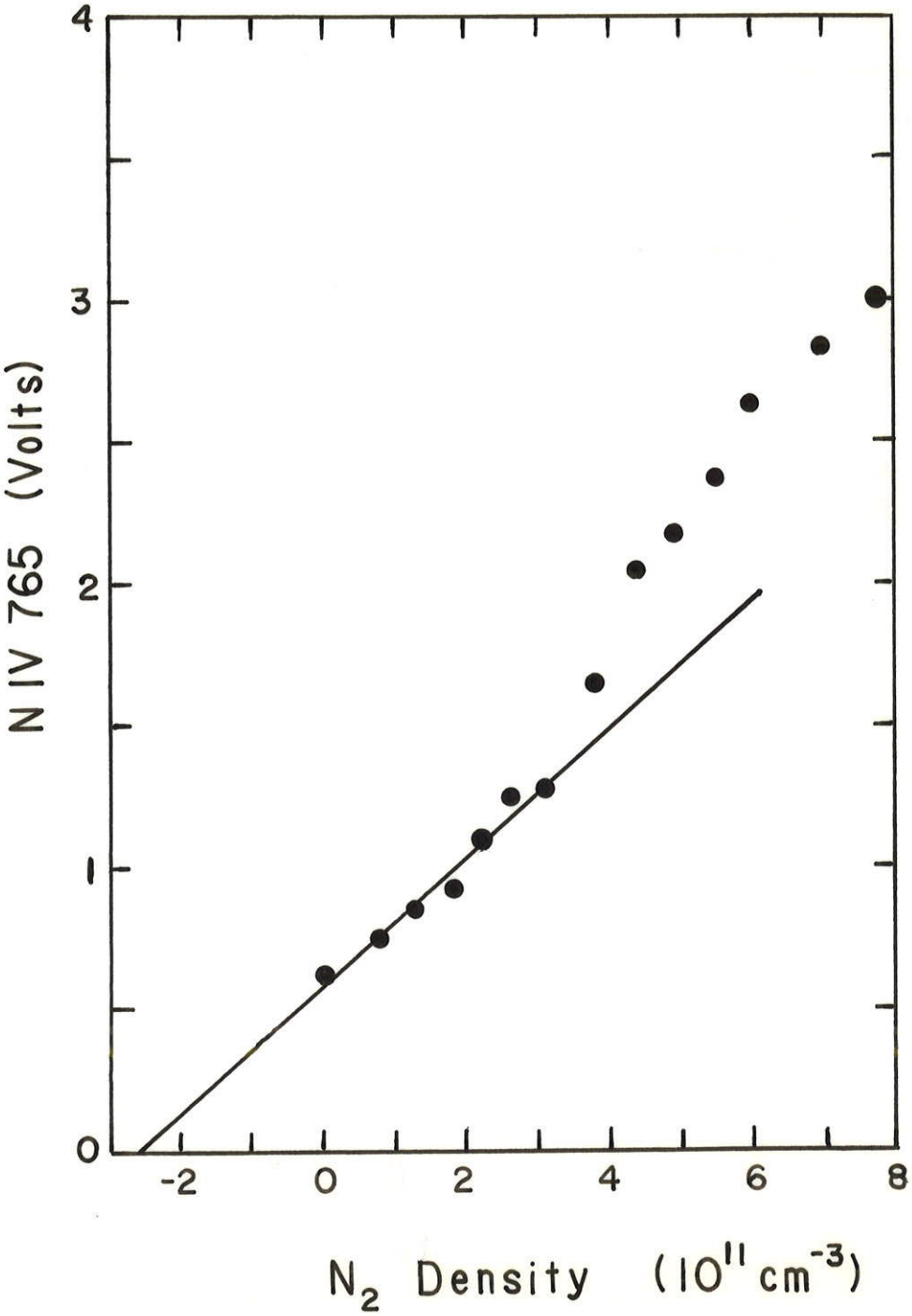
4
3
2
1
0
N IV 765 (Volts)
-2
0
2
4
6
8
N2 Density (10^11 cm^-3)

Fig. 6-10: Brightness of OIV 790 ionization peak vs the maximum VUV signal during O_2 doping run. With no doping, VUV_M signal was 0.10 volt. The line through the data points extrapolates to 0.075 volt with no OIV light (no oxygen impurity). Thus, in the no doping case, oxygen accounted for $\frac{0.10-0.075}{0.10}$ = 25% of the VUV_M signal.

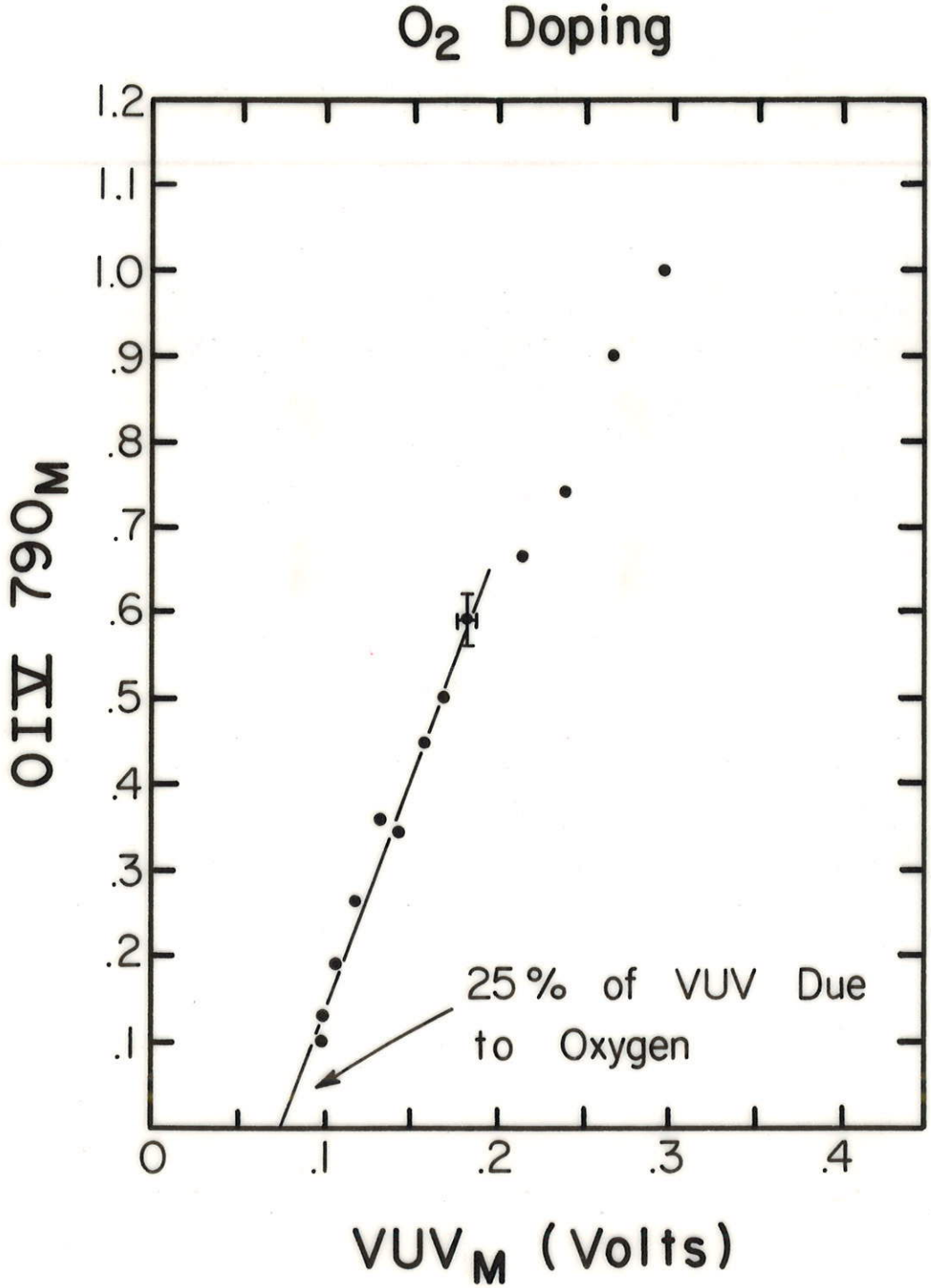
O_2 Doping
OIV 790$_M$
1.2
1.1
1.0
.9
.8
.7
.6
.5
.4
.3
.2
.1
0
.1
.2
.3
.4
25% of VUV Due
to Oxygen
VUV$_M$ (Volts)

Fig. 6-11: Brightness of C IV 1549 ionization peak vs. the maximum VUV signal during CH_4 doping run.

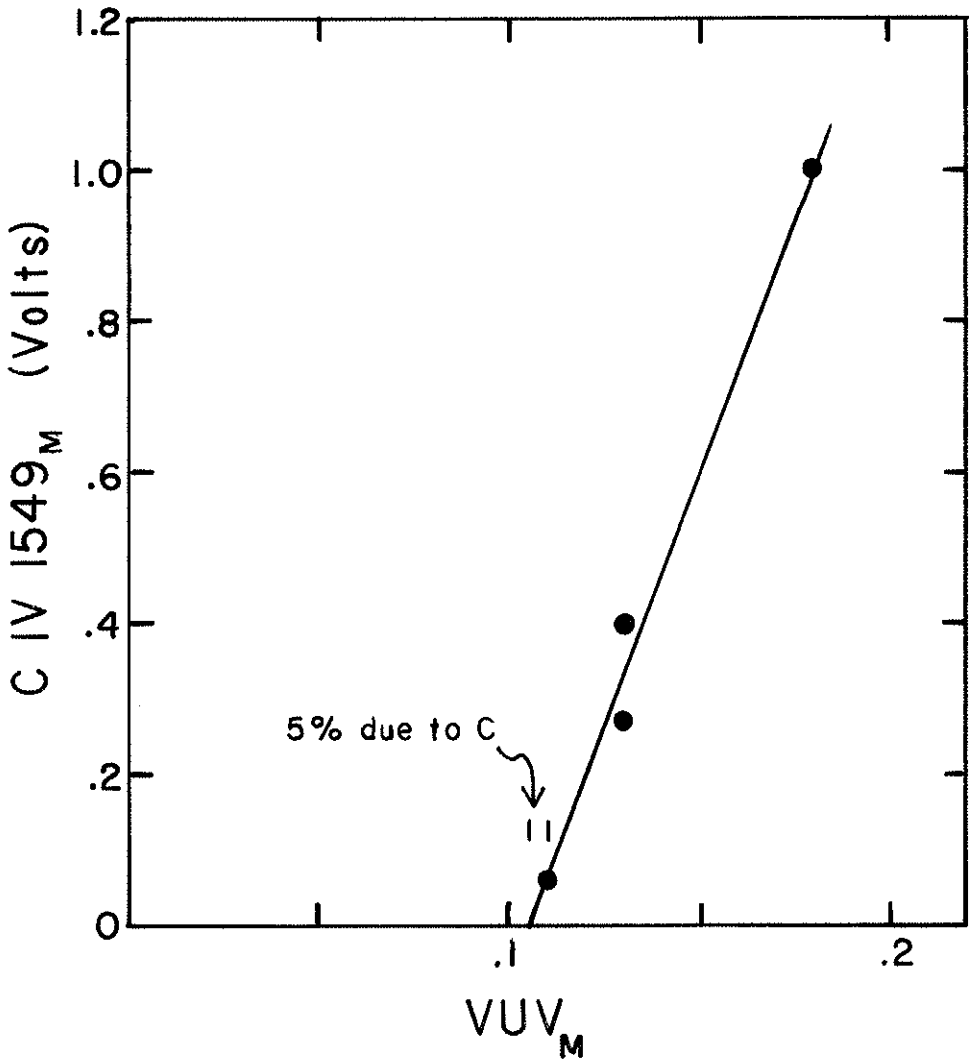
1.2
1.0
.8
.6
.4
.2
0
C IV 1549$_M$ (Volts)
5% due to C
.1
.2
VUV$_M$

Fig. 6-12: Brightness of N IV 765 ionization peak vs. the maximum VUV signal during N_2 doping run.

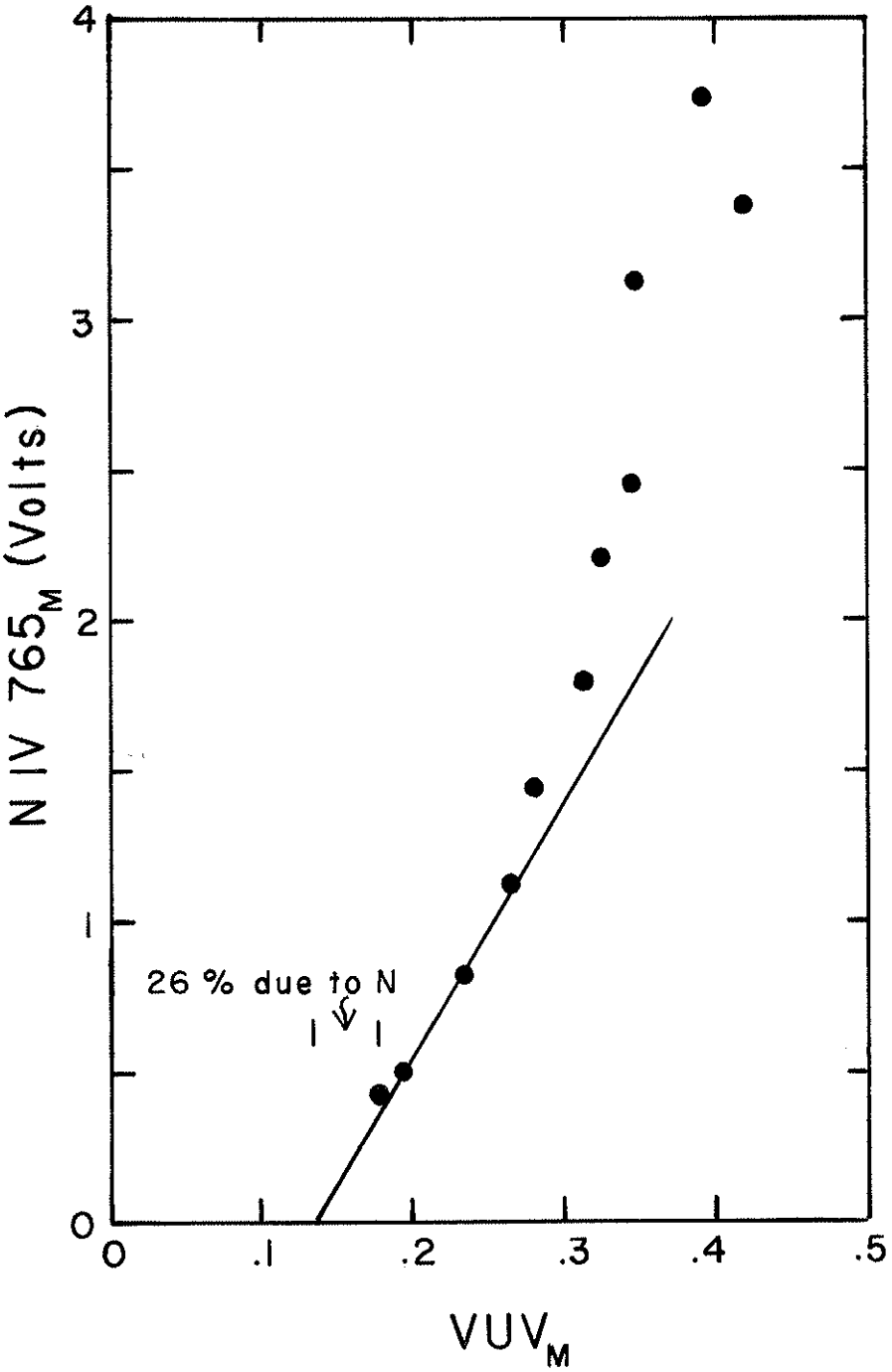
N IV 765$_M$ (Volts)
VUV$_M$
26 % due to N
0
1
2
3
4
0
.1
.2
.3
.4
.5

C.3. Z_{eff} Estimate

The results presented above permit an estimate of Z_{eff}.

It is often found that the impurity concentrations are fairly constant in time during tokamak discharges.[7,8] Thus, it will be assumed that the impurity concentrations of oxygen, carbon, and nitrogen in Tokapole discharges were constant at 3%, 0.5%, and 5%, respectively. It will be assumed that the unidentified impurity was entirely copper and that since a 3% oxygen impurity contributed 30% of the VUV signal, then copper was a 4% impurity and contributed 40% of the VUV signal. At the center of Tokapole discharges, all oxygen would ultimately have been in the OVII state, nitrogen would have been NVI, carbon would have been CV, and it is assumed that copper was Cu VIII. (These limit ions can be formed at a T_e of 100 eV, but their ionization potentials are so large that they cannot be ionized in turn.) Z_{eff} can now be calculated from the definition,

$$Z_{eff} = \frac{\sum_i n_i Z_i^2}{\sum_i n_i Z_i} , \qquad (6\text{-}2)$$

where the sum is performed over all of the ions, with densities n_i and charges Z_i, in the discharge. The calculation yields $Z_{eff} = 3.1$, and this number yields good agreement between the conductivity and spectroscopic estimates of T_e (Chapter 5). The probable limits on Z_{eff} are 2.5 and 3.5.

C.4. Amp-Second Behavior

The integral of the plasma current over time, called Amp-Seconds or AS (units of ampere-seconds), was a convenient parameter which indicated the quality of the discharge. Low values of AS (as low as 25)

were correlated with dirty, low temperature discharges. The highest values of AS achieved (100-130) were correlated with high temperatures, low values of radiated power, and long-lived discharges. With the assumption that the plasma obeys Spitzer conductivity, the AS parameter can be expressed in terms of several plasma parameters.[11]

$$AS \equiv \int_0^{t_f} I_p \, dt = \int_0^{t_f} J_{ll} \, A \, dt = 200 \int_0^{t_f} \frac{T_e^{3/2}}{Z_{eff} \ln \Lambda} E_T \, A \, dt, \quad (6\text{-}3)$$

where t_f = the time when the discharge ends (sec), I_p = plasma current (A), J_{ll} = toroidal current density (A/cm^2), A = plasma current cross section (cm^2), σ = parallel conductivity ($ohm^{-1}\ cm^{-1}$), E_T = toroidal electric field (V/cm), T_e = electron temperature (eV), Z_{eff} = average ionic charge, and $\ln \Lambda$ = coulomb logarithm $\approx$ 15. Since AS has a stronger dependence on T_e than on any other parameter, AS is a qualitative T_e indicator.

Data will now be presented which show that at low doping levels, AS was independent of the doping level. An explanation for this behavior will be given in the following section. Data will only be presented for oxygen since C and N caused very similar behavior of AS.

In Fig. 6-13, AS is plotted as a function of the oxygen doping density. With the lowest doping concentrations, AS was constant, and the parameter started to decrease after the O_2 dopant level reached about $2.5 \times 10^{11}\ cm^{-3}$. In Fig. 6-14, AS is plotted against the VUV signal, which is equivalently the radiated power signal. This graph is very similar to Fig. 6-13 because the VUV signal increased essentially linearly with the O_2 content. Figure 6-14 shows clearly that a substan-

Fig. 6-13: AS as a function of the O_2 doping concentration.

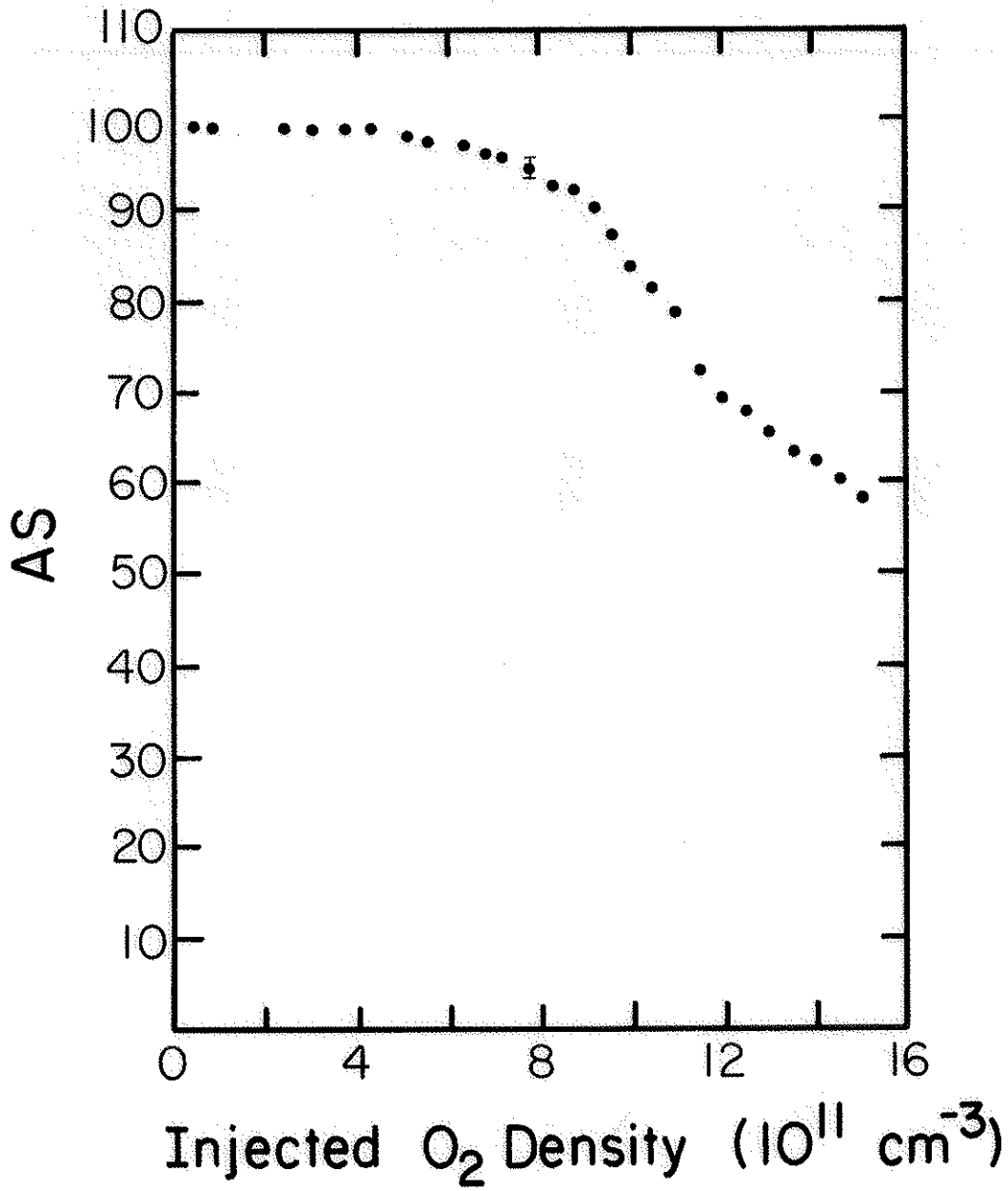
110
100
90
80
70
60
50
40
30
20
10
AS
0
4
8
12
16
Injected O_2 Density (10^{11} cm^{-3})

Fig. 6-14: AS vs. the maximum VUV signal, which is equivalent to radiated power. Conversion factor is 350 kW/V.

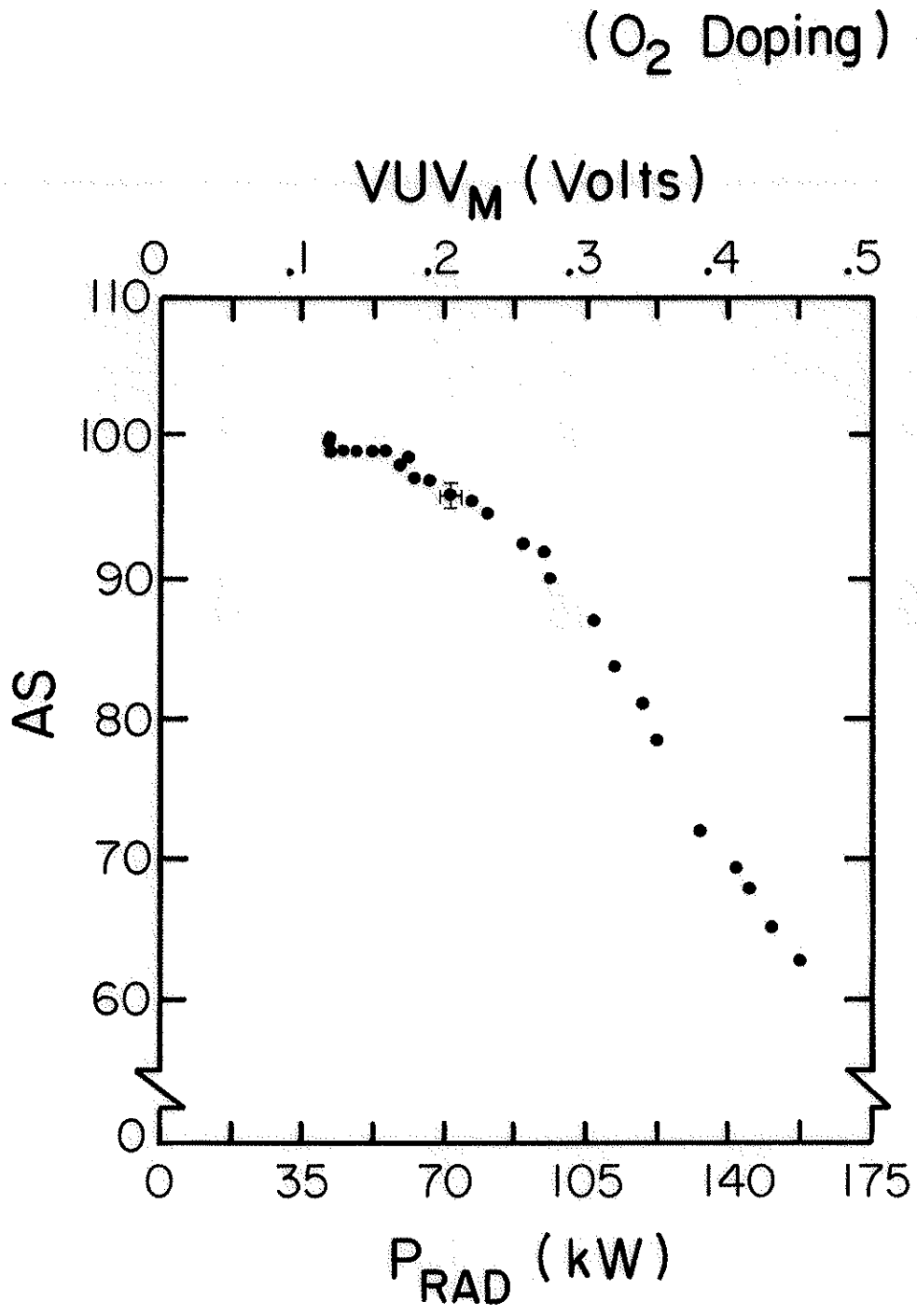
(O_2 Doping)
VUV_M (Volts)
0
.1
.2
.3
.4
.5
110
100
90
80
70
60
0
AS
0
35
70
105
140
175
P_{RAD} (kW)

tial increase (about 100%) in radiated power P_{rad} was achieved before AS started to decrease. Then, AS decreased linearly with the radiated power, and a straight line drawn through the points intercepts the P_{rad} axis at 270 kW (not shown), which is interpreted to be the ohmic input power. This number is consistent with the actual ohmic input power, of about 350 kW.

Figure 6-15 is a parametric plot of AS against the peak SXR signal SXR_M. With no doping, AS was 98 while SXR_M was 80. With increasing doping concentrations, the AS level remained constant, which is evidence that T_e was not changing. Also, the SXR signal was increasing because there was more oxygen available to radiate. Eventually, a level of doping was reached after which AS started to drop, and the SXR signal remained roughly constant. These observations indicate that the plasma was cooling. As the O_2 concentration was increased above about 1×10^{12} cm^{-3}, large oscillations were observed in the SXR signal (Fig. 6-16), and SXR_M decreased with increasing doping concentration. The oscillations most likely were associated with an instability, and the oscillations were probably correlated with a decrease in the plasma lifetime, although this was not studied in any detail.

C.5. Model of AS Behavior

The following model for the behavior of AS with doping is proposed. With no doping, the central current density was limited by internal disruptions at a q=1 surface. Sufficiently low doping levels were such small perturbations to the plasma that the disruptions still controlled the current density, and the current and AS were unaffected by the doping. As the doping level increased, the plasma resistivity increased

Fig. 6-15: AS and maximum soft x-ray signal plotted parametrically as functions of the O_2 doping concentration. The leftmost point on the upper part of the curve corresponds to no doping. Subsequent points along the curve correspond to increased dopant levels.

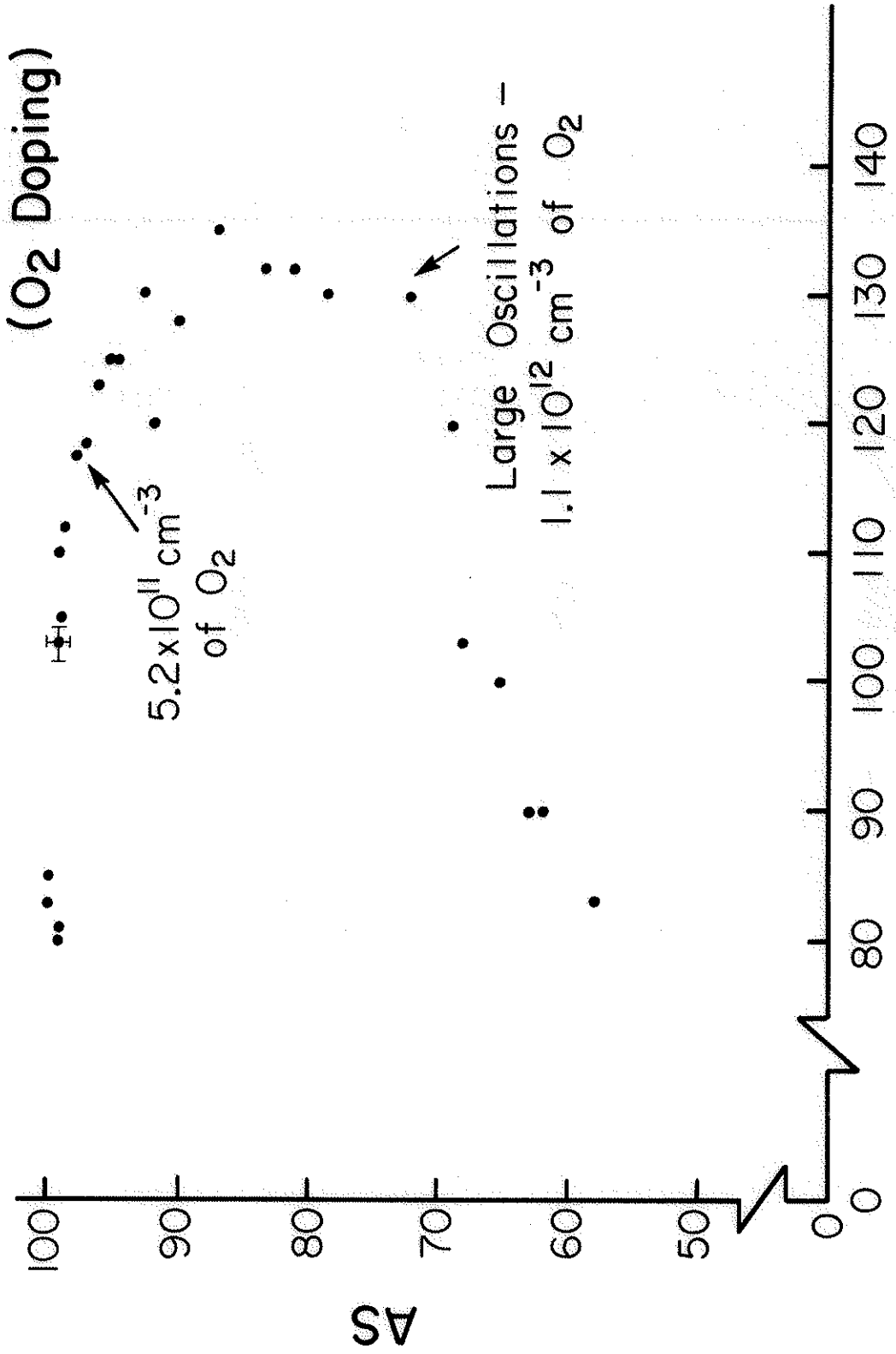
(O2 Doping)
5.2x10^11 cm^-3 of O2
Large Oscillations – 1.1 x 10^12 cm^-3 of O2
ΔS
SXRM (mV)
100
90
80
70
60
50
0
80
90
100
110
120
130
140

Fig. 6-16: Oscillations in OVI 1032, SXR, and VUV signals during heavy oxygen doping (1.2×10^{12} cm^{-3} of O_2). All traces from same discharge. In the lower picture, the smoother trace is the VUV signal.

OSCILLATIONS DURING HEAVY O_2 DOPING

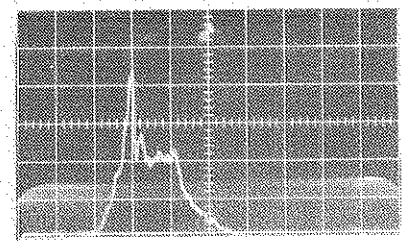

O VI 1032

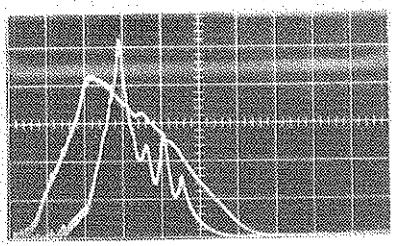

SXR & VUV

ALL TIME SCALES = 0.5 msec/d

(T_e dropped and Z_{eff} increased), and eventually the resistivity reached a level such that the available electric field could no longer drive the current to a q limit. At higher doping levels, the resistivity increased further, and then the current dropped; therefore, AS dropped. The current could drop since the ohmic heating power supply for Tokapole II was a voltage source, and this source produced an electric field which was not strongly dependent on the plasma properties. If the power supply had been a current source, then with an increase in the plasma resistivity, the electric field would have increased to maintain the current at a constant value.

This model fits the available evidence. Measurements with the large Rogowski coil have shown that during doping runs, the plasma current was of the form

$$I_p(t) = I_{pM}\, G(t), \qquad (6\text{-}4)$$

where G(t) is a function describing the time dependence of the plasma current, and G was independent of the doping concentration. The scale factor for the current I_{pM} was a constant for low doping levels and was a decreasing function of the dopant level for sufficiently high doping concentrations. Furthermore, measurements of toroidal current density and electric field were performed at the separatrix for a case with no doping and a case in which a large oxygen doping concentration was used. The electric fields were essentially identical for the two cases, and the current density in the doping case was about half of that in the undoped case.[12]

The q profiles presented in Chapter 5 (Fig. 5-11) show that for an

undoped plasma, q(0) dropped below one between 1.6 and 1.8 msec. This observation is consistent with the hypothesis that the SXR peak, which occurred at about 1.7 msec, indicated the onset of internal disruptions associated with a q=1 surface.

D. Impurity Production

A necessary condition for the successful control of impurity production is an understanding of the impurity sources. Possible mechanisms for the generation of low-Z impurities are desorption by ions, photodesorption, electron stimulated desorption, or desorption by neutrals.[13,14] Candidate mechanisms for the production of metallic impurities are sputtering, arcing, and evaporation.[15-17]

D.1. Location of Impurity Generation

An interpretation of available data is that during the turbulent start-up phase of Tokapole discharges, impurity generation occurred primarily at the walls; after the central current channel was well formed, the impurity generation occurred primarily at the rings.

Figure 6-17 is a comparison of the VUV, SXR and $\dot{B}$ signals with and without the divertor baffle in the plasma, and Fig. 6-18 is a comparison of the OIII-OVI resonance lines for the same two cases. When the baffle was inserted into the plasma, the VUV signal was reduced early in the discharge by about a factor of two; furthermore, the $\dot{B}$ signal was considerably quieter with the baffle in the plasma. The most direct interpretation is that early in the discharge, the baffle reduced the electron density and current density near the walls, where those quantities were normally peaked. The reduction in current density decreased the amplitude of the $\dot{B}$ oscillations and decreased the severity of the plasma-wall

Fig. 6-17: Comparison of VUV, SXR, and $\dot{B}$ signals from poloidal field without baffle (pictures on left) and with baffle in scrape-off region (pictures on right). Both $\dot{B}$ signals have same vertical scale. $\dot{B}$ time scale was 0.2 msec/d as opposed to 0.5 msec/d for other signals. VUV and SXR traces are each overlays from two shots.

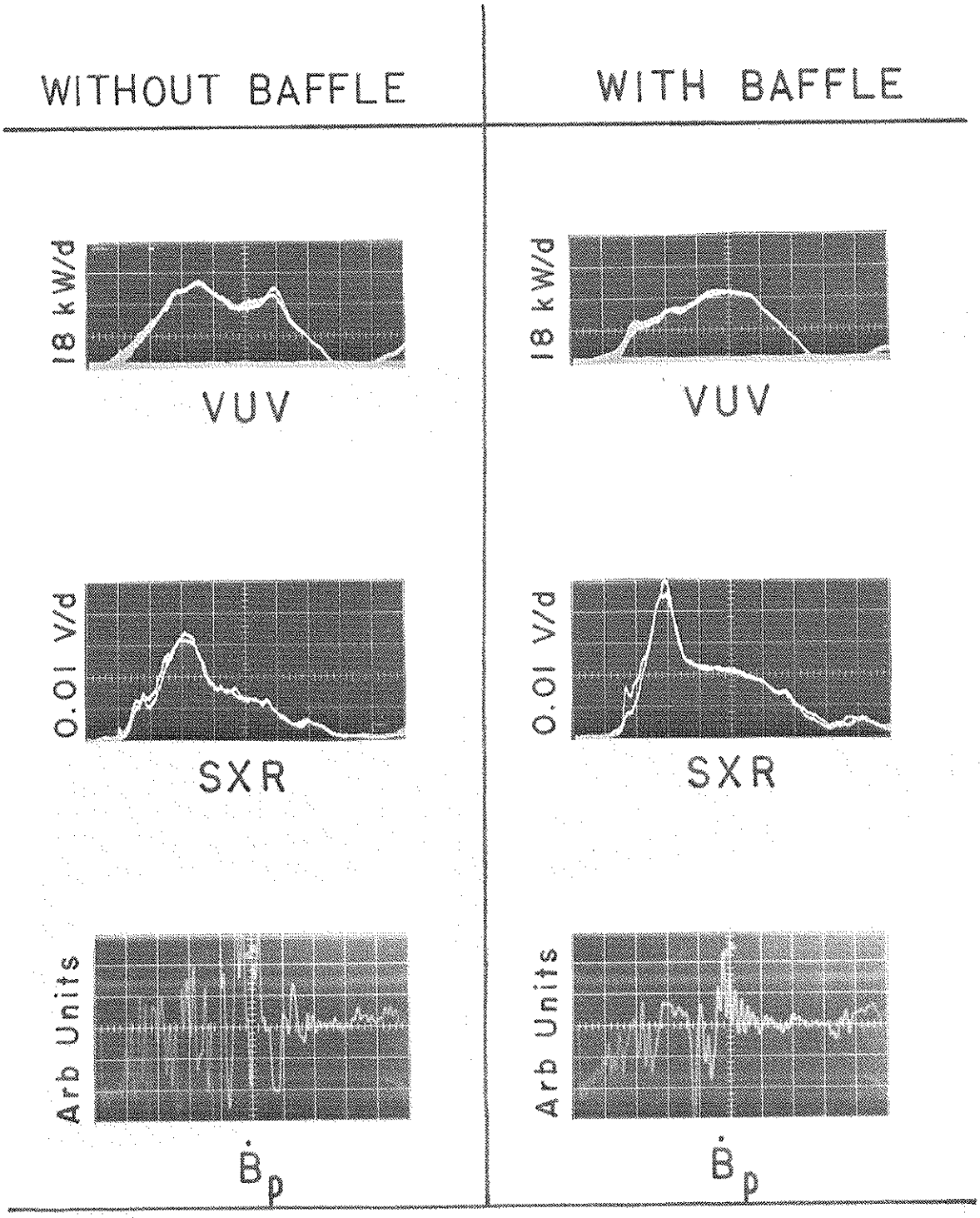
WITHOUT BAFFLE
WITH BAFFLE
18 kW/d
VUV
18 kW/d
VUV
0.01 V/d
SXR
0.01 V/d
SXR
Arb Units
$\dot{B}_p$
Arb Units
$\dot{B}_p$
$\dot{B}_p$ TIME SCALE = 0.2 msec/d
OTHER TIME SCALES = 0.5 msec/d

Fig. 6-18: Comparison of brightness of emission lines from OIII to OVI without baffle (pictures on left) and with baffle in scrape-off region (pictures on right). Each trace is an overlay from two shots.

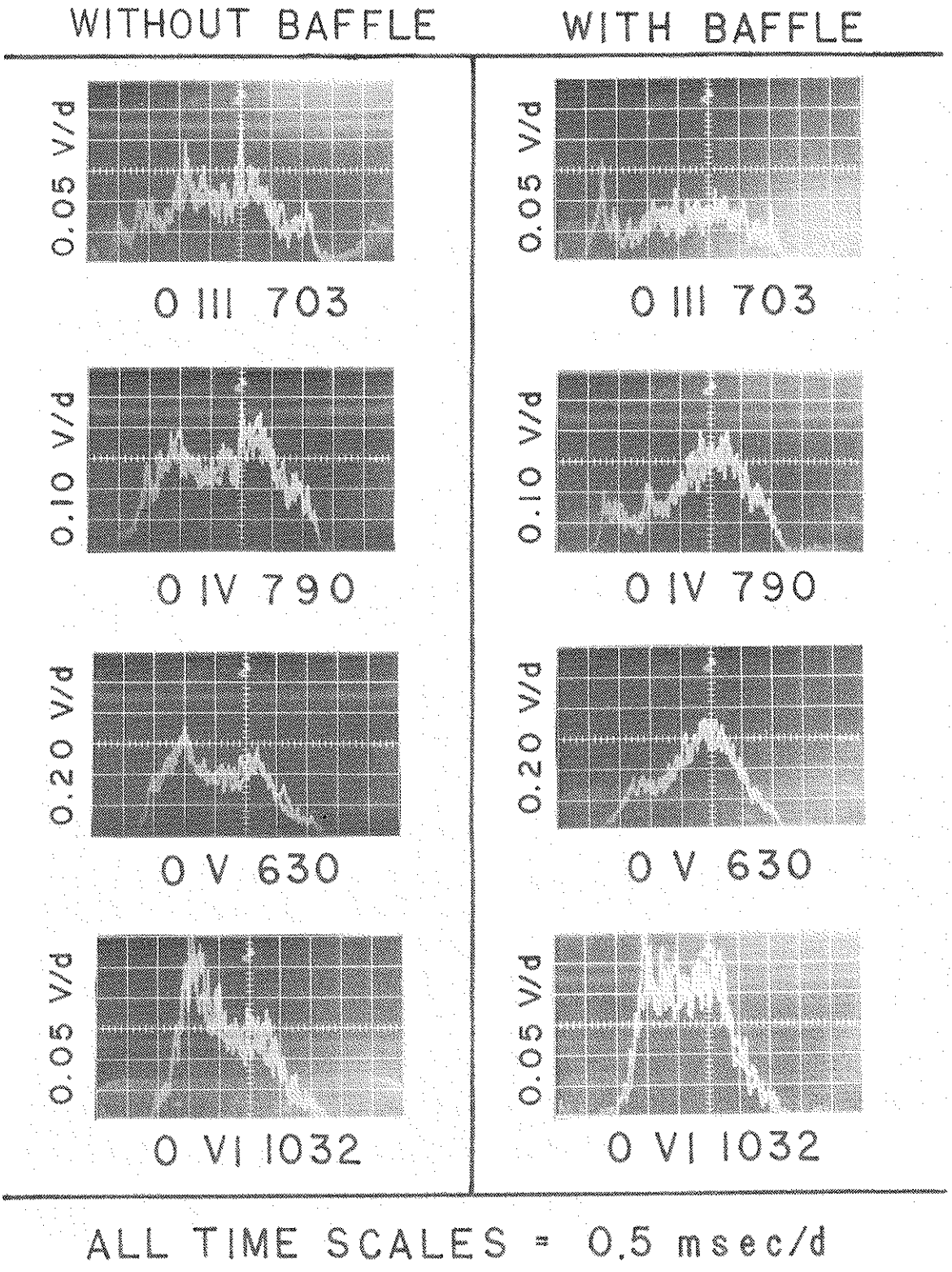
WITHOUT BAFFLE
WITH BAFFLE
0.05 V/d
O III 703
0.05 V/d
O III 703
0.10 V/d
O IV 790
0.10 V/d
O IV 790
0.20 V/d
O V 630
0.20 V/d
O V 630
0.05 V/d
O VI 1032
0.05 V/d
O VI 1032
ALL TIME SCALES = 0.5 msec/d

interaction; therefore, the impurity generation was reduced.

After the current penetrated to the center, the hot plasma is expected to have interacted primarily with the rings. The baffle, which intercepted the private flux of only one of the internal rings, would have been unable to reduce the plasma density near the other three rings. The impurity production and thus the VUV signal, during the steady phase of the discharge, would then have been relatively unaffected by the presence of the baffle. Supporting evidence for the impurity generation at the rings is that spatial data taken with various broadband light detectors often showed a lobe of impurity emission concentrated near one of the rings.

The SXR signal was larger with the baffle in place than without it. This suggests that the presence of the baffle allowed T_e to rise or the baffle was a source of impurities which radiated in the SXR region. Some of the oxygen lines (OIV 790, for instance) behaved in accordance with the model which has been presented. However, some features of the line radiation, such as the observation that OVI was generally higher with the baffle than without it, are not explained by the model. It is possible that the presence of the baffle changed the locations of impurity generation and perhaps changed the impurity transport in the machine. There is also strong evidence that the impurity generation is very asymmetric, and this could explain the data of Fig. 6-18.

D.2. Metallic Impurities

The sputtering yields from 10-20 eV protons are so low[18] that it is clear that the protons in Tokapole II discharges could not have caused the metal production which was observed in the machine. Visual examin-

ation of the interior of the vacuum vessel indicated that arcing of the aluminum tank has occurred, especially in the upper half of the machine, and the two lower rings have been sputtered or have been damaged by arcs. Erosion from the rings occurred primarily at those areas closest to the central current channel. Arc tracks have been observed on the divertor baffle and the tank protecting the large Rogowski coil.

Recent tokamak results indicate that the sheath potentials in the vicinity of metals in contact with the plasma are very important in metal production,[15-17] and sheath effects must be invoked to explain the metal production in Tokapole II. The sheath potential occurs because electrons escape from a plasma faster than the ions, and then the plasma becomes positively charged to retard the escape of the electrons. Most of the potential drop occurs near a wall, limiter, or other metallic object inserted in the plasma. The magnitude of the sheath potential V can be estimated from[19]

$$V = \frac{kT_e}{2e} \ln \left(\frac{m_p}{2\pi m_e}\right) \quad , \tag{6-4}$$

where m_p is the proton mass, m_e is the electron mass, and e is the electronic charge. If T_e near the walls and rings was 15-30 eV, then the sheath potential would have been of the order of 45-90 V. A multiply-charged ion falling through this potential drop would have hit a surface with an energy of a few hundred eV. (The ion's energy would have been Z.eV.) Such an ion would have had a significant sputtering yield.

Unipolar arcs, which also depend on the existence of sheath potentials,[19] have evidently occurred in Tokapole II. Clearly, an under-

standing of metal production in Tokapole II rests on an understanding of the sheath potentials in the machine.

A simple experiment was performed in which a 14,000 μF capacitor bank was used to simultaneously bias all four rings with respect to the tank during a discharge. Figure 6-19 shows the temporal behavior of CuI 3250 for discharges in which the applied ring bias was 90 V, O V, and -90 V with respect to the tank. Also shown is the floating potential with respect to the tank from a Langmuir probe which was in the scrape-off region. During the biasing operations, about 600 A of current were drawn from the capacitors until they were discharged. Thus, the bias voltage had dropped to about half of its value after the first msec of the discharge.

Although Fig. 6-19 shows that the biasing affected the Cu radiation and therefore the Cu production rate, the results were ambiguous. It had been expected that a positive bias on the rings would reduce the Cu production rate. This reduction evidently occurred between 0.3 and 0.4 msec, but between 0.2 and 0.3 msec, the Cu production was enhanced slightly. The negative ring bias reduced the copper signal during most of the discharge. The results suggest that good control of the copper generation might be achieved with an adequate power supply and optimization of the biasing technique.

The floating potential followed the bias voltage quite well. In all cases, the floating potential had large (~ 50 V) but entirely reproducible fluctuations. These fluctuations did not obviously correlate with impurity production, but a more detailed study of the potential in the vicinity of the rings would probably be instructive.

Fig. 6-19: Brightness of CuI 3250 and floating potential V_f measured with a probe in the scrape-off region for ring bias of 90 V (top picture), 0 V(middle picture), and minus 90 V (bottom picture). In each picture, upper trace is V_f signal and lower trace is CuI 3250 signal. All light signals have same vertical scale. Each trace is an overlay from three shots.

RING BIASING DATA

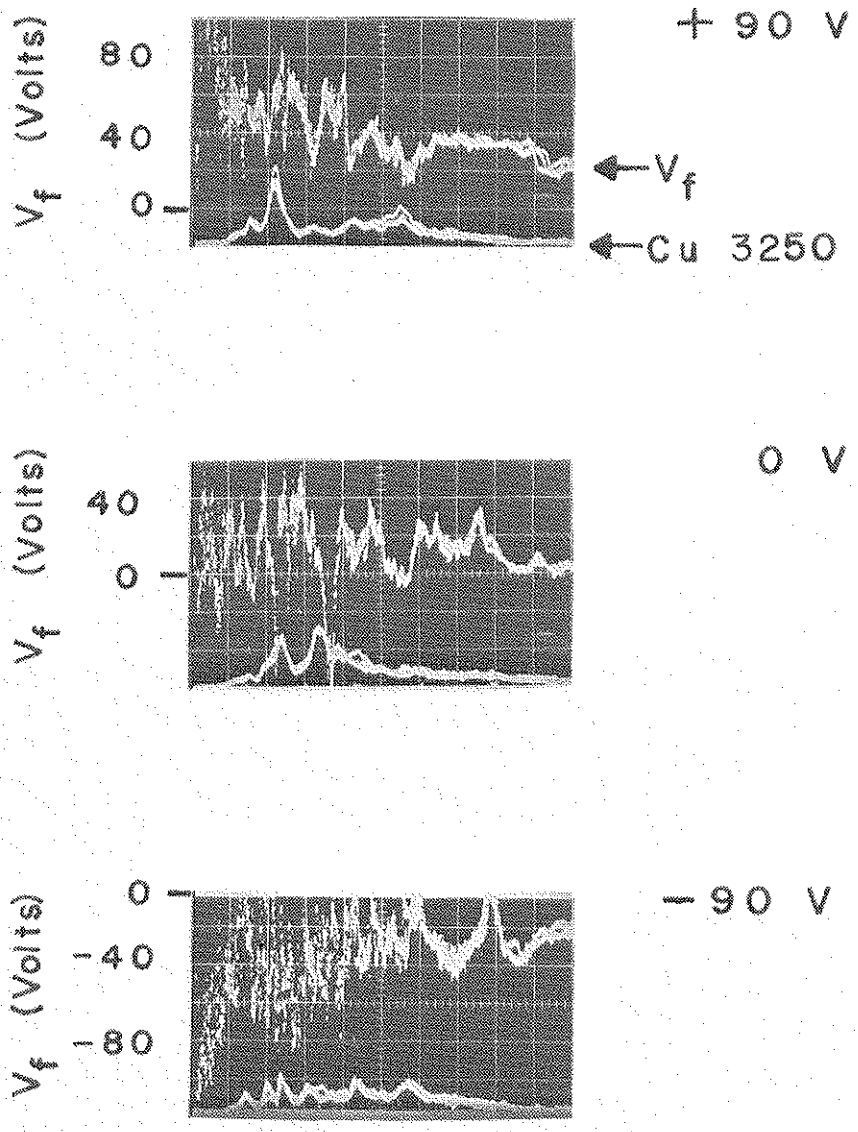

ALL Cu 3250 TRACES HAVE SAME UNITS.
ALL V_f TRACES ARE 20 VOLTS/d.
ALL TIME SCALES = 0.2 msec/d.

REFERENCES

1. W. L. Wiese, M. W. Smith, B. M. Glennon, Atomic Transition Probabilities, NSRDS-NBS 4 Report, National Bureau of Standards, 1966.

2. S. Bashkin, J. O. Stoner, Jr., Atomic Energy Levels & Grotrian Diagrams 1 (North-Holland Publishing Co., Amsterdam, 1975).

3. R. L. Kelly, L. J. Palumbo, Atomic and Ionic Emission Lines Below 2000 Angstroms, NRL Report 7599 (Naval Research Laboratory, Washington, D.C., 1973).

4. A. N. Zaidel, V. K. Prokofiev, S. M. Raiskii, Tables of Spectrum Lines (Pergamon Press, New York, 1961).

5. R. J. Groebner, R. N. Dexter, University of Wisconsin Plasma Studies PLP 769, 1978.

6. R. J. Groebner, University of Wisconsin Plasma Studies PLP 791, 1979.

7. E. Hinnov et al., Plasma Phys. 20, 723 (1978).

8. Equipe TFR, Nucl. Fusion 15, 1053 (1975), and Euratom-CEA Association Fontenay-aux-Roses, Report EUR-CEA-FC-777, 1975.

9. S. Von Goeler, W. Stodiek, N. Sauthoff, Phys. Rev. Lett. 33, 1201 (1974), and Princeton Plasma Physics Lab. Rep. MATT 1058, 1974.

10. R. J. Groebner, R. N. Dexter, University of Wisconsin Plasma Studies PLP 770, 1978.

11. F. Chen, Introduction to Plasma Physics (Plenum Press, New York, 1974), p. 162.

12. B. Lipschultz, private communication.

13. P. Staib, G. Staudenmaier, J. Nucl. Materials 76 & 77, 78 (1978).

14. T. F. R. Group in Proceedings of the International Symposium on Plasma Wall Interaction, Jülich, 1976 (Pergamon Press, New York, 1977), p. 3.

15. G. M. McCracken, D. H. J. Goodall, Nucl. Fusion 18, 537 (1978).

16. K. Ohasa, et al., Nucl. Fusion 18, 872 (1978).

17. R. J. Taylor, L. Oren, Phys. Rev. Lett. 42, 446 (1979).

18. M. Nishi, E. Rosengaus, M. Yamada, S. Suckewer, Princeton Plasma Physics Lab. Rep. PPPL-1521, 1979.

19. A. E. Robson, P. C. Thonenann, Proc. Phys. Soc. (London) 73, 508 (1959).

CHAPTER SEVEN

TEMPERATURE MEASUREMENTS

This chapter describes the measurement of electron temperature by two spectroscopic techniques and the use of Doppler broadening to measure the ion temperature.

A. Rate Coefficients

The electron temperature measurements described here require a knowledge of several rate coefficients. Few experimental measurements of rate coefficients exist, so the coefficients are usually obtained from theoretical calculations. Useful reviews of coefficients are provided in the literature.[1,2]

Lotz has provided the best available compilation of electron ionization rate coefficients, which are expressed in terms of a semi-empirical formula.[3] Salop has performed a more recent and detailed calculation for a limited number of ions.[4] Photorecombination rate coefficients have been calculated by several authors, and their results agree to within a factor of about two.[5,6,7] Burgess provided a convenient prescription for calculating dielectronic recombination rate coefficients.[8] Several authors have used this prescription to calculate these coefficients, but the results often differ by almost an order of magnitude. At tokamak electron densities, the dielectronic recombination rate coefficient is a function of n_e, but the dependence is extremely difficult to take into account accurately.[9] A simple correction to the Burgess formula to account for n_e is given in Ref. 10.

Kunze and Johnston have published experimentally measured electron excitation rate coefficients for lithium-like and beryllium-like ions.[11,12]

Electron excitation rate coefficients are often conveniently expressed in terms of Van Regemorter's formula:[5,13]

$$Q = 1.6 \times 10^{-5} \frac{f \bar{g}(\beta) \beta^{1/2}}{\Delta E^{3/2}} e^{-\beta} \qquad (7\text{-}1)$$

where Q is the rate coefficient in cm^3/sec, f is the absorption oscillator strength for the transition under consideration, $\bar{g}$ is the average effective Gaunt factor (usually of order unity), ΔE is the excitation energy in eV and $\beta = \Delta E/T_e$ where T_e is in eV. Convenient compilations of oscillator strengths and of excitation energies exist,[14-16] and several theoretical calculations have obtained values for the Gaunt factors.[13,17-21] Many calculations have not been based on the Gaunt factor formulation. Vainshtein et al. have performed calculations for a number of transitions in light atoms and ions.[22] Breton et al. have conveniently tabulated the information needed to use these calculations for oxygen ions,[5,23] while Sobelman has provided additional information on the formulas used in Ref. 22.[24] The most recent compilation of a large number of calculations has been assembled by Magee et al.[25] These may be the most accurate rates available. A comprehensive survey of experimental and theoretical work on excitation rate coefficients for a large number of ions is available in Atomic Data for Fusion.[26] Moiseiwitsch and Smith have published an older review of excitation rates and a critique of the calculations used to obtain the rates.[27]

B. Electron Temperature in the Dirty Discharge

The electron temperature in the dirty discharge was obtained by a line ratio technique used on the Model C Stellarator.[28] This method uses formula 4-14 of Chapter 4:

$$\frac{E_{m,k}}{E_{n,j}} = \frac{\Gamma_{m,k}\, Q_{g,m}(T_e)}{\Gamma_{n,j}\, Q_{g,n}(T_e)} \quad . \tag{7-2}$$

Line pairs used were OIV 790-OIV 610, OIV 790-OIV 554, and OIII 703-OIII 508. The branching ratio was 1 for all lines and the excitation rates were expressed in terms of Eq. (7-1) with $\bar{g}$ set equal to 0.2. Since all of these lines are resonance lines, Eqn. 7-2 became

$$\frac{E_{m,g}}{E_{n,g}} = \frac{f_{g,m}\ \lambda_{m,g}}{f_{g,n}\ \lambda_{n,g}} \exp\left[(E_n - E_m)/T_e\right] \tag{7-3}$$

where $f_{g,m}$ is the absorption oscillator strength from the ground state to level m, λ_{mg} is the wavelength of the photon emitted from level m and E_m is the energy of level m. With Eq. (7-3) and the intensity ratios of the line pairs, it was determined that T_e was about 10 eV, which was in good agreement with Langmuir probe and conductivity measurements of T_e.

C. Computer Modeling of Oxygen Radiation

To measure T_e in the standard discharge, the oxygen radiation was modeled with a numerical computer code, as has been done on other tokamaks.[29-31] With an added dopant of 7×10^{11} cm^{-3} of oxygen to enhance the ionization peaks of the oxygen ions, the temporal evolution of those ions appeared as is illustrated in Fig. 7-1. The time dependent coronal model described in Chapter 4 was applied to the oxygen ions. The time evolution of the oxygen ion densities was calculated from the set of equations (4-7), and the emission of resonance lines of those ions was calculated from Eq. (4-4). The line-averaged electron density was obtained from the following analytical fit to the density curve in

Fig. 7-1: Experimentally observed emissions from OIII 703, OIV 789, OV 630, and OVI 1034. The OIV 789 signal is the sum of the OIV 787.7 and OIV 790.2 signals, which are both produced by the same multiplet. The OVI 1034 signal is the sum of the OVI 1032 and OVI 1037.6 signals. All light signals have been corrected with relative calibration curve of 1-m Seya.

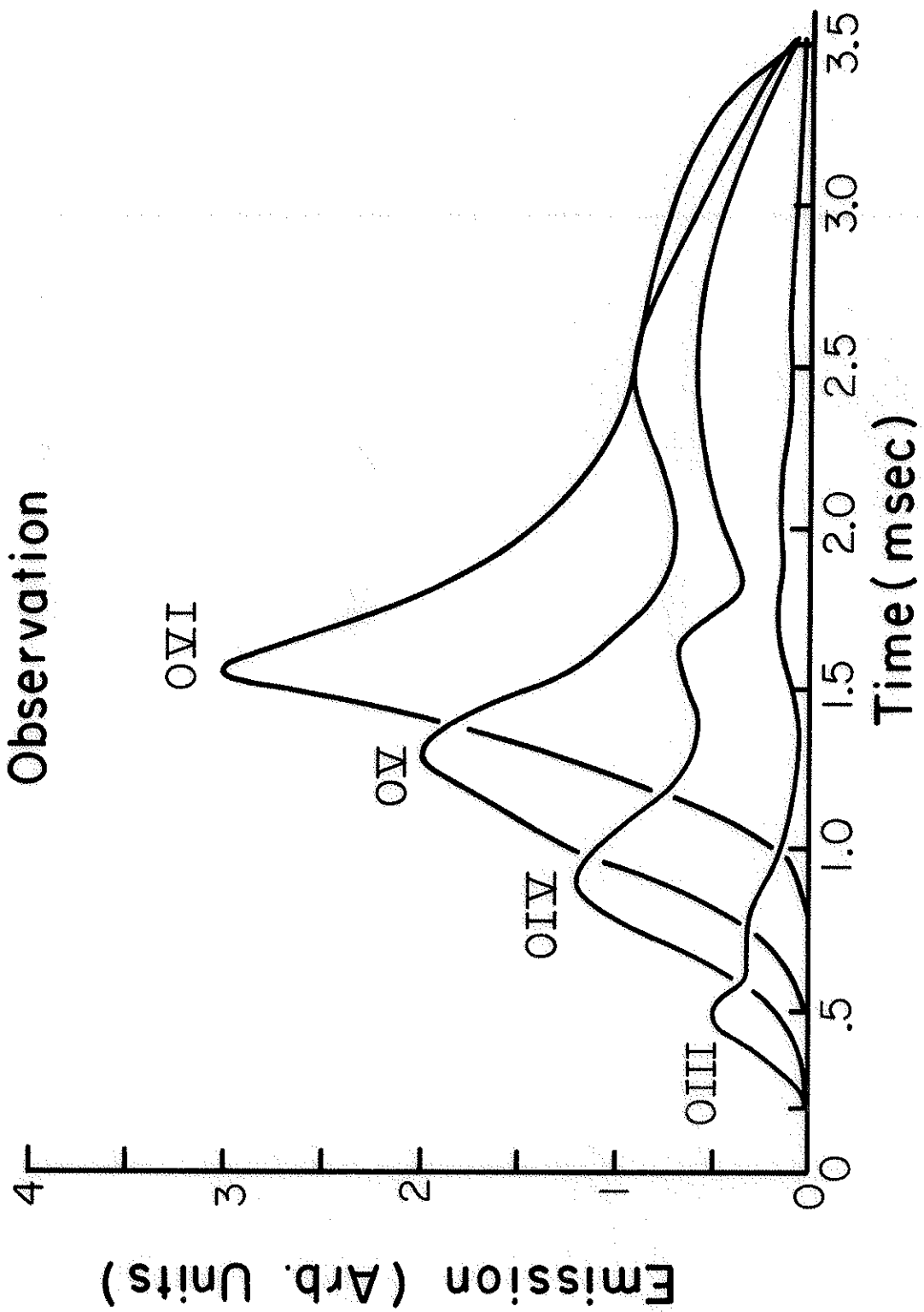
Observation
IAO
AO
AIO
IIIO
Emission (Arb. Units)
Time (msec)
0
1
2
3
4
.5
1.0
1.5
2.0
2.5
3.0
3.5

Fig. 5-1:

$$\bar{n}_e = \begin{cases} 1.0 \times 10^{11}, & 0 \leq t \leq 0.1 \text{ ms} \\ 9.373 \times 10^{12} \ \text{Exp}(-.1803\sqrt{(t-.1)})(1-\exp(-1.867(t-.1))), & 0.1 < t \leq 1.5 \\ 8.68 \times 10^{12}\, t^{.8966} \ \text{Exp}(-.3766t), & 1.5 < t \leq 10.0 \text{ ms} \end{cases} \quad (7\text{-}4)$$

where t is the time in msec, and $\bar{n}_e$ is in cm^{-3}. Spatial data from the spectroscopic emissions indicated that light was coming preferentially from the region of the central current channel. Therefore, the electron density used in the computer code was taken as 1.35 times the density of Eq. 7-4, to account for the higher density in the center of the machine. The initial atomic oxygen density was assumed to be 10.5×10^{11} cm^{-3}, and the influx term was set equal to zero, since the development of the ion densities was dominated by the initial oxygen concentration. A particle containment time of 3 msec was assumed for all of the ions as this number provided good agreement with the observations.

The ionization rate coefficients were from Lotz,[3] the photorecombination rate coefficients were from Aldrovandi and Péquignot,[7] the dielectronic recombination rate coefficients were from Beigman *et al.*[6] and the electronic excitation rate coefficients were those of Vainshtein *et al.*[22] The required formulas and coefficients for the excitation rate coefficients were taken from Ref. 23 and from M. Mattioli,[32] who provided the coefficients needed for the excitation rates for individual terms in the 2s-2p excitations for OIII and OIV. In the terminology of reference 23, the q's for the ^3P-^3S, ^3P, ^3D transitions in

OIII are respectively, 4/9, 3/9, 5/9 while A is 9.8 for all terms. For the ^2P-^2S, ^2P, ^2D terms in OIV, the q's are, respectively, 1/9,1, 5/9 while A is 9.1. Graphs of the ionization and recombination rate coefficients can be found in Ref. 1. (The recombination rate coefficients used for the calculation being discussed differ slightly from those in Ref. 1, since different sources for photorecombination were used in Ref. 1 and in the work reported here.) Graphs of some of the excitation rates are displayed in Refs. 1 and 19. Of interest is the fact that the resonance lines of the oxygen ions all have rate coefficients which are about 2×10^{-8} cm^3/sec and are essentially independent of electron temperature.

In the simulation, the function $T_e(t)$ was varied until the calculated times of the ionization peaks agreed with the observed times. The function which successfully did this is illustrated in Fig. 5-4, and its analytic form is:

$$T_e = \begin{cases} 22.42 \exp\left(-16.09(t-.5)^2\right), & 0 \leq t \leq .5 \text{ ms} \\ 22.44, & .5 < t \leq .9 \\ 20.02 + 96.45 \exp\left(-5.10(t-1.75)^2\right), & .9 < t \leq 2.0 \end{cases} \quad (7\text{-}5)$$

where t is in msec. Figure 7-2 shows the calculated time evolution of the oxygen ions. At the time of the OVI ionization peak (1.54 msec), the calculated T_e was 97 eV, and this technique could not be used to estimate T_e after the OVI peak. However, the SXR signal peaked between 1.7 and 1.8 msec, and this peak is interpreted to have indicated the peak in T_e also. In that case, the maximum T_e could not have been very much higher than T_e at the OVI peak; therefore, the peak electron

Fig. 7-2: Time evolution of the emissions of OIII 703, OIV 789, OV 630, and OVI 1034 as obtained from a time dependent coronal computer simulation. No oxygen influx included.

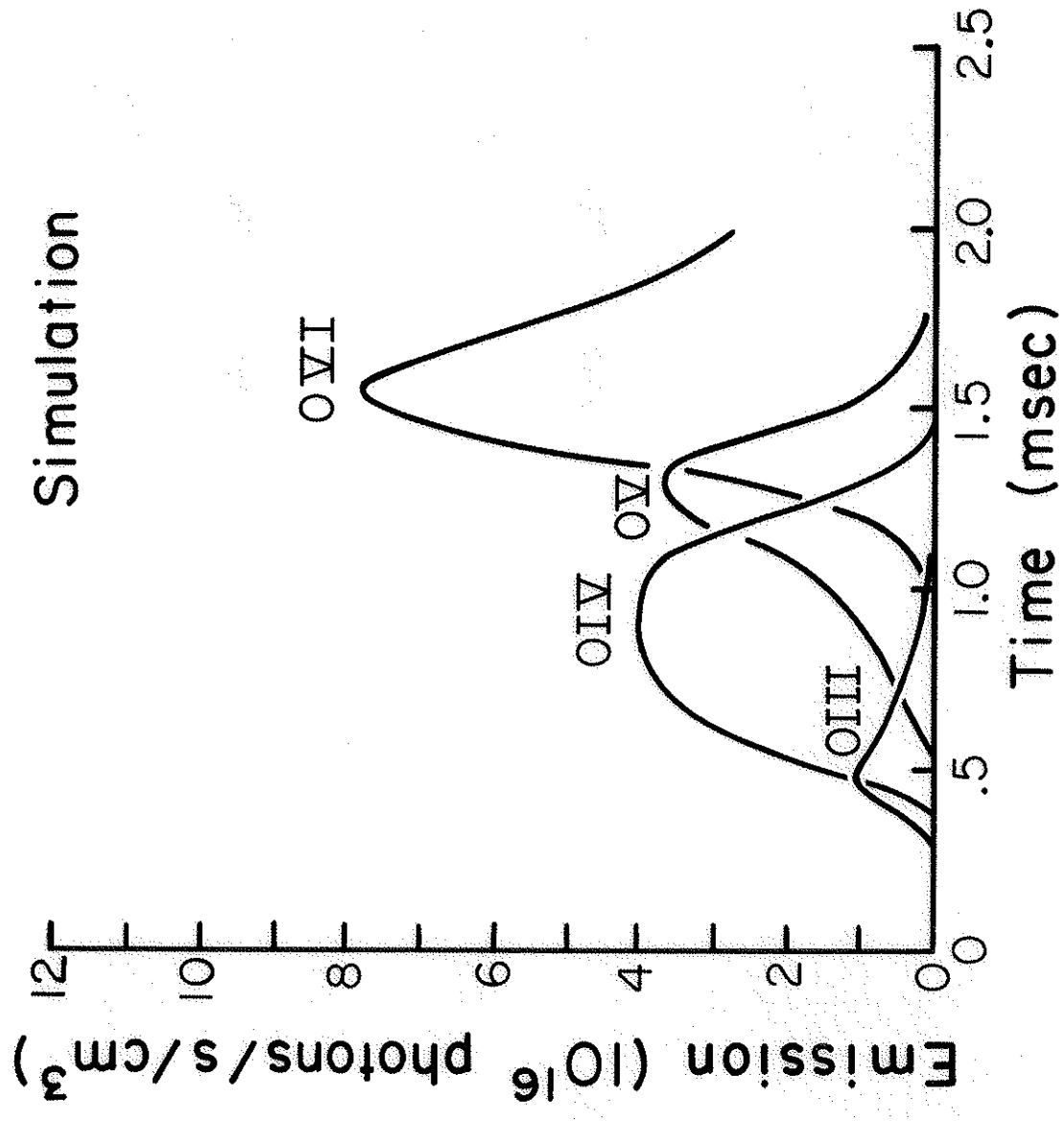
Simulation
Emission (10^{16} photons/s/cm^3)
Time (msec)
0
2
4
6
8
10
12
.5
1.0
1.5
2.0
2.5
1IIO
1AO
0AO
1AO

temperature was about 100 eV.

The largest errors in the estimate of T_e are due to uncertainties in the electron density and in the ionization rate coefficients. Furthermore, the calculation ignored spatial variations of any plasma quantities and provided an estimate of the average electron temperature of the central current channel. The accuracy of the calculation of the volume-averaged T_e is estimated to be within 50%.

When the calculation described above was first performed, the calculated ratio of the peak emission of OV 630 to that of OVI 1034 was about a factor of 3.1 larger than that observed experimentally. This occurence has been noted by other authors.[29,30,33] With the ground state densities of OIII-OV corrected for the fact that those ions have metastable levels, the agreement between the OV 630 and OVI 1034 lines was much better. The correction factors for the metastable levels were taken from Ref. 30, and the data of Figs. 7-2 and 7-3 include the corrections. As the calculation stands, OIV 789 now provides the poorest agreement with the observations, and this may be due to uncertainties in the correction for the metastable levels or to uncertainties in the excitation rates.

D. Impurity Influx

Figure 7-1 shows that the experimentally observed emissions had relatively constant plateau values after the ionization peaks. These plateau values are attributed to an impurity influx,[29] and an attempt was made to include the influx in the computer model. Spatial measurements of impurity distributions in tokamaks have shown that the incoming

impurities form cylindrical shells, centered on the current axis, in regions where the electron energy is comparable to or less than the ionization energy of the ions. In the TFR tokamak, the shell of any oxygen ion was centered at a radius where the electron energy was one-third of the ionization energy of the ion.[34] Measurements on the DIVA tokamak showed that the impurity radiated power was proportional to the plasma current;[35] therefore, the impurity influx was probably proportional to I_p.

Reasonable success with the computer calculation was achieved with the following assumptions. The influx term was assumed to be proportional to the plasma current, measured by the current monitor, and was assumed to consist entirely of OI. The calculated resonance line emissions of Fig. 7-2 were combined with the observed signals of Fig. 7-1 to provide a crude absolute calibration of the 1-m Seya. The plateau signals of Fig. 7-1 were then converted into brightnesses, each ion was assumed to be in a region where T_e was one-third of its ionization energy, and Eq. 4-27 was used to estimate the particle influx rate ϕ_o. Within an order of magnitude, ϕ_o was found to be about 6×10^{14} atoms/cm^3/sec at the current peak (44 kA). The influx was then expressed as

$$\phi_o(t) = 1.36 \times 10^{13} \, I_p(t), \tag{7-6}$$

where ϕ_o has units of atoms/cm^3/sec and I_p is in kA. The plasma current was expressed analytically by

$$I_p = 1.72 \times 10^7 \, t^{9.97} \, \mathrm{Exp}(-13.3\, t), \quad 0 < t \leq .9 \text{ ms}$$

$$I_p = 41.2 \, t^{.3193} \, \mathrm{Exp}(-.0529\, t), \quad .9 \text{ ms} < t \leq 1.6 \text{ ms}$$

$$I_p = 44. - 10.65 \, (t-1.6)^{1.62}, \quad 1.6 \text{ ms} < t \leq 40 \text{ ms} \tag{7-7}$$

The electron density was taken from Eq. 7-4, and each ion was assumed to be in a region where the electron energy was one-third of its ionization energy. The initial impurity concentration was set equal to zero, and the electron temperature was assumed to go linearly to zero between 3.5 and 4.0 msec.

Figure 7-3 shows the result of adding the impurity densities calculated from the influx modeling to the Fig. 7-2 densities, which did not include an influx term. A comparison of Fig. 7-1 and 7-3 shows that the modeling of the influx term produced reasonable agreement with the observations. This model is the only way found to explain the plateau signals; the assumption that the influxing impurities were in the hot central channel produced very poor accord with the observations. Without spatial profiles of the impurity densities, the electron temperature, and the electron density, it is not reasonable to attempt a better match of the calculation to the observations, as many unjustifiable assumptions would have to be made in the calculation.

E. Ion Temperature Measurements

A spectral line produced from motionless ions will be very sharp in wavelength space (Fig. 7-4a). When a monochromator is scanned in wavelength across a sharp line, the line is broadened due to the finite resolution of the instrument (Fig. 7-4b). The instrumental resolution is defined to be the full-width-at-half-maximum (FWHM) of the instrumental profile of a sharp line and will be denoted as $\delta\lambda_{INS}$. Ions which are in motion towards and away from the monochromator will have Doppler-shifted wavelengths and will further broaden the profile of the observed line (Fig. 7-4c). If the ions have a Maxwellian distribution, the Doppler-

Fig. 7-3: Time evolution of the emissions of OIII 703, OIV 789, OV 630, and OVI 1034 as obtained from a time dependent coronal computer simulation. Oxygen influx included.

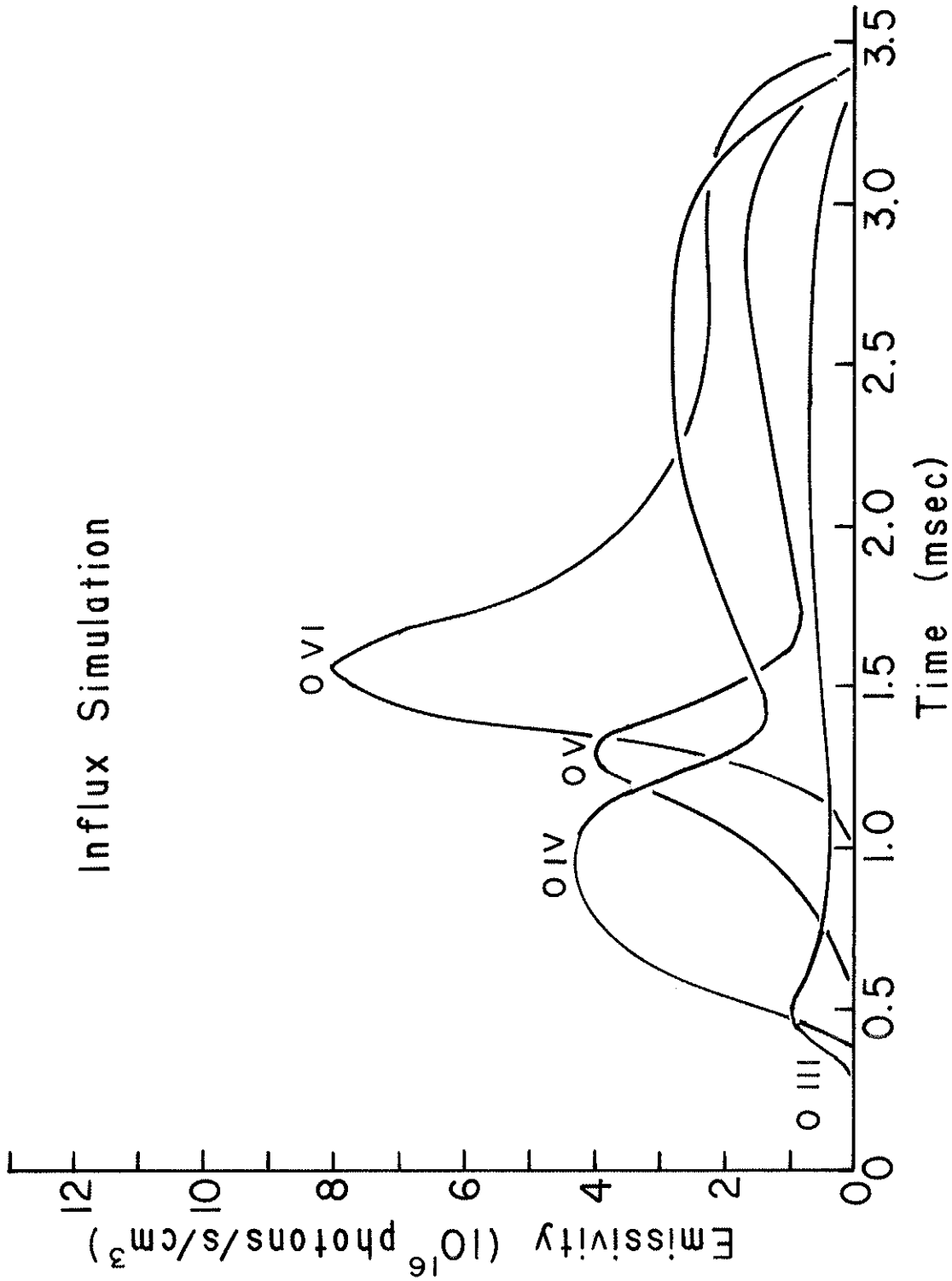
Influx Simulation
Emissivity (10^{16} photons/s/cm^3)
Time (msec)
O VI
O V
O IV
O III
0
2
4
6
8
10
12
0.0
0.5
1.0
1.5
2.0
2.5
3.0
3.5

Fig. 7-4a: Intensity of an emission line as a function of wavelength. For radiating ions at rest with respect to the observer, the line is sharp.

Fig. 7-4b: Instrumental profile of a monochromator obtained when the instrument views a sharp emission line and is scanned in wavelength.

Fig. 7-4c: When radiating ions are in motion with respect to the observer, the line profile obtained with the monochromator is a convolution of the instrumental profile and the true Doppler profile of the line.

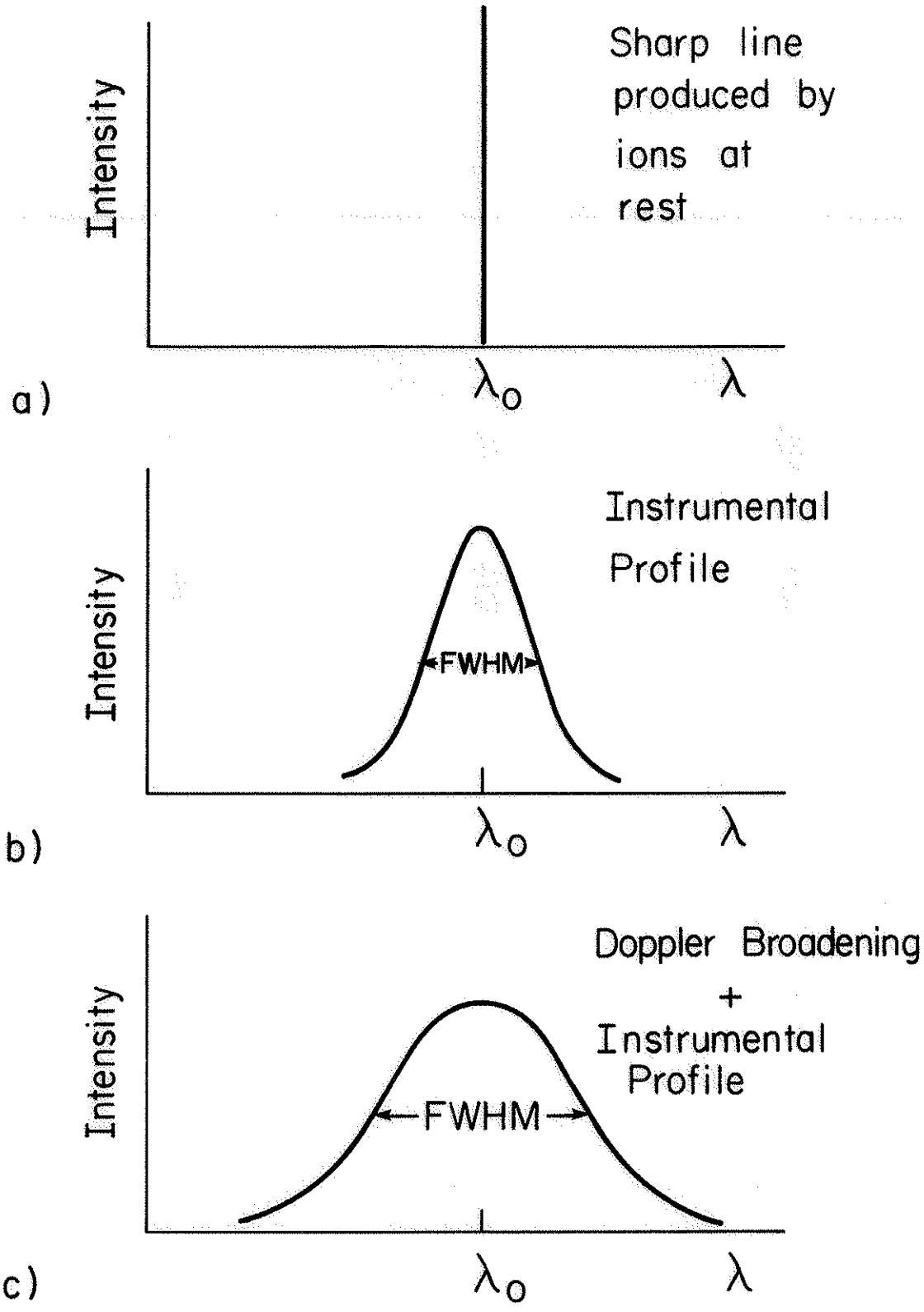
Intensity
Sharp line
produced by
ions at
rest
λ_o
λ
a)
Intensity
Instrumental
Profile
FWHM
λ_o
λ
b)
Intensity
Doppler Broadening
+
Instrumental
Profile
FWHM
λ_o
λ
c)

broadening will produce a line shape with a Gaussian profile which has a FWHM $\delta\lambda_D$ given by[36]

$$\frac{\delta\lambda_D}{\lambda_o} = 7.56 \times 10^{-5}\sqrt{\frac{T_i}{M}} \quad , \tag{7-8}$$

where λ_o is the unperturbed wavelength, T_i is the ion temperature in eV, and M is the mass number of the ion. The instrumental profile can usually be expressed as a Lorentzian, and for most practical purposes this can be approximated as a Gaussian.[37] The monochromator output is then the convolution of two Gaussians and the observed FWHM ($\delta\lambda_{OBS}$) is related to the two Gaussians by:

$$(\delta\lambda_{OBS})^2 = (\delta\lambda_D)^2 + (\delta\lambda_{INS})^2 \tag{7-9}$$

In practice, the Doppler measurements were made with the Jarrell-Ash, and its instrumental profile was obtained by scanning it over the spectral lines of simple discharge lamps. This instrument had an instrumental width of about 0.45 Å with 10 micron slits. Light ions give the largest Doppler widths, so a small amount of He was added to Tokapole discharges, and the broadening of the HeII 4686 line was observed. The observed profiles were obtained on a shot-by-shot basis, and a least squares fit was made to the data to obtain $\delta\lambda_{OBS}$. Figure 7-5 shows a typical example of the experimental data and the least squares fit to that data. The Doppler width was then determined with the aid of Eq. 7-9. Figure 5-7 shows $T_i(t)$ as determined by this technique. T_i was relatively constant at about 15-18 eV. Doppler measurements of the CIII 4648 line yielded results in agreement with the HeII results.

Fig. 7-5: Experimentally observed line profile from HeII 4686. The line profile is the convolution of the instrumental profile and the Doppler-broadened profile. Curve fit is a least squares fit of the data points to a Gaussian.

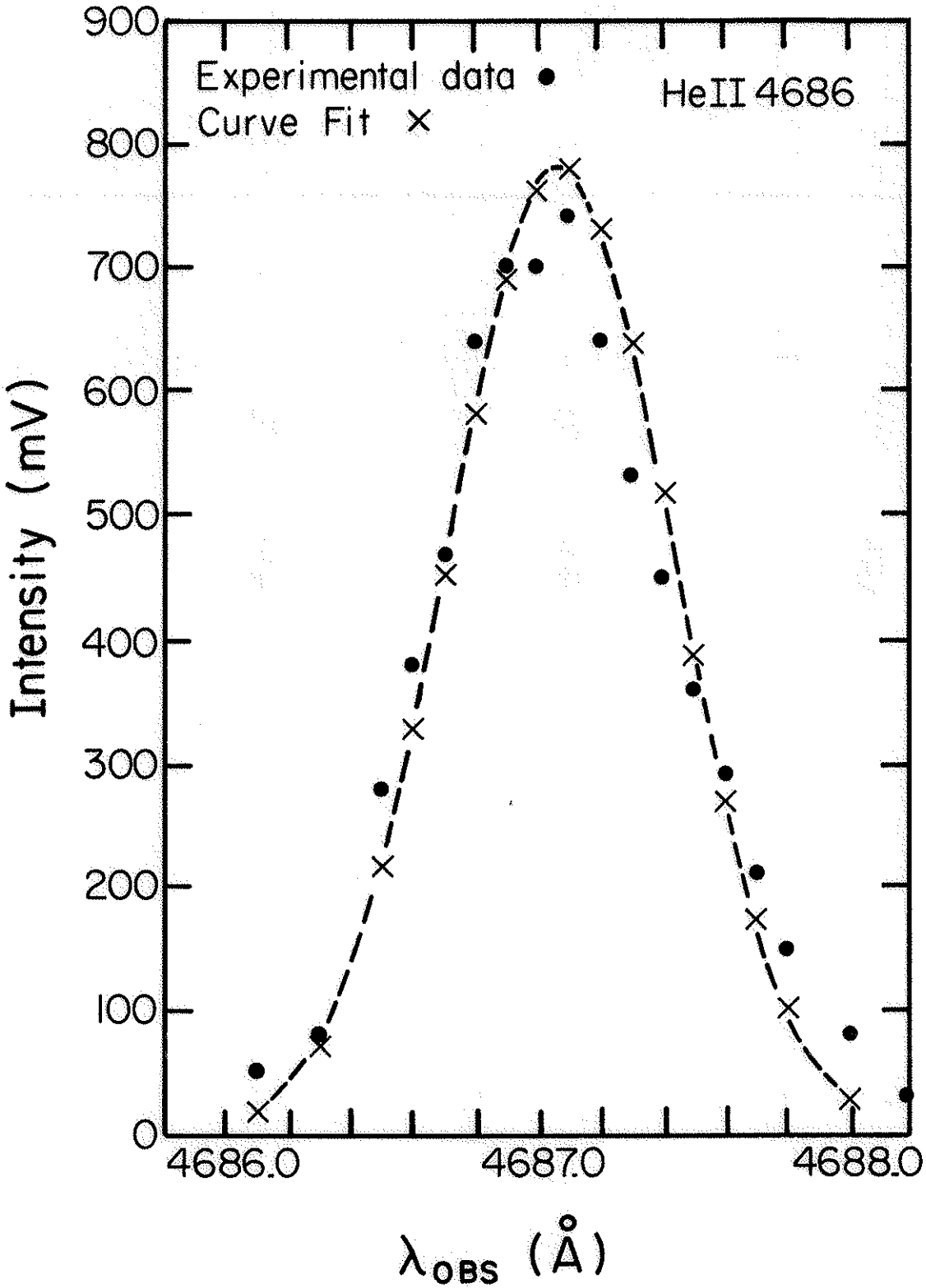
Experimental data
Curve Fit
HeII 4686
Intensity (mV)
900
800
700
600
500
400
300
200
100
0
4686.0
4687.0
4688.0
λOBS (Å)

More recent data have shown that T_i from HeII was about 10 eV in December, 1978 and about 25 eV in March, 1979. Ten eV is near the lower limit of T_i for which HeII 4686 may be used.

Two questions must be addressed to fully validate the Doppler measurements. The impurity ions used for the Doppler measurements typically have a non-uniform spatial distribution, so that T_i determined from Doppler measurements is the ion temperature in some region of the plasma. (In particular, impurity ions are localized in shells during the current plateau in standard tokamaks.) To prevent misleading conclusions about T_i, one should know where the radiation originates. Since the helium was introduced before the start of the Tokapole discharges, the HeII was probably well distributed in the plasma at the time of the Doppler measurements, and the data yielded a volume-averaged T_i. This has not been well verified.

One must also consider the question of the ion-ion equilibration time to be certain that the species observed has the same temperature as the protons. This problem can be addressed with the help of Spitzer.[38] When a species of test particles of temperature T is immersed in a background plasma with temperature T_b (b refers to the background plasma), and if both species are charged, the rate at which T changes is given by

$$\frac{dT}{dt} = \frac{T_b - T}{t_{eq}} \tag{7-10}$$

where t_{eq} is the equilibration time. This time is given by

$$t_{eq} = \frac{7.34 \times 10^6 \; A \; A_b}{n_b \; Z^2 \; Z_b^2 \; \ln \Lambda} \left(\frac{T}{A} + \frac{T_b}{A_b} \right)^{3/2} \tag{7-11}$$

where t_{eq} is in seconds, A is the mass number, Z is the charge, n_b is the density of the background species in cm^{-3}, T is in eV and $\ln\Lambda$ is the Coulomb logarithm. For typical Tokapole parameters, t_{eq} for He II was about 20 μsec. If Eqs. 7-10 and 7-11 are solved with T initially 0, T_b = 20 eV, $n_b = 1 \times 10^{13}$ cm^{-3}, A = 4 and A_b = 1, then T reaches 19.5 eV in 60 μsec. Clearly, the He II was equilibrated with the protons in Tokapole discharges.

Sprott has performed a steady state calculation[39] in which a 1% He impurity was immersed in a background plasma (10^{13} cm^{-3}) of protons and electrons. The electrons gained energy from ohmic heating and the ion species exchanged energy by colliding with the electrons and with each other. For a constant energy confinement time of 300 μsec for all species, the calculated temperatures of the various species are given as functions of the ohmic input power by Fig. 7-6. It is clear that the He II and proton temperatures are strongly coupled. Furthermore, at an input power of about 300 kW (corresponding to typical Tokapole conditions), T_e is about 100 eV while T_i is about 10 eV. These numbers agree well with the actual measurements and add consistency and confidence to the measurements of all of these parameters.

Fig. 7-6: Results of steady state power balance calculation. Temperatures of electrons, protons, and He II ions as functions of ohmic input power to electrons. Temperatures of protons and helium ions are essentially identical over the range of input power used in the calculation.

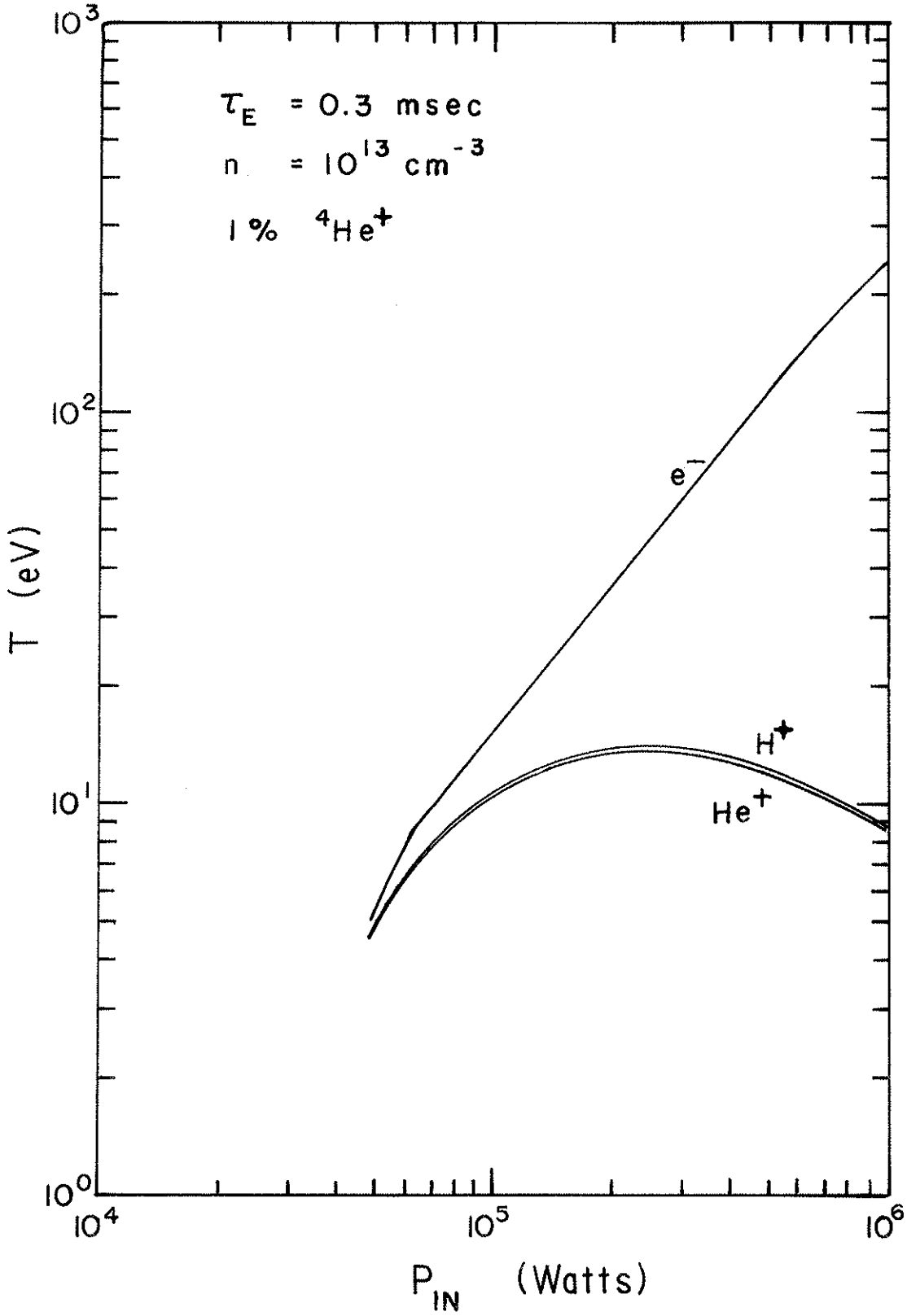
τ_E = 0.3 msec
n = 10^{13} cm^{-3}
1% $^4He^+$
e^-
H^+
He^+
T (eV)
P_{IN} (Watts)
10^3
10^2
10^1
10^0
10^4
10^5
10^6

REFERENCES

1. M. Mattioli, Euratom-CEA Association Fontenay-aux-Roses, Report EUR-CEA-FC-761, 1975.
2. A. H. Gabriel, C. Jordan in Case Studies in Atomic Collision Physics II, M. R. C. McDowell, E. W. McDaniel (eds.), (North-Holland Publishing Co., Amsterdam, 1972), ch. 4.
3. W. Lotz, Zeitschrift für Physik 216, 241 (1968), in English.
4. A. Salop, Phys. Rev. A 14, 2095 (1976).
5. C. Breton, C. DeMichelis, M. Mattioli, J. Quant. Spectrosc. Radiat. Transfer 19, 367 (1978), and Euratom-CEA Association Fontenay-aux-Roses, Report EUR-CEA-FC-853, 1976.
6. I. L. Beigman, L. A. Vainshtein, A. Vinogradov, Sov. Astron.-AJ 13, 775 (1970).
7. S. M. V. Aldrovandi, D. Péquignot, Astron. Astrophys. 25, 137 (1973).
8. A. Burgess, Astrophys. J. 141, 1588 (1965).
9. A. L. Merts, R. D. Cowan, N. H. Magee, Jr., Los Alamos Scientific Laboratory,Report LA-6220-MS, 1976.
10. D. E. Post, R. V. Jensen, C. B. Tartar, W. H. Grasberger, W. A. Lokke, At. Data and Nucl. Data Tables 20, 397 (1977), and Princeton Plasma Physics Lab., Rep. PPPL-1352, 1977.
11. H. J. Kunze, W. D. Johnston III, Phys. Rev. A 3, 1384 (1971).
12. W. D. Johnston III, H. J. Kunze, Phys. Rev. A 4, 962 (1971).
13. H. Van Regemorter, Astrophys. J. 136, 906 (1962).

14. W. L. Wiese, M. W. Smith, B. M. Glennon, Atomic Transition Probabilities, NSRDS-NBS 4 Report, National Bureau of Standards, 1966.

15. M. W. Smith, W. L. Wiese, Astrophys. J. Suppl. Ser. 196, 23, 103 (1971).

16. G. A. Martin, W. L. Wiese, Phys. Rev. A 13, 699 (1976).

17. O. Bely, Proc. Phys. Soc. (London) 88, 587 (1966), Ann. Astro-Phys. 29, 131 (1966), and Ann. Astrophys. 29, 683 (1966).

18. J. Davis, J. Quant. Spectrosc. Radiat. Transfer 14, 549 (1974).

19. J. Davis, P. C. Kepple, M. Blaha, J. Quant. Spectrosc. Radiat. Transfer 15, 1145 (1975).

20. R. Mewe, Astron. Astrophys. 20, 215 (1972).

21. M. Blaha, Astrophys. J. 157, 473 (1969).

22. L. A. Vainshtein, I. I. Sobelman, E. A. Yukov, Cross Sections of Excitation of Atoms and Ions by Electrons (Nauka, Moscow, 1973), in Russian.

23. C. Breton, C. De Michelis, M. Mattioli, Euratom-CEA Association Fontenay-aux-Roses, Report EUR-CEA-FC-822, 1976.

24. I. I. Sobelman, Introduction to the Theory of Atomic Spectra (Pergamon Press, New York, 1972).

25. N. H. Magee, J. B. Mann, A. L. Merts, W. D. Robb, Los Alamos Scientific Laboratory, Report LA-6691 MS, 1977.

26. Atomic Data for Fusion, Supplement 1, C. F. Barnett, W. L. Wiese (eds.), Controlled Fusion Atomic Data Center of ORNL and NBS, March, 1977.

27. B. L. Moiseiwitsch, S. J. Smith, Rev. Mod. Phys. 40, 238 (1968).

28. E. Hinnov, Phys. Fluids 7, 130 (1964).

29. Equipe TFR, Nucl. Fusion 15, 1053 (1975) and Euratom-CEA Association Fontenay-aux-Roses, Report EUR-CEA-FC-777, 1975.

30. J. L. Terry, K. I. Chen, H. W. Moos, E. S. Marmar, Nucl. Fusion 18, 845 (1978), and Johns Hopkins University, Technical Report COO-2711-3, 1977.

31. M. Shiho et al., Nucl. Fusion 18, 1705 (1978).

32. M. Mattioli, private communication.

33. E. Hinnov, Phys. Rev. A. 14, 1533 (1976).

34. T.F.R. Group, Plasma Phys. 20, 207 (1978), and Euratom-CEA Association Fontenay-aux-Roses, Report EUR-CEA-FC-892, 1977.

35. DIVA Group, Nucl. Fusion 18, 1619 (1978).

36. A. P. Thorne, Spectrophysics (Chapman and Hall Ltd, London, 1974), p. 259.

37. R. N. Dexter, R. J. Groebner, University of Wisconsin Plasma Studies PLP 768, 1978.

38. L. Spitzer, Jr., Physics of Fully Ionized Gases, 2nd ed. (Interscience Publishers, New York, 1962), p. 135.

39. J. C. Sprott, University of Wisconsin Plasma Studies PLP 782, 1979.

CHAPTER 8

POWER BALANCE CONSIDERATIONS

An important part of this study has been the determination of the plasma energy confinement time of Tokapole discharges and of the contribution of impurity radiation to the total power loss. The central results are that the energy confinement time τ_E is of the order of 200 μsec, that this measured τ_E is consistent with empirical scaling laws for the energy confinement time in tokamaks, and that the radiated power does not dominate the power loss mechanisms. This chapter analyzes the power balance of standard Tokapole discharges in considerable detail.

A. Basic Data

Measurements of the power balance in Tokapole discharges have been hampered by the difficulty of measuring the required quantities. The electron temperature, in particular, has not been accurately measured as a function of space and time. The best available data from standard discharges are used in the following discussion, and reasonable assumptions are made when necessary.

A further complication of the power balance study has been that Tokapole plasmas are composed of two separate regions, the central current channel and the scrape-off plasma, and it is conceivable that the confinement is rather different in the two parts. Therefore, separate calculations are presented for these two regions. Experimental flux plots indicate that the central current channel, the region inside the

separatrix, has about a 16 cm by 16 cm square cross section. It is assumed that the current channel is centered on the minor axis of the machine and that all plasma quantities are constant in square shells centered on the minor axis.

Table 8-1 contains, as functions of time, the measured and calculated plasma quantities used in the study. These quantities, I_p, $\bar{n}_e$, $\bar{T}_e$, P_{in}, U_e, $\dot{U}_e$, and τ_{Ee}, are presented for both cases, and $\bar{T}_i$, P_{ei}, U_i, $\dot{U}_i$, and τ_{Ei} are presented for the central current channel. In addition, P_{rad} is listed with the central current channel data, but clearly some of the radiation also came from the scrape-off region. The plasma currents were obtained by integrating the current density profiles of Fig. 5-7 over the appropriate plasma cross sections. The ohmic input power P_{in} was calculated from

$$P_{in} = \int E_T J_T \, dV \tag{8-1}$$

where the toroidal electric field E_T and the toroidal current density J_T were obtained, respectively, from Figs. 5-6 and 5-7, and the integral was performed over the plasma volume V.

An examination of the ion saturation current profiles of Fig. 5-5 suggested the following assumptions for the electron density spatial profiles: At 0.5 msec, 1.0 msec, and 1.5 to 2.5 msec, the average central electron density was taken to be, respectively, one half of, equal to, and 1.35 times the average scrape-off region electron density. With these assumptions, the average densities in the two regions were obtained from the line-averaged density of Fig. 5-4.

TABLE 8-1

POWER BALANCE DATA

Central Current Channel

Time (ms)	I_p (kA)	$\bar{n}_e$ (10^{13} cm^{-3})	$\bar{T}_e$ (eV)	$\bar{T}_i$ (eV)	P_{in} (kW)	U_e (J)	$\dot{U}_e$ (kW)	τ_{Ee} (μsec)	P_{ei} (kW)	U_i (J)	$\dot{U}_i$ (kW)	τ_{Ei} (μsec)	P_{rad} (kW)	τ_E (μs)
0.5	1.9	0.27	22	13	16	1.1	3.3	90	0.5	0.5	1.3	?	0	131
1.0	7.9	0.64	25	17	37	3.1	9.5	119	1.5	1.3	0.6	1400	19	164
1.5	13.2	0.84	90	19	64	14.6	2.7	243	2.2	1.2	-0.2	500	28	257
2.0	11.2	0.91	55	17	104	9.7	-7.8	89	2.9	1.2	-0.2	390	33	97
2.5	10.1	0.91	38	15	118	6.7	-6.5	55	3.0	1.0	-0.2	310	39	62

Scrape-Off Region

0.5	28.1	0.53	22		455	14.6	19.0	34						
1.0	49.1	0.64	25		893	20.0	8.7	23						
1.5	34.7	0.62	30		494	23.2	0.8	47						
2.0	22.7	0.67	25		256	20.9	0.0	82						
2.5	14.7	0.67	28		94	23.4	0.0	249						

For the first msec of the discharge, the electron temperature was assumed to be flat throughout the machine, and $\bar{T}_e$ was obtained from the spectroscopic data of Fig. 5-4. At 1.5 msec, the central current channel electron temperature was also obtained from Fig. 5-4. (Since the plasma light originated mainly in the central part of the machine, the spectroscopic $\bar{T}_e$ measurement was assumed to reflect the temperature of the central channel.) For the central current channel at times after 1.5 msec and for the scrape-off region at times after 1.0 msec, the average electron temperature was obtained by averaging the conductivity T_e data of Fig. 5-8 and then multiplying the result by $Z_{eff}^{2/3}$, where Z_{eff} was taken to be 3. At 1.5 msec in the central channel, this procedure gave good agreement with the spectroscopic temperature of 90 eV.

The average ion temperature $\bar{T}_i$ in the central current channel was taken directly from the Doppler broadening data of Fig. 5-4. No estimate of T_i was made for the scrape-off region, since there was no information on the T_i profile.

In principle, the stored energy in the electrons U_e is calculated from

$$U_e = \frac{3}{2} k \int n_e T_e \, dV \qquad (8\text{-}2)$$

where k is Boltzmann's constant, and the integral is performed over the appropriate plasma volume V. For the calculations performed here, the average values $\bar{n}_e$ and $\bar{T}_e$ were used, and U_e was calculated from

$$U_e = \frac{3}{2} k \bar{n}_e \bar{T}_e V \quad . \qquad (8\text{-}3)$$

A similar expression was used for the energy stored in the ions U_i.

With the assumption of quasi-neutrality and with the ion densities which were used to calculate Z_{eff} (Chapter 6, section C.3), it was determined that $\bar{n}_i = 0.4\ \bar{n}_e$, (for $Z_{eff} = 3$).

The time rate of change of the plasma energy stored in electrons $\dot{U}_e$ was obtained from the slope of a graph of U_e as a function of time. In a similar way, the time rate of change of the stored ion energy $\dot{U}_i$ was determined. In Tokapole discharges, energy was transferred to the ions by Coulomb collisions with electrons. The power transfer from the electrons to the ions P_{ei} was calculated from

$$P_{ei} = \frac{1.5\ n_i k\ (\bar{T}_e - \bar{T}_i)\ V}{t_{eq}} \qquad (8\text{-}4)$$

where t_{eq} is the electron-ion equipartition time and is given by Eqn. 7-11. The electron energy confinement time τ_{Ee} was obtained from the equation

$$\tau_{Ee} = \frac{U_e}{P_{in} - \dot{U}_e - P_{ei}} \quad . \qquad (8\text{-}5)$$

Similarly, the ion energy confinement time τ_{Ei} was obtained from

$$\tau_{Ei} = \frac{U_i}{P_{ei} - \dot{U}_i} \quad . \qquad (8\text{-}6)$$

Figures 8-1 and 8-2 contain graphs of U_e, P_{in}, and τ_{Ee} for the scrape-off region and central current channel, respectively. Figure 8-2 also contains a graph of τ_{Ei}. In the central channel, the ohmic input power started low and increased in time, reaching a value of about 120 kW at 2.5 msec. The ohmic input power to the scrape-off region increased rapidly to a peak value of about 900 kW at 1.0 msec and then decreased

Fig. 8-1: Stored electron energy, ohmic input power, and electron energy confinement time in the scrape-off region as functions of time.

$\cdot = U_e$, $x = P_{in}$, $o = \tau_{Ee}$, with ohmic input power being only input term; $\Delta = \tau_{Ee}$, with ohmic input power and all of the power loss from the central channel assumed to be power inputs. Only at late times do the assumptions about input power affect τ_{Ee}.

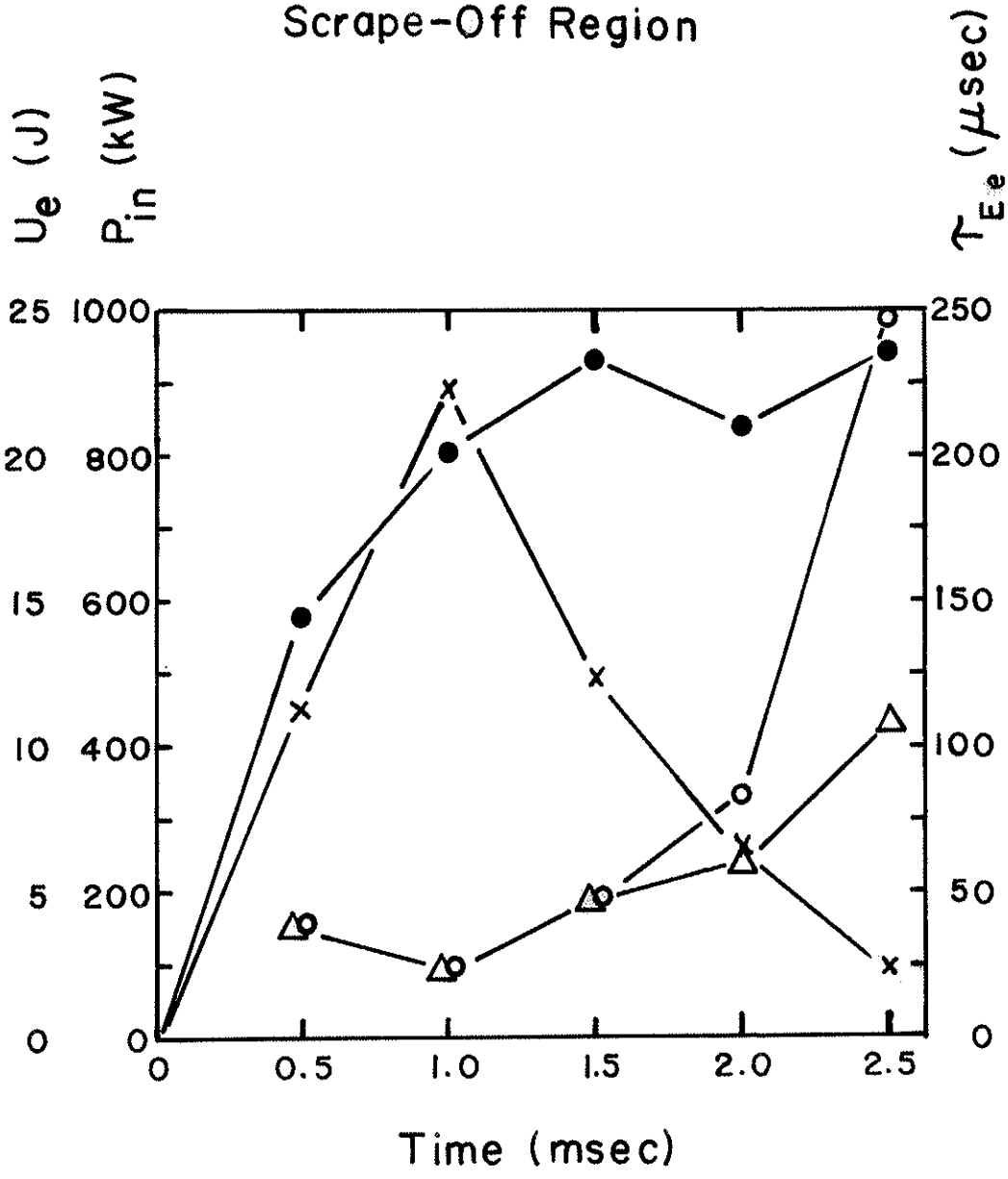
Scrape-Off Region
U_e (J)
P_{in} (kW)
τ_{Ee} (μsec)
25
20
15
10
5
0
1000
800
600
400
200
0
250
200
150
100
50
0
0
0.5
1.0
1.5
2.0
2.5
Time (msec)

Fig. 8-2: Stored electron energy, ohmic input power, electron energy confinement time, and ion energy confinement time in the central current channel as functions of time.

$\cdot = U_e$, $x = P_{in}$, $o = \tau_{Ee}$, $+ = \tau_{Ei}$.

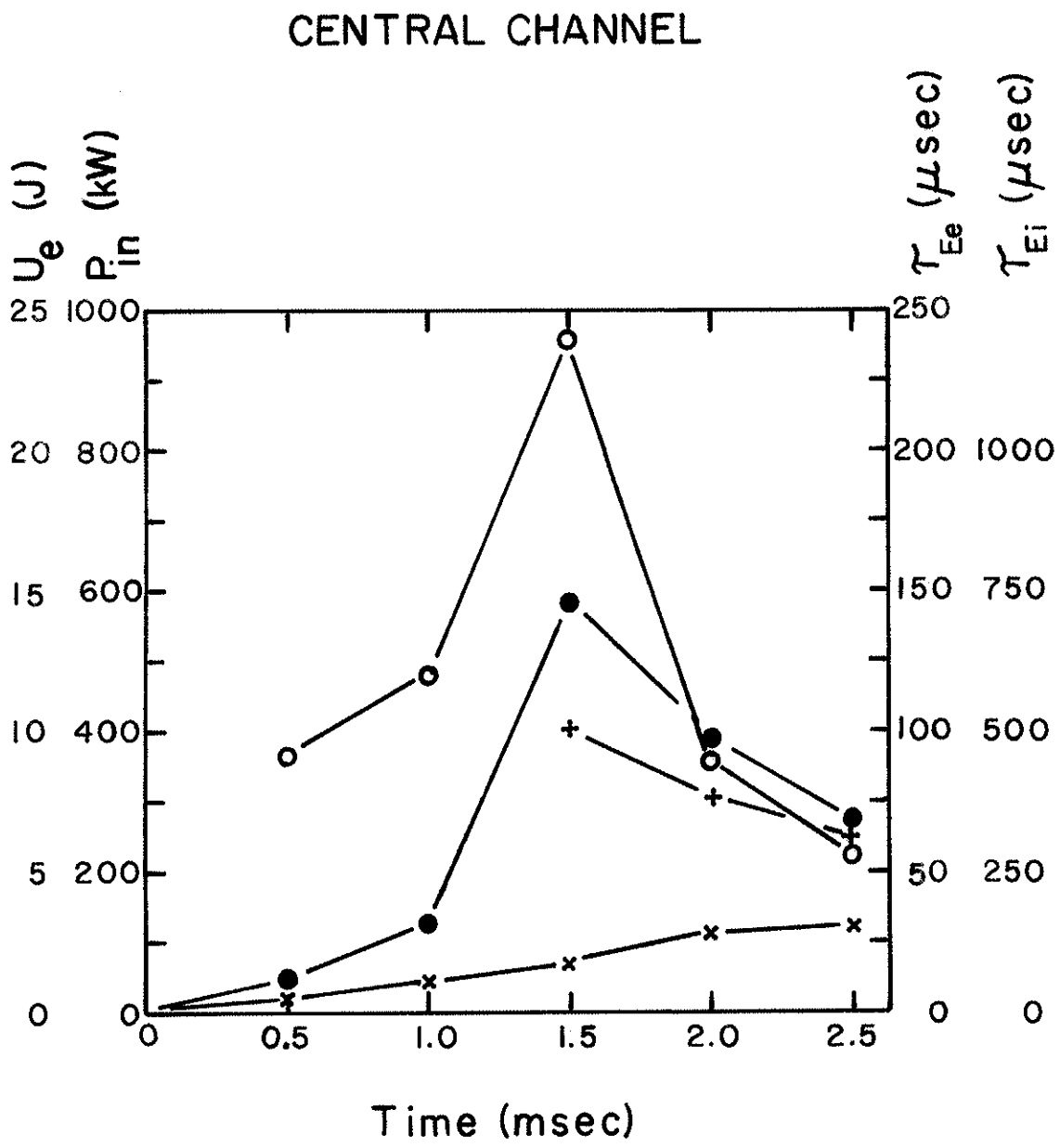
CENTRAL CHANNEL
U_e (J)
P_{in} (kW)
τ_{Ee} (μsec)
τ_{Ei} (μsec)
25 1000
20 800
15 600
10 400
5 200
0 0
250
200 1000
150 750
100 500
50 250
0 0
0
0.5
1.0
1.5
2.0
2.5
Time (msec)

continuously for the remainder of the discharge. The ohmic input power density was initially very large in the skin current and penetrated to the center of the machine as the current did.

In the scrape-off region, the stored electron energy reached a plateau of 20 to 25 J at 1.0 msec. The stored electron energy in the current channel changed rapidly and reached a peak value of about 15 J at 1.5 msec. It is likely that the decrease of U_e in the central channel after 1.5 msec was artificially accelerated by the small Rogowski coil, which caused a premature current reduction.

For both the scrape-off region and the current channel, τ_{Ee} started low early in the discharge and increased with time. This behavior is typical of tokamak discharges[1] and reflects the fact that tokamak confinement is poor until the central current channel is well established. In the central channel τ_{Ee} attained a maximum value of about 240 μsec at 1.5 msec. The rapid decrease in τ_{Ee} may have been partially induced by the Rogowski coil, as discussed earlier. The data show that τ_{Ee} in the scrape-off region climbed rapidly between 2.0 and 2.5 msec. This behavior is suspicious and suggests the need for more reliable analysis of the scrape-off region.

A note of caution should be interjected at this point. The calculation has ignored power flows between the central channel and the scrape-off region. In fact, it is very likely that energy losses from the central channel are energy inputs to the scrape-off region and that the power input to the scrape-off layer is larger than the ohmic input power. Energy could flow in the other direction also, but since the plasma

pressure in the central channel is higher than in the scrape-off region (except for early times) this flow is not expected to be important. Figure 8-1 also contains the scrape-off region energy confinement time calculated with the assumption that all of the energy lost from the central channel is an input to the scrape-off layer. This analysis significantly reduces τ_{Ee} at 2.5 msec, and this result suggests that energy flows between the two regions might be important.

In the central channel, the energy confinement time of the ions was slowly varying and of the order of 300 to 500 μsec. (Estimates of τ_{Ei} earlier in the discharge are not reliable.) Clearly, τ_{Ei} was larger than τ_{Ee}.

The overall plasma energy confinement time τ_E, including the ion and electron contributions, has been calculated for the central channel and is tabulated in the final column of Table 8-1. The maximum value of τ_E of 257 μsec at 1.5 msec is the best estimate of τ_E for the steady state portion of the discharge. Presumably, if the plasma current had remained constant, τ_E would have remained roughly constant.

Figure 8-3 shows the ohmic input power, stored energy and energy confinement time for the entire plasma, including the ion and electron contributions from the central channel and the electron contribution from the scrape-off region. (The neglecting of the ions in the scrape-off layer introduces little error.) The total stored plasma energy U_p reached 30 to 35 J. The energy confinement time τ_{Ep} climbed fairly steadily to about 140 μsec at 2.5 msec.

Of the basic data which have been used in the power balance calculations, the input power data are probably more accurate than any of the

Fig. 8-3: Stored plasma energy, ohmic input power, radiated power, and plasma energy confinement time for the full plasma.

$\Delta = U_p$, $\cdot = P_{in}$, $x = P_{rad}$, $o = \tau_{Ep}$.

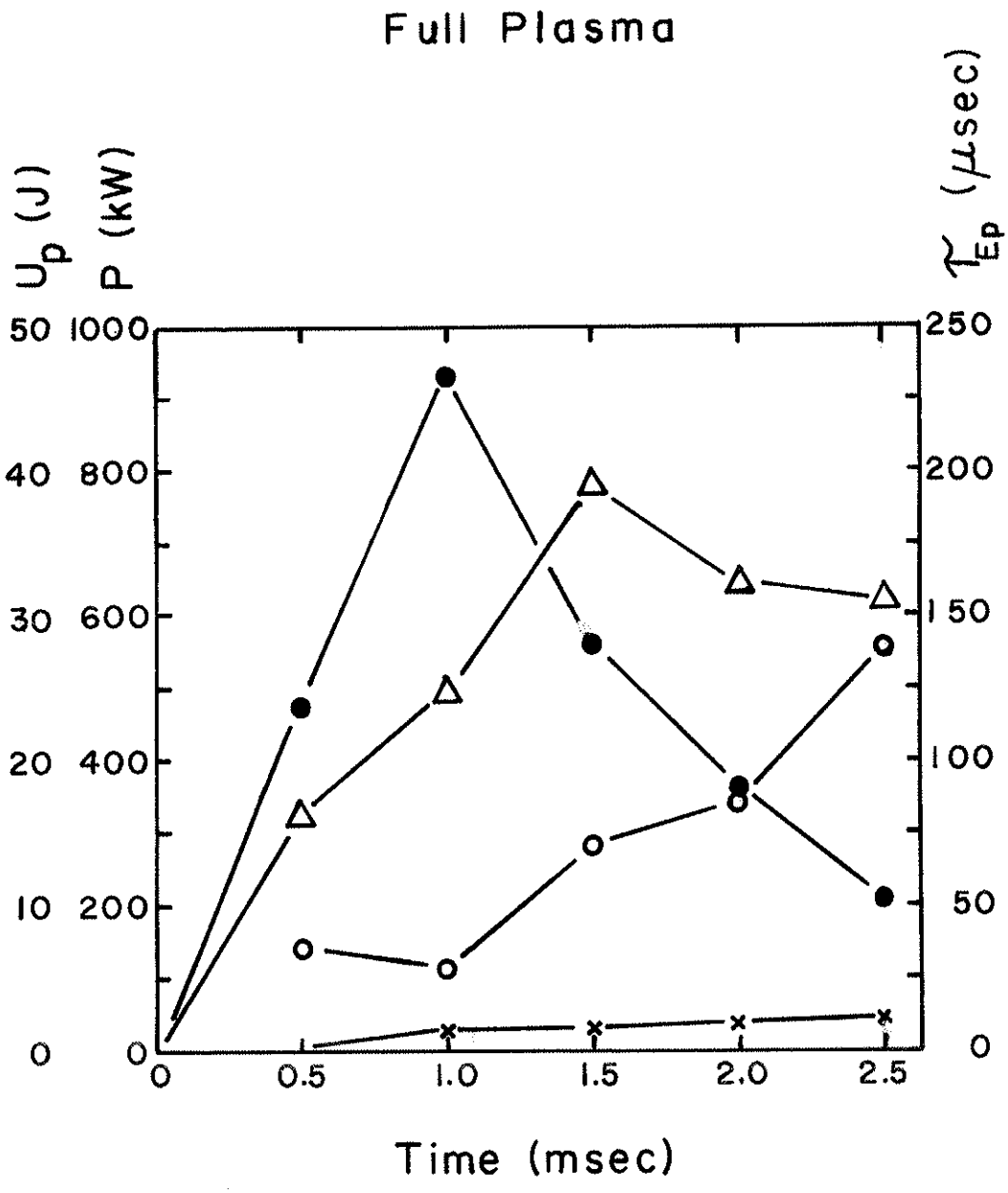
Full Plasma
U_p (J)
P (kW)
τ_{Ep} (μsec)
50 1000
40 800
30 600
20 400
10 200
0
0
250
200
150
100
50
0
0
0.5
1.0
1.5
2.0
2.5
Time (msec)

other numbers and are estimated to have errors of about 30%. The electron density and electron temperature data are considerably less reliable. As a result, the electron energy confinement times are estimated to be accurate to within a factor of two. However, the value of the central channel τ_E of 257 μsec is probably accurate to within a factor of 50% since the maximum values of T_e and n_e are known fairly well.

B. Energy Loss Mechanisms

Figure 8-3 also shows the total radiated power, which was obtained from the VUV integral signal. The radiated power P_{rad} was never more than 20% of the input power. Spatial data of impurity radiation indicate that most of the radiation came from the interior plasma. (It is hypothesized that the radiation was emitted predominantly from the region near the separatrix and field nulls.) Impurity line radiation may have been a significant loss mechanism in some regions of the plasma. However, most of the plasma energy was lost by undetermined processes.

Magnetohydrodynamic instabilities must be considered as possible energy loss mechanisms. The MHD stability properties of the Tokapole magnetic configuration have not been studied theoretically or experimentally. Magnetic oscillations have been observed with $\dot{B}$ probes in the plasma,[2] and it remains to be seen whether or not the magnetic disturbances are deleterious to confinement.

Magnetic islands located at the q = 2 rational flux surface can constitute an important loss mechanism in stable tokamak discharges. A study of ORMAK discharges in which both I_p was varied with B_T held constant and B_T was varied with I_p held constant showed that τ_E varied as $q(a)^{1/2}$,

where q(a) is the safety factor at the limiter.[3] This scaling was observed for $q(a) \leq 6$. It was determined that the energy loss was associated with the size and location of magnetic islands on the $q = 2$ surface. As the islands grew in size and moved out in minor radius, they were increasingly able to transport energy to the limiter.[4]

In Tokapole II, it is conceivable that the existence of unfavorable q profiles could permit the growth of damaging magnetic islands. However, in Tokapole discharges, the q profiles outside of the central current channel are not known, and the existence of magnetic islands has not been proven, although it is suggested by signals on a $\dot{B}$ coil located outside the plasma. Presumably, q rises very rapidly in the vicinity of the separatrix and goes to infinity on the separatrix. How such a q profile might favor the growth of magnetic islands and the transport of plasma energy is not clear. Possibly, islands or other disturbances exist which could permit the rapid transfer of energy to the internal rings and to the common flux region of the plasma.

Another possibility is that the confinement in the vicinity of the poloidal field nulls (x-points) is poor, and energy escapes rapidly from the central current channel in those regions. The x-points might favor the growth of instabilities. The effects of the x-points on confinement are not known.

The major energy loss mechanism in Tokapole plasmas may be the same as that in most other tokamaks: anomalous electron heat loss. The electron energy in most tokamaks is lost about 100 times faster than is predicted by neoclassical diffusion, and it is widely believed that this

loss is due to some type of microinstability.[5] Electrostatic fluctuations from drift waves or magnetic fluctuations from drift waves or shear-Alfvén waves have been proposed as candidates for the heat loss.[4] ORMAK researchers concluded from their data that the fluctuations must be magnetic in origin,[4] and the shape of the x-ray spectrum from Alcator discharges can be explained with the assumption that anomalous diffusion is caused by magnetic fluctuations.[6] A transport code which computes the electron density, the ion temperature, and the electron temperature as functions of space and time produced very good agreement with data from TFR discharges.[7] This code includes transport due to the trapped-electron instability, the current-driven thermal instability, and sawtooth relaxations.

C. Energy Confinement Time Scaling Laws

It is of interest to compare the observed energy confinement time of Tokapole discharges to that of other tokamaks. A number of empirical scaling laws are available for this purpose. Several researchers[8-12] have searched for a simple law, expressing the energy confinement time as a function of n_e, B_T, T_e, q, a (plasma minor radius), and I_p, which would accurately describe the observations of τ_E from a number of existing machines and allow the prediction of τ_E for new machines. The data base which these researchers used probably reflected the best discharges obtained in the machines under study. The discharges used for the data base were magnetohydrodynamically stable; that is, the safety factor at the limiter was normally larger than three. The empirically derived scaling laws are meant to describe a discharge in steady state rather than the current rise phase.

The Jassby scaling law, which fits data from ATC, Alcator, ORMAK, and other machines, is[8]

$$\tau_E \propto n_e a^m q^{1/2}, \tag{8-6}$$

where m is two if the energy loss mechanism is a diffusive process and is one for a convective loss mechanism. The safety factor is assumed to be between 2.5 and 6. A similar law is that proposed by Daughney:[9]

$$\tau_E = 3 \times 10^2 \frac{\bar{n}_e \bar{T}_e^{1/2} a^2}{I_p} \quad \text{msec} \tag{8-7}$$

where $\bar{n}_e$ has units of 10^{13} cm^{-3}, $\bar{T}_e$ is in eV, a is in meters, and I_p is in kA.

Hugill and Sheffield have statistically analyzed data from several tokamaks and proposed an empirical scaling law which predicts the observed energy confinement times quite well.[10] Their law is

$$\tau_E = 2.7 \bar{n}_e^{0.61} a^{1.57} B_T^{0.88} A_i^{0.65} \quad \text{msec} \tag{8-8}$$

where n_e has units of 10^{13} cm^{-3}, a is in meters, B_T is in kG, and A_i is the atomic mass of the ions. Mirnov has proposed a law[11] of the form

$$\tau_E = 3 \times 10^{-4} a I_p \bar{n}_e^{1/2} \quad \text{msec} \tag{8-9}$$

where the units are cm, A, and 10^{13} cm^{-3}.

It has been observed that τ_E in ISX-A was considerably higher than that predicted by most scaling laws. Hirose and Skarsgard proposed a scaling law[12] for τ_E which is consistent with the results from ISX and other machines. Those authors noted that the squared ratio of the electron plasma frequency to the electron cyclotron frequency $(\omega_{pe}/\omega_{ce})^2$

was higher in ISX than in other machines. (The ratio is normally less than one in tokamaks.) Their scaling law is

$$\tau_E = 0.014 \frac{a^2\sqrt{\bar{n}_e A}}{\bar{T}_e \sqrt{Z}} \left(1 + \frac{\omega_{pe}^2}{\omega_{ce}^2}\right)^{-1/2} \quad \text{sec} \qquad (8\text{-}10)$$

where a is in cm, $\bar{n}_e$ has units of 10^{14} cm^{-3}, $\bar{T}_e$ is in eV, A is the atomic weight of the plasma ions, and Z is the charge number of the ions. (Z is not Z_{eff}.)

The scaling laws of Jassby, Daughney, Mirnov, and Hugill-Sheffield have been used to calculate confinement times for the Tokapole discharge data of Table 8-1. The results of the calculations are compared with one another and with the observed confinement times in Fig. 8-4 for the central channel. Jassby's law was used in the form

$$\tau_E = Kn_e \frac{B_T^{1/2}}{I_p^{1/2}} a^2 \quad , \qquad (8\text{-}11)$$

where the constant K was adjusted to give the observed confinement time in the central current chanel at 1.5 msec. For the calculations, B_T was 3.5 kG, and A_i was one. The meaning of the minor radius a for Tokapole discharges is not quite so clear-cut as for standard tokamaks. It was assumed that the magnetic limiter in Tokapole II corresponds to the physical limiter of circular tokamaks, and the "radius" of the separatrix was taken to be 8 cm.

For the central current channel, the Hugill-Sheffield and Mirnov energy confinement times are in reasonable accord with the experiment. In particular, the Mirnov law predicts a steady state τ_E of about 290 μsec, which was only 20% larger than the observed time; the Hugill-Sheffield value was low by about 50%. The favorable agreement of these two

Fig. 8-4: Comparison of observed energy confinement time in central channel with predictions of scaling laws.

· = experiment,

—— = Hugill-Sheffield law,

... = Mirnov law,

----- = Daughney law

-.-.-.-. = Jassby law.

Results plotted as functions of time during the discharge.

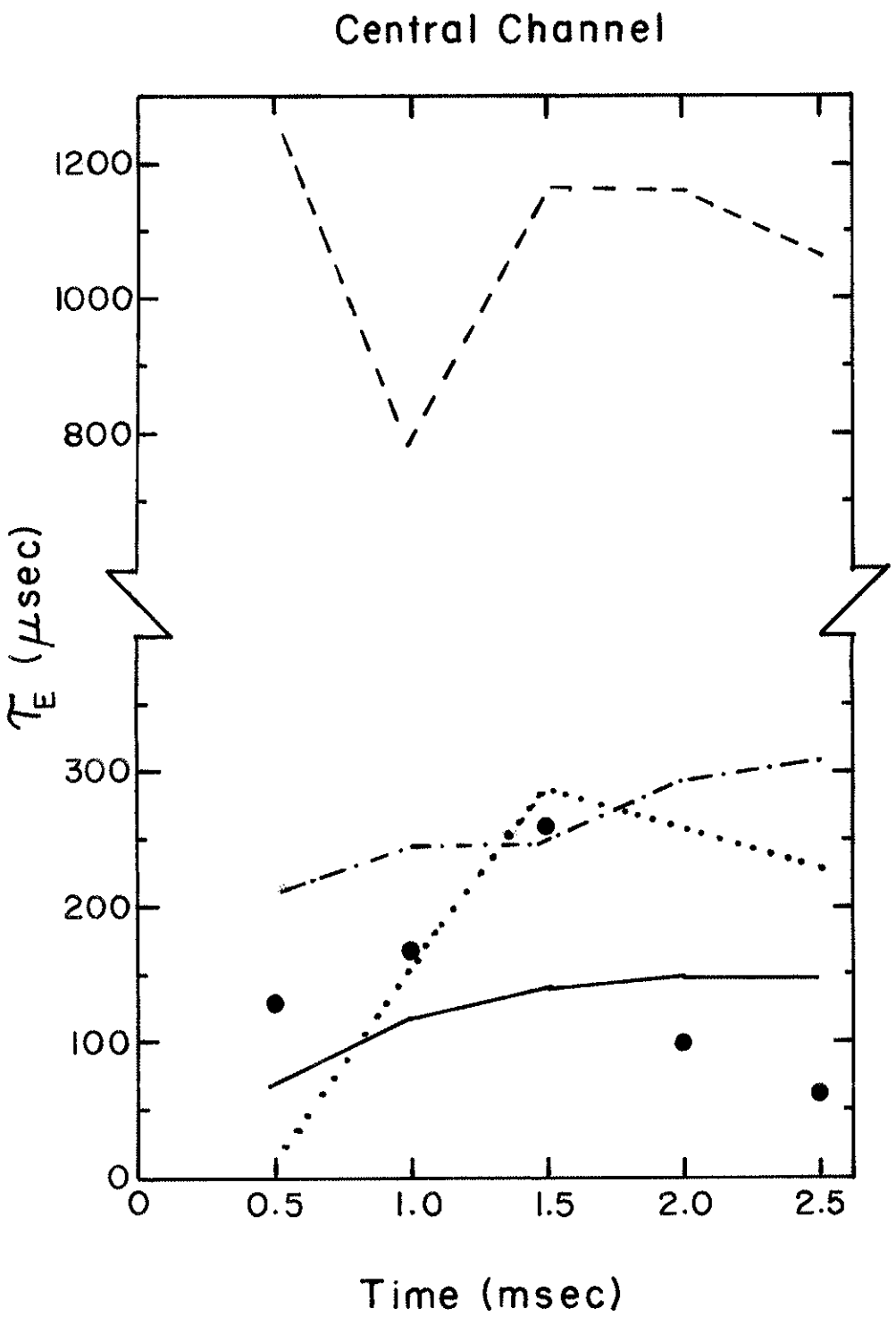
Central Channel
1200
1000
800
300
200
100
0
τ_E (μsec)
0
0.5
1.0
1.5
2.0
2.5
Time (msec)

laws with the experiment for the "steady state" phase suggests that the confinement in the Tokapole central current channel is comparable to that of circular tokamaks and suggests further that an important energy loss mechanism from the central channel is the same as that in other tokamaks: anomalous electron heat transport.

The Jassby value for τ_E at 1.5 msec agrees well with the experiment, of course, because the law was scaled to do so. The Daughney law does not agree with the experiment.

The Hirose-Skarsgard law has been compared to the Tokapole experiment. For typical Tokapole parameters, the ratio $(\omega_{pe}/\omega_{ce})^2$ was about 6.7. (The highest ratio observed in ISX was 2.7.) For the experimental parameters in the central current channel at 1.5 msec, this law yields a τ_E of 1.0 msec, which is clearly in disagreement with the experimentally observed τ_E. This fact suggests that the law does not work in the very limit for which it was intended.

REFERENCES

1. D. L. Dimock et al., Nucl. Fusion 13, 271 (1973).

2. T. Osborne, private communication.

3. L. A. Berry et al., in Plasma Physics and Controlled Nuclear Fusion Research (Proc. 6th Int. Conf. Berchtesgaden, 1976) Vol I, IAEA, Vienna, 49 (1977).

4. J. D. Callen et al., Oak Ridge Natl. Lab., Report ORNL/TM-6564, 1978.

5. R. J. Bickerton, Culham Laboratory, Rep. CLM-R 176, 1977.

6. K. Molvig, J. E. Rice, M. S. Tekula, Phys. Rev. Lett. 41, 1240 (1978).

7. H. H. Klein et al., Phys. Rev. Lett. 42, 1144 (1979).

8. D. L. Jassby, D. R. Cohn, R. R. Parker, Nucl. Fusion 16, 1045 (1976).

9. C. Daughney, Nucl. Fusion 15, 967 (1975).

10. J. Hugill, J. Sheffield, Nucl. Fusion 18, 15 (1978).

11. M. Murakami et al., Phys. Rev. Lett. 42, 655 (1979).

12. A. Hirose, H. M. Skarsgard, Nucl. Fusion 18, 1737 (1978).

CHAPTER 9

DISCUSSION

Observations of the plasma behavior and of impurity effects, in particular, in Tokapole II discharges have been presented. This chapter contains a summary of the major experimental results of this study. The basic conclusions are presented. Possible areas of future study are indicated, and the role of impurities in Tokapole plasmas is discussed.

A. Summary

The main characteristics of a standard Tokapole discharge were as follows. Early in the discharge, the current density and electron density were peaked near the walls. This phase of the discharge was characterized by MHD activity in the skin current. By 1.2 msec the current had started to peak on axis and the electron temperature started to rise. Between 1.5 and 2.0 msec, the plasma current peaked at roughly 40 kA, and $\bar{n}_e$ peaked at about 8×10^{12} cm^{-3} at 2.0 msec. The ion temperature was slowly varying and was about 15-20 eV. The electron temperature of the central current channel reached a peak of roughly 100 eV near the time of the current peak. The steady state value of the electron energy confinement time was about 250 μsec and τ_{Ei} was about 300 to 500 μsec. MHD activity was observed throughout the discharge. As the poloidal gap voltage dropped, the plasma current decayed, and the discharge ended quietly.

The major impurities and their concentrations as percentages of $\bar{n}_e$ were oxygen (3-5%), carbon (~0.5%), nitrogen (associated with vacuum leaks), and copper (undetermined concentration). An air leak resulting

in a base pressure of 1-2 x 10^{-7} Torr produced a nitrogen concentration of 2-4%. For the period during which the impurity concentrations were measured, the contributions of the impurities to the radiated power were: oxygen (25-35%), carbon (~5%), nitrogen (20-30%), metals (~40%). The impurity contributions varied with time; more recent data indicated that 75-85% of the radiated power was due to oxygen, carbon, and nitrogen. Typically, the total impurity radiated power was about 35-70 kW, and P_{rad} was never more than 15-30% of P_{in} during the discharge. Z_{eff} is estimated to have been about 3 and is assumed to have been relatively constant after about 1.5 msec.

Within an order of magnitude, the oxygen influx rate was 6 x 10^{14} atoms/cm^3/sec. Primarily on the basis of results from other machines, it has been assumed that after the impurity build-up of the current rise phase, the impurity concentrations in the central current channel were relatively constant. The influx of impurities was balanced by the outflux.

During doping experiments, in which impurities (O_2,N_2,CH_4) were introduced into the vacuum chamber before the start of the discharge, the AS parameter was independent of the dopant concentration for dopant densities less than about 5 x 10^{11} cm^{-3} (1.5 x 10^{-5} Torr). At larger dopant densities, AS decreased approximately linearly with the added impurity concentration. MHD activity and hard X-ray production increased as the dopant level was increased. Above dopant levels of about 1 x 10^{12} cm^{-3} (3 x 10^{-5} Torr), large amplitude oscillations in the SXR signal were observed. However, doping with H_2 in concentrations of up to 3 x $10^{12}$$cm^{-3}$

produced insignificant effects on the AS parameter.

B. Conclusions

A general and important conclusion is that the central current channel of a Tokapole plasma is very similar to a tokamak plasma. This allows many facets of tokamak physics to be applied to Tokapole discharges.

The results of the doping study and the experiences of several researchers indicate that a bad vacuum does not necessarily deleteriously affect the gross discharge characteristics (e.g., current, plasma stability, AS). In fact, the doping experiments indicate that changes in AS and, presumably, in T_e do not occur for impurity pressures less than $\sim 1 \times 10^{-5}$ Torr. This conclusion does not imply that no plasma parameter is affected by low dopant levels or relatively small air leaks; aside from changes in the optical signals, some parameters are affected by small changes in impurity levels. Furthermore, the deleterious effects of the residual plasma impurity content may be far more serious than the added effects of a bad vacuum. This cannot be tested, of course, without further reducing the residual impurity content.

The case of a bad vacuum is to be contrasted to that of dirty walls. During the initial operation of Tokapole II and after major vacuum openings, the gross plasma characteristics were clearly degraded, and this degradation occurred even when the vacuum was good. Deleterious plasma effects in such cases were probably due to high levels of impurity radiation, which were produced by large impurity concentrations (particularly, carbon) from the walls. Sufficient discharge cleaning has always reduced

this problem.

The power balance study has shown that for normal discharges impurity radiation did not dominate the overall energy loss mechanisms. During the current rise phase, enhanced transport due to instabilities in the skin current probably dominated the energy loss channels. During the steady phase of the discharges, the central channel energy confinement time was comparable to that predicted by the Hugill-Sheffield and Mirnov scaling laws for tokamaks. This agreement suggests that the observed energy loss was due to anomalous electron heat conductivity. However, MHD activity was always observed during the steady state phase, and it is conceivable that macroinstabilities degraded the energy confinement time.

Analysis of the doping experiments and other observations have strongly suggested that the central current density and electron temperature were limited by an instability, and the best candidate for this instability is the m=1, n=1 resistive tearing mode. This mode flattens the current density and electron temperature profiles by internal disruptions. According to this model, radiated power did not limit the central electron temperature; however, the impurities almost certainly cooled the edge of the central channel, controlled the edge resistivity, and helped to shape the current density and T_e profiles.

Low-Z impurities are generated by desorption from ions, electrons, neutrals, and photons. Metallic impurities are generated by sputtering and arcing. Unipolar arcs require the existence of a sheath potential. The 15-20 eV protons in Tokapole discharges have essentially no sputtering yield. Efficient sputtering of metal in Tokapole II requires the

existence of a sheath potential to accelerate multiply-charged ions to sufficiently high energies to sputter upon impact with a metal surface. Thus, sheath potentials play a central role in metal production in Tokapole discharges.

A variety of observations suggests that the magnetic limiter configuration works in the following way. A hot central current channel is separated from the cooler (~20 eV), but dense (~2 x 10^{12} cm^{-3}), plasma in the scrape-off region by a separatrix. The poorly confined plasma of the current build-up phase interacts primarily with the chamber walls and releases impurities to produce the initial impurity concentrations. During the steady state phase of the discharge, the primary impurity production occurs at the rings, and some of the impurities diffuse into the central current channel.

The scrape-off layer (~10 cm wide) is expected to insulate the main current channel from the wall. Ions in the scrape-off layer have a large amount of poloidal flux to cross to penetrate to the central channel. Low-Z neutrals released from the wall with energies less than ~3 eV will be ionized and trapped in the magnetic field of the scrape-off plasma. In contrast, neutrals produced at the rings can penetrate into the central channel, or if the impurities are ionized near the rings, they have considerably less poloidal flux to cross than ions diffusing from the walls. By virtue of its lower temperature and density, the scrape-off plasma has a much less severe interaction with the walls than the hot central plasma would have, and this fact serves to further reduce the wall impurity influx.

Spatial impurity data indicate that the impurity radiation is pro-

duced in the central regions of the plasma. The oxygen modeling strongly indicates that the radiation does not come from the hot current channel itself. It is consistent with these observations to assume that the impurity radiation is primarily produced in the vicinity of the separatrix.

C. Discussion

This research has suggested several areas for further study. Work is needed to determine exactly what the processes are that produce impurities and to further clarify the places from which impurities originate. In particular, the rings must be studied as possible impurity sources. Studies of the sheath potentials, especially those near the rings, would give insight into the mechanisms for metal production.

Closely related to such studies is the need for further attempts to control impurities. Presumably, an understanding of impurity production mechanisms would lead to methods for effective impurity control. Candidate techniques for impurity control and elimination are the Taylor discharge cleaning method, titanium gettering, the use of non-evaporable getters, limiters on the rings, ring biasing, electron injection techniques, and the use of a gas blanket. One obvious method for which Tokapole II is ideally suited is the use of a burial chamber in the scrape-off region to further isolate the central current channel from the impurity sources. Gettered divertor baffle plates would probably be suitable burial sites.

Other areas for study are the effects of impurities in shaping the current density profile and the role of impurities in MHD activity. The use of electrical probes to measure current density and q profiles and to observe magnetic fluctuations in conjunction with impurity doping

techniques might permit a study of these problems. Ultimately, such data could unfold the individual roles of ohmic heating and impurity cooling in the shaping of the current density profile.

Finally, there is a strong need for an understanding of the stability of Tokapole plasmas and for insight into the role of the observed magnetic oscillations. MHD instabilities are candidates for enhancing the energy losses from Tokapole plasmas.

In the final analysis, the role of impurities in Tokapole II is similar to the role of impurities in the last generation of tokamaks (e.g., ATC, ORMAK, TFR 400): the impurities are tolerable but not desirable. For standard, medium-power discharges, the impurities do not adversely affect the gross plasma parameters. The plasma current, and the ion and electron temperatures are roughly independent of the impurities; the impurities do raise the electron density. In standard tokamaks, impurity effects limit the ultimate achievable parameters. The maximum stable plasma currents and the maximum attainable densities are limited by the disruptive instability, which is caused in part by impurity edge cooling of the plasma.

The experiences of present-day tokamaks, in which $Z_{eff} \sim 1\text{-}2$, probably indicate what could be expected if the impurity concentration of Tokapole plasmas was reduced substantially. For a given set of discharge conditions, the central current density and electron temperature would probably be limited by internal disruptions, as they may be in the present case. However, the electron temperature profile would likely be broader. The electron density would decay more quickly in a clean machine than in

a dirty one, and some type of refueling, such as gas puffing, would be needed to maintain the density for long discharges. Z_{eff} and the plasma resistivity would drop. Under such conditions, a smaller loop voltage would be needed to sustain a given plasma current, and this effect would permit a longer current pulse for a fixed amount of core flux and stored energy in the poloidal field capacitor bank.

The energy confinement time would be somewhat higher with the removal of impurities. For a given toroidal field, the plasma current and electron density could be pushed higher before MHD instability would occur. Thus, the reduction of impurities is crucial to the attainment of high β (ratio of plasma pressure to toroidal magnetic field pressure) plasmas in a tokamak device.

The standard discharge chosen for study during the first year of machine operation and described in detail in this thesis involved machine operation at a toroidal magnetic field (3.5 kG) and a pulse length (3.5 m_{sec}) well below the design limits of the device. Impurity control was accomplished with a low power discharge cleaning technique. The impurity concentrations in the standard discharge did not grossly impair the basic plasma parameters. However, a substantial reduction of the impurity level will almost certainly permit operation in new regimes of τ_E, $\bar{n}_e$, and β.

PLP REPORTS

In this thesis, several references are made to the internal reports of the University of Wisconsin plasma physics group. These reports, which are identified by PLP numbers, are available upon request from:

Plasma Physics Office
University of Wisconsin
1150 University Avenue
Madison, WI 53706